Alma Mater Studiorum – Università di Bologna

DOTTORATO DI RICERCA IN

SCIENZE CHIMICHE

Ciclo XXV

Settore Concorsuale di Afferenza: 03/A1

Settore Scientifico Disciplinare: CHIM/01

DEVELOPMENT AND CHARACTERIZATION OF MICROMACHINED DEVICES FOR SEPARATION TECHNIQUES

Presentata da: Dott.ssa Maddalena Belluce

Coordinatore Dottorato

Chiar.ma Prof.ssa Adriana Bigi

Relatore

Chiar.mo Prof. Pierluigi Reschiglian

Responsabile Scientifico

Chiar.mo Ing. Gian Carlo Cardinali

Esame finale anno 2013

CONTENTS

LIST OF TABLES

LIST OF FIGURES

INTRODUCTION

In 1990 the groundbreaking paper of Manz et al. established the field of micro-total-analysis-systems (µTAS), also called lab-on-a-chip (LOC) systems. The µTAS concept is an extension of the total chemical analysis system (TAS) concept, which was proposed in the early 1980s to address the issue of automation in analytical chemistry [1].

Ideally, a TAS performs all the analytical steps (e.g. sample preparation, chemical and biological reactions, analyte separation and detection) in an integrated instrument. Hence the µTAS concept was developed from TAS by downsizing and integrating its analytical steps onto single monolithic devices. In essence, a µTAS is a device that improves the performance of an analysis by virtue of its reduced size [2]. This signifies that as the sample volume decreases, the overall efficiency increases in accordance with the scaling law. Due to the reduced heat capacity, temperature control over reagents and fluids becomes easier. In addition, since many chemical reactions are diffusion related, they take place faster in small volumes. For the numerous advantages possessed by miniaturization and microfluidics, it is no surprise that the applications have extended from its origin in analytical chemistry to chemical synthesis, biochemistry, and clinical settings [3].

Finally the reduced physical size of many chip-based systems is attractive and important in niche areas, such as 'point-of-care' diagnostics. Indeed there is a recent trend towards a more decentralized diagnostic analysis, so-called point-of-care-testing (POCT) device, which has the aim of performing clinical chemistry analysis directly where the sample is obtained. In this way, for example, the time lag between tests results and patients care is reduced [4].

The crucial enabling technologies came first from the world of micro-electro-mechanical-systems (MEMS), where the use of photolithographic processes to obtain micrometer features in silicon and other substrates was well established [1].

MEMS technology has many applications in microfluidics with many of the key building blocks such as flow channels, pumps and valves be fabricated using mature micromachining techniques. Chemical analysis, drug delivery, biological sensing, environmental monitoring and many other applications typically incorporate MEMS microfluidic devices [5].

The work presented in this dissertation describes the development of micromachined separation devices for both high-speed gas chromatography (HSGC) and field-flow fractionation (FFF) using MEMS technology.

Concerning the HSGC, the three micromachined core components of a GC system (namely injector, separation column and detector) will be presented. In particular, more emphasis will be given to the separation column: theory, design procedures, characterization and experimental results will be discussed. Furthermore, design and experimental results of the microfabricated injector and detector will be reported. All the experimental work has been performed at the Institute of Microelectronics and Microsystems (IMM), unit of Bologna, of the National Research Council of Italy (CNR).

Finally a feasibility study for miniaturizing a channel suited for gravitational field-flow fractionation (GrFFF) will be described together with the experimental results. The proposed GrFFF microchannel is at an early stage of development, but represents a first step for the realization of a highly portable and potentially low-cost POCT device for biomedical applications.

REFERENCES

[1] Verpoorte E., De Rooij N.F.; *Proceedings of the IEEE*, **91** (2003) 930-953.

[2] Ríos et al.; *Trends in Analytical Chemistry*, **25** (2006) 467-479.

[3] Ohno K. et al.; *Electrophoresis*, **29** (2008) 4443-453.

[4] Roda. B. et al.; *Analyst*, 1**38** (2013) 211-19.

[5] Prime Faraday Technology Watch; Wolfson School of Mechanical and Manufacturing Engineering Loughborough University, Loughborough - UK (2002).

1

MICROFLUIDICS MEETS MEMS TECHNOLOGY

Miniaturization in analytical chemistry is a clear trend and has been the subject of an important number of research works. Micromachining technologies, especially those based on silicon, are well suited for the realization of microstructures and microchannels in which small volumes of solution may be introduced. In this chapter a general overview on silicon microfabrication processes is described.

1.1 - INTRODUCTION

The MEMS world has widely demonstrated the integration of mechanical and electrical functionality into small structures for diverse applications. MEMS technology can be found in systems ranging across automotive, medical, electronic, communication and defence applications. Current MEMS devices include for example, accelerometers for airbag sensors, inkjet printer heads, blood pressure sensors, microvalves, biosensors and so on [1].

In the next section, the technological processes employed for the fabrication of MEMS structures in silicon substrate are described. In addition the technological procedures for sealing the MEMS devices are reported.

1.1.1 - What is MEMS?

Micro-electromechanical systems (MEMS) are process technologies used to create tiny integrated devices or systems that combine mechanical and electrical components. Microdevices are fabricated using integrated circuit (IC) batch processing techniques and can range in size from a few micrometers to millimetres. These devices (or systems) have the ability to sense, control and actuate on the micro scale, and generate effects on the macro scale.

In the most general form, MEMS consist of mechanical microstructures, microsensors, microactuators and microelectronics, all integrated onto the same silicon chip. A microsensor detects changes in the system environment; an 'intelligent' part processes the information detected by the sensor and makes a decision in the form of a signal; and a microactuator acts on this signal to create some form of changes in the environment.

Sensors and actuators are broadly termed transducers and are essentially devices that convert one form of energy into another [1].

1.1.2 - Microfluidic Devices

MEMS technology has also many applications in microfluidics. The key building blocks, such as flow channels, pumps and valves are fabricated using mature micromachining techniques. Chemical analysis, drug delivery, biological sensing, environmental monitoring and many other applications typically incorporate MEMS microfluidic devices. It should be noted that in MEMS fluidic devices the type of flow (laminar or turbulent), and the effect of bubbles, capillary forces, fluidic resistance and capacitance all have an effect on their final design [1].

The most basic elements of a microfluidic device are the microchannels and microchambers. These are passive fluidic elements, formed in the planar surface of the chip substrate, which serve only to physically confine liquids to µL- or nL-volume cavities. Interconnections of channels allow the realization of networks along which liquids can be transported from one location to another on a device. In this way, small volumes of solution may be introduced from one channel into another, and controlled interaction of reactants is made possible.

The analytical chemists employed microfabrication techniques to design and fabricate microchannel manifolds with the small volumes required by TAS.

MEMS technology includes techniques, such as film deposition, doping, lithography, and etching, developed four decades ago for the microelectronics industry. In addition, special etching and bonding processes that permit to obtain three-dimensional microstructures with micrometer resolution have been and continue to be developed.

Micromachining technologies are primarily silicon-based due to its excellent mechanical and electrical properties.

Silicon makes possible the combination of mechanical and electrical functions in single devices, providing the impetus for the enormous activity over less than three decades in the area of MEMS.

In a parallel development, the high precision obtainable with micromachining processes has led to their application in the patterning of materials other than silicon. Thus, quartz, glass, ceramics, and polymers are gradually becoming accepted complementary materials to silicon, widening the potential range of applications of microfabricated components and systems [2]. In particular, polymers such as polydimethylsiloxane (PDMS) or epoxy resins such as EPON® SU-8, are widely used materials because they are inexpensive, photopatternable, chemically inert and biocompatible.

In the following sections, a brief description of the main technological steps (photolithography, etching and bonding processes) will be presented.

1.1.3 - Photolithographic Technique

Photolithography is the process of transferring geometric shapes of a mask on the silicon wafer surface.

The photolithography process consists in the following main steps:

- Photoresist deposition
- Soft Bake
- Exposure
- Development
- Hard Bake

In the first step, a thin layer of an organic polymer, called photoresist, which is sensitive to UV radiation, is deposited on the substrate. Soft-baking is the step during which almost all of the solvents are removed from the photoresist coating. Soft-baking plays a very critical role in photo-imaging. The photoresist coatings become photosensitive only after softbaking.

The photoresist is then exposed through the pattern on the glass mask with an UV light in the range of 200 nm – 400 nm wavelength.

For positive photoresist, exposure to the UV light changes the chemical structure of the resist so that it becomes more soluble in the developer. The exposed resist is then washed away by the developer solution. In other words, the mask contains an exact copy of the pattern which is to remain on the wafer.

Negative resists behave in just the opposite manner. Exposure to the UV light causes the negative resist to become polymerized, and more difficult to dissolve. Therefore, the negative resist remains on the surface wherever it is exposed, and the developer solution removes only the unexposed portions.

Hard-baking is the final step in the photolithographic process. This step is necessary in order to harden the photoresist and improve adhesion of the photoresist to the wafer surface.

The Fig. 1.1 shows the pattern differences generated from the use of positive and negative resist.
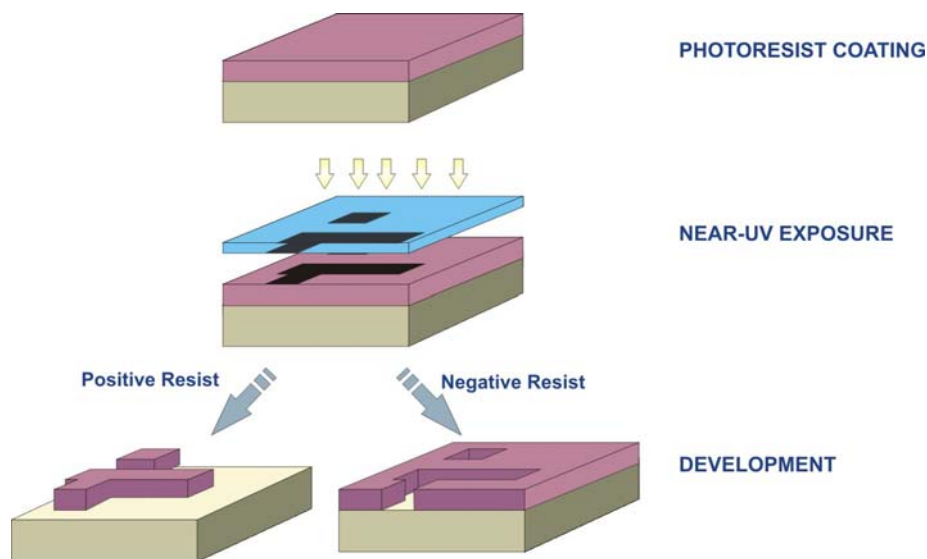
Fig. 1.1 - Photoresist patterning.

1.1.4 - Silicon Etching Technology

The atoms in crystalline silicon are arranged in a diamond lattice structure with a lattice constant of 5.4307 Å and it is composed of two interpenetrating face-centered cubic (fcc) lattices, one displaced 1/4 of a lattice constant in each direction from the other (Fig. 1.2).
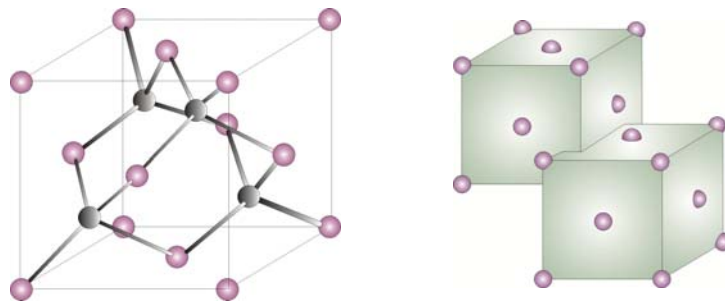
Fig. 1.2 - The diamond cubic lattice structure of silicon.

The crystalline orientation of silicon is important in the fabrication of MEMS devices because some of the used etchants attack the crystal at different rates in different directions.
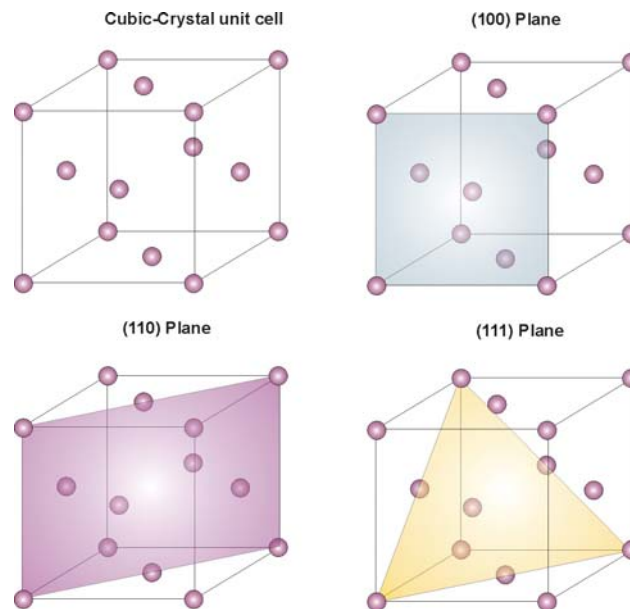
Fig. 1.3 - Crystallographic index planes of silicon.

Fig. 1.3 shows a model of the silicon crystal seen along the <110>, <100> and the <111> directions.

Silicon micromachining can be divided into two categories, depending on what region of the wafer is being worked. Bulk micromachining refers to those processes that involve partial removal of bulk material in order to create three-dimensional structures or free devices, whereas surface micromachining results in structures located on the wafer surface.

Silicon micromachining technologies employ different etching techniques:

- wet isotropic and anisotropic
- dry isotropic and anisotropic

Generally speaking, isotropic methods are those characterized by etch rates which are more or less equal in all directions, whereas anisotropic methods have etch rates which are significantly faster in a particular direction or directions.

Specifically, *anisotropic wet silicon etching* involves dipping the monocrystalline silicon wafer into a solution (e.g., potassium hydroxide, KOH; tetramethylammonium hydroxide, TMAH).

The most common planes in MEMS are the (111), (110), (100) planes. As different planes are cut, different atom densities are encountered. Because of this, when silicon is etched, different planes are etched at different rates. In general terms, the most dense planes are etched the slowest; the (111) planes are the most dense of all the planes. Fig. 1.4 shows a typical cross sections of (100) silicon wafers etched with an anisotropic wet etchant.

The *isotropic wet etching* solution most commonly used is known as HNA, and contains hydrofluoric acid (HF), nitric acid (HNO_3) and acetic acid (CH_3COOH). The resulting channels have rounded side walls, and are wider than they are deep, since etch rates are equal for all crystal planes. Fig. 1.5 displays a SEM micrograph of an array of etched cavity fabricated by a HNA solution.
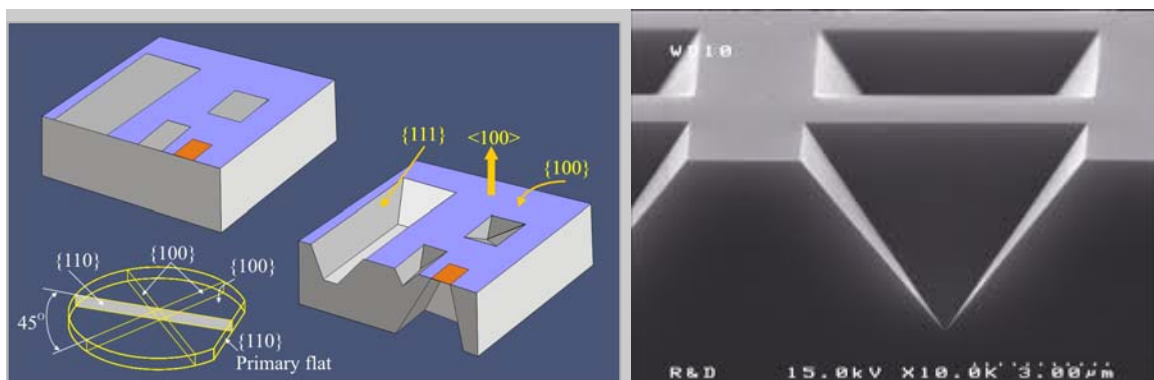
Fig. 1.4 – Etching profiles of a <100> oriented silicon substrate after immersion in an anisotropic wet etchant solution (left). SEM image of an inverted micro-pyramids etched into silicon by an alkaline solution through an oxide mask (right).

Reactive-ion etching (RIE) is an etching technology used in microfabrication that employs chemically reactive plasma to remove material deposited on wafers. The plasma is generated inside a chamber containing gas mixture at low pressure by means of an electromagnetic field which induces the formation of reactive ions and radicals. Depending on the process conditions, etching can be (a) purely chemical, by reaction of free radicals with the surface, (b) physical, through bombardment of the surface with high-energy ions (sputtering), (c) or ion-enhanced energetic etching. These processes can be fully or partially isotropic or anisotropic.
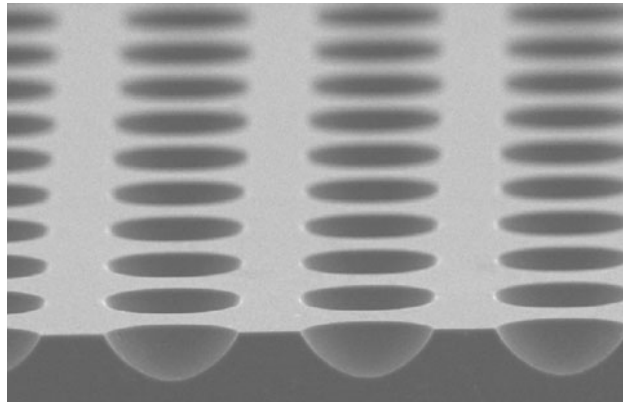
Fig. 1.5 - SEM image showing a cross-sectional microcavities formed by wet etching using HNA.

One type of RIE, called *deep reactive-ion etching (DRIE)*, has gained in popularity in recent years and it has become a key process in the fabrication of MEMS. This technology allows fabrication of vertical sidewalls, high-aspect-ratio structures with high etch rate, independently from the silicon crystallographic planes (Fig. 1.6A).
Typical DRIE equipment uses a high density inductively coupled plasma (ICP) source to obtain fast and uniform anisotropic etching. It is important to observe that purely chemical silicon etching of a fluorine-based plasma allows obtaining an almost perfectly isotropic etching. The advantages with respect to wet isotropic silicon etching obtained by a HNA solution are the good control and uniformity of the process, and the high etching rate. In Fig. 1.6B a SEM image of the cross section of an ICP isotropic etched trench is shown.
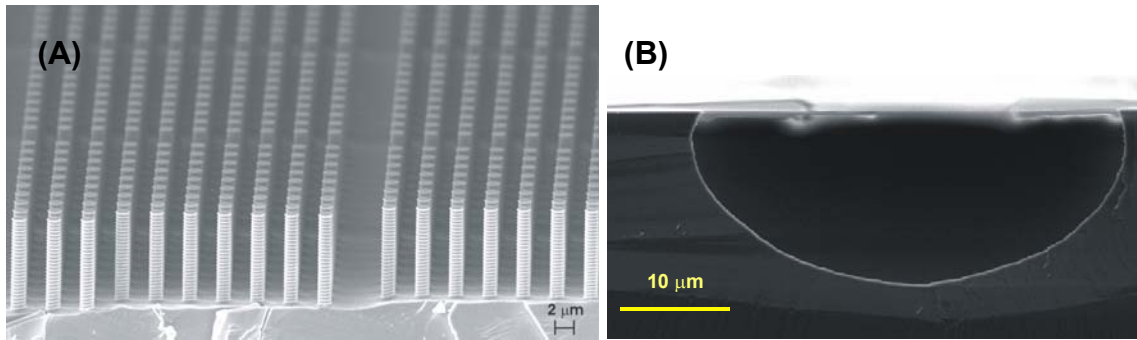
Fig. 1.6 – SEM image of high-aspect ratio micrometric pillars fabricated by a Bosch® DRIE process (A) and a cross section of an isotropic etched trench (B).

1.1.5 - Micromechanical Bonding

In order to form more complex and larger MEMS structures, micromachined silicon wafers can be joined to other materials by use of a special sealing technique, sometimes called micromechanical bonding or, in short, bonding [3]. Bonding can be divided into three categories: bonding without an intermediate layer (e.g. anodic bonding and direct bonding), with an insulating interlayer (e.g. adhesive bonding), and with a metallic interlayer (e.g. eutectic bonding).

Anodic bonding (also known as electrostatic bonding or field-assisted bonding) is a wafer bonding procedure used to join a silicon wafer with a sodium-containing glass wafer through an electric field at medium temperature (180 – 500 °C). The process involves the application of a voltage between 200 and 1000 V over the silicon/glass assembly, with the cathode (negative electrode) on the glass side. The components to be bonded are heated at the same time to a temperature between 180 °C and 500 °C (favoring the increase of the mobility of the ions in the glass substrate). The thermal and electrical fields cause a diffusion of the Na^+ ions contained in the glass that migrate more rapidly toward the cathode (that is, away from the glass–silicon interface). This results in a large electric field at this interface, which pulls the two surfaces together. Chemical bonds between the silicon and glass are formed due to the elevated temperature and the applied electric field [2]. The advantages of this process lie on the highly-strong bond between the substrate, and on the ability to obtain hermetic encapsulations. The drawbacks are the high voltage involved in the process, and the presence of sodium that could be incompatible with some microelectronic processes.

The bonding of silicon wafers at high temperature (> 700 °C) without use of an external electric field is called *fusion bonding*, also referred to as direct bonding because there is no intermediate layer between the wafers. The wafer surfaces spontaneously bond at room temperature due to the interaction of weak forces (e.g. van der Waals, capillary or electrostatic forces). These forces are converted to strong chemical bonds (e.g. covalent bonds) when the wafers pair is annealed at high temperature. High temperature bonding falls in two categories: hydrophilic bonding, in which the bonded surfaces are silicon dioxide, and hydrophobic bonding, in which the surface are made of silicon.

In the latter bonding process, it is of paramount importance to remove the native silicon oxide by an etching solution containing fluorine to enhance formation of Si-F bonds of the exposed silicon atoms. It is also important to avoid re-hydrophilization of the substrate since Si-F bonds contacted with water result in silicon hydroxylation.

In hydrophilic bonding, instead, the silicon wafer surface is covered with an oxide layer that can be a thin native oxide grown by a chemical process, or thermally grown or deposited. The surface contains Si-O-Si and Si-OH bonds, and it is the amount on the surface of the latter one that determines the hydrophilicity of the surface due to polarization of the hydroxyl groups. The hydrophilicity of the surface can be enhanced with various methods of which the most popular is the surface treatment with nitric acid:

$$3Si + 4HNO_3 \rightarrow 3SiO_2 + 4NO_{(g)} + 2H_2O$$

or with a H_2O_2-containing solution (such as standard wet chemical cleaning solution). The reaction between two hydrophilic silicon surfaces during bonding is depicted in Fig. 1.7. At the initial state after establishing contact between the wafers, water molecules form a "bridge" between the surfaces (Fig. 1.7a). During high temperature annealing these water molecules diffuse out from the interface, dissolve into the surrounding material or react with surfaces increasing the number of silanol groups on the surface. Once these water molecules are removed, a bond is formed between silanol groups (Fig. 1.7b). During further annealing, opposing silanol groups react according to reaction:

$$Si-OH + Si-OH \rightarrow Si-O-Si + H_2O$$
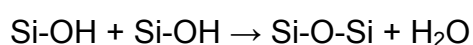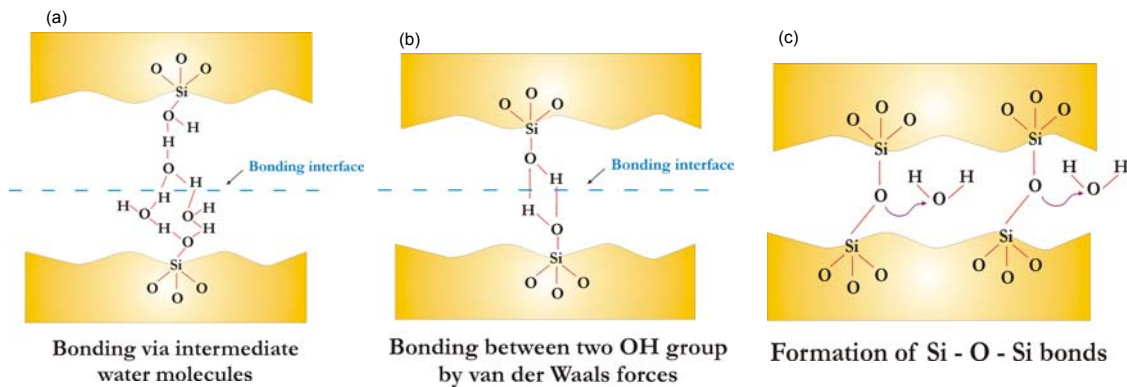
Fig. 1.7- Reaction between two hydrophilic silicon surfaces during bonding.

and, then, Si-O-Si bonding is formed (Fig. 1.7c). The advantages of these techniques are the strong bond between the substrate and ability to achieve hermetic sealing. The drawbacks are the very flat surface, and the high temperature process required that could not be compatible with the standard IC technologies or if a low thermal budget is mandatory [4].

Adhesive bonding is a thermocompressive process that involves the use of an intermediate adhesive layer to connect substrates of different materials. The commercially available adhesive can be organic or inorganic, and it is deposited in one or both substrate surfaces. Typical adhesives can be photoresists (such as SU-8 epoxy resin), polyimides and benzocyclobutane (BCB). This technique is highly versatile, requires a low thermal budget but does not allow hermetic sealing due to permeability of the typically used polymers. Furthermore, the used adhesive could be a contaminant for some high-purity applications.

Eutectic bonding describes a bonding technique with an intermediate metal layer that can produce an eutectic system (typical metal systems are AuSi, AlGe and AuSn). Those eutectic metals are alloys that transform directly from solid to liquid state, or vice versa from liquid to solid state, at specific composition and temperature without passing a two-phase equilibrium, i.e. liquid and solid state. Some advantages of the metal eutectic compositions are the strong and hermetic seal they create and their tolerance to surface deviations, or inclusion of particles.

1.2 - SENSORS AND MICROSYSTEMS GROUP RESEARCH ACTIVITY AT CNR - IMM BOLOGNA

Since several years, the Institute for Microelectronics and Microsystems (IMM) – Section of Bologna is involved in an intense research activity focused on the development of basic micromachining technologies (bulk, surface and wafer bonding) for the realization of three-dimensional micrometric structures relying on the excellent mechanical properties of silicon and the know-how resulting for microelectronic technologies. The use of microsystems technologies allows to address the miniaturization and integration of different sensing/actuating capabilities into a single system, having new functionalities, small dimensions, low power consumption as well as low cost. In particular a part of the research activity is direct to the design, fabrication and characterization of gas sensors and gas sensing microsystems for environmental monitoring and agro-food applications.

REFERENCES

[1] Prime Faraday Technology Watch; Wolfson School of Mechanical and Manufacturing Engineering Loughborough University, Loughborough-UK- (2002).

[2] Verpoorte E., De Rooij N.F.; *Proceedings of the IEEE*, **91** (2003) 930-953.

[3] Dziuban J.A.; "Bonding in Microsystem Technology"; *Published by Springer* (2006).

[4] Suni T. *Ph. D. Thesis*; VTT Technical Research Centre of Finland, Publication 609, Espoo - Finland. (2006).

2

MICRO-GAS CHROMATOGRAPHY

In this chapter, a general overview of gas chromatography and gas chromatographic system is presented. In particular, microfabricated GC capillary columns state-of-the-art is reported.

2.1 - GAS CHROMATOGRAPHY: AN OVERVIEW

Undoubtedly, chromatography is the most common technique for achieving analytic separation. It was invented in the 1901 by the Russian botanist Tswett, who was surprised to obtain, rather than sample filtration, the first chromatography of chlorophylls from plant pigments [1]. The term "chromatography" (from Greek χρῶμα *chroma* "color" and γράφειν *graphein* "to write") brings together a group of important and different methods to separate very similar components within complex mixtures.

In all chromatographic separations, the sample is dissolved in a mobile phase, liquid or gaseous, which is passed in a stationary phase, immiscible, placed in a column. Depending on the typology of the mobile phase, we can distinguish between liquid chromatography (LC) and gas-chromatography (GC). In this thesis work we will focus most of our attention on GC.

GC was first described by James and Martin in 1952 [2], and it has become one of the most important tools for the separation of volatile compounds. The union of sensitivity, speed, and a high resolving power in GC provides a very adequate technique for the separation of complex mixtures and for this reason GC has gained widespread acceptance in numerous application areas, such as:

- *Drugs and Pharmaceuticals*. GC is used not only in the quality control of products but also in the analysis of new products and monitoring of metabolites in biological systems.

- *Clinical Chemistry*. GC is adaptable to samples as blood, urine, and other biological fluids.

- *Foods*. The determination of antioxidant and food preservatives is an active part of the gas chromatographic field. Applications and sample types are almost limitless, and they include analysis of beverages, cheeses, oils, food aromas etc.

- *Environmental Studies*. Air samples can be very complex mixtures and many chronic respiratory diseases (asthma, lung cancer, emphysema, and bronchitis) could result from air pollution or be directly influenced by air pollution. GC is easily adapted to the separation and analysis of such air complex mixtures [3].

Over the years, GC technique has evolved and the most important breakthrough has been the introduction, in the late 1950's, of the capillary columns by M. Golay.

In GC there are two types of separation columns, depending on the stationary phase deposition: packed column and capillary column. The former consists of three basic components: tubing in which packing material is placed, packing retainers (such as glass wool plugs) inserted into the ends of the tubing to keep the packing in place, and, thirdly, the packing material itself. Sometimes, the thickness and the shape of the packing bed are not uniform, and this can cause problems related to the column performance. On the other hand, the capillary column (also named "*open tubular column - OTC*" because of its open flow path) has a thin coating of stationary phase deposited on the inner walls. Such a column is also often referred to as a *wall-coated open tubular column (WCOT)*, and it offers higher performance over the packed ones. Moreover, because of the nature of the material inside a packed column, molecules of the same solute can take a variety of paths before reaching the detector (via eddy diffusion), whereas in a WOTC all flow paths have nearly equal length. In addition, in a packed column, some molecules of the same component encounter thinner regions of stationary phase, whereas other molecules have increased residence times in these thicker pools of phase, all of which create band broadening and than lower resolution [3].

At the beginning of the 1960's D. H. Desty demonstrated the potential of capillary columns with reduced inner diameter for high speed separations. Consequently high

speed gas chromatography (HSGC) or fast gas chromatography (FAST-GC) has become an important tool for the rapid analysis of complex samples. Since 1960, great strides have been made and today HSGC is a mature, well developed field.

2.1.1 - Peculiarity of a GC System

The basic components of a gas chromatograph are (Fig. 2.1):

- the injection system
- the separation column
- the detector
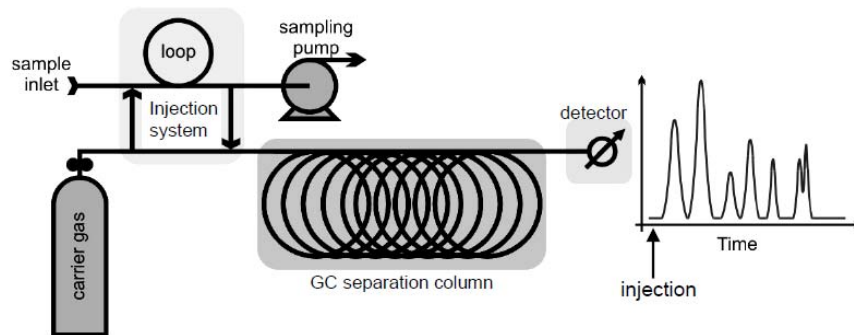
Fig. 2.1 - Schematic representation of a GC system.

The injection system has the function to inject the sample into a continuous flow of an inert, gaseous mobile phase called carrier gas (such as helium, hydrogen or nitrogen) supplied from a cylinder. The sample can be injected, for example, via a gas-tight syringe or aspirated by a pump from a sampling bag. Once injected, the sample is carried by the carrier gas through the separation column whose walls are coated by a polymer, called stationary phase, which is the only responsible for the separation of the various gaseous species. The interaction between the sample and the stationary phase physically delays the elution of the components to different degrees based on their chemical properties. Eluting from the column at different times, the separated compounds pass over a detector, which generates a signal, called chromatogram, corresponding to the concentration of the compound.

The most commonly used detectors in GC are: thermal conductivity detector (TCD), flame ionization detector (FID), electron capture detector (ECD) and mass spectrometer (MS). Thermal conductivity detector is a nondestructive, universal

detection system, since it responds to all constituents in the sample which have a different thermal conductivity with respect to the carrier gas, and it is well suited as a detector for HSGC thanks to its reasonable speed of response.

Typical laboratory GC systems are bulky, expensive and able to perform analyses with high flexibility and low throughput of only few analysis per hour; moreover, in-field analysis by means of conventional GC systems is obstructed also from the bulk caused by the gas carrier cylinder (as shown in Fig. 2.1) and, generally, by the calibration cylinder. Although these systems allow obtaining excellent results from the point of view of resolution, sensitivity and selectivity, unfortunately, they present a certain number of drawbacks that can not be circumvented, especially when the interest shifts from off-line to on-line analysis.

On-site analysis, in fact, is becoming increasingly important, especially in the area of environmental monitoring, since it reduces the risk of contamination, sample loss, and sample decomposition during transport. To be effective, an on-site analytical instrument should be small, lightweight and low maintenance while, on the contrary, common GC systems do not meet this requirements.

The use of MEMS technology for GC-based micro-systems aims at smaller sizes, lower power consumption, faster analyses, lower costs and greatly increased portability for in-field use. Moreover, the overall functionality of GC systems is likely to improve when sensors, valves, pumps, columns and other components are replaced with their lower-volume, lower-power microfabricated counterparts [4].

2.2 - ON- CHIP GC SYSTEM. HISTORICAL BACKGROUND

In 1979 Terry and co-workers at Stanford Electronic Laboratory (Stanford, CA) reported what is generally considered the first example of a microfabricated device for chemical analysis (Fig. 2.2).

That work described the design, fabrication and characterization of a gas chromatograph integrated on a planar silicon wafer. The device included a sample injection system based on a single magnetically actuated microvalve, a 1.5 meters long separation column and a thermal conductivity detector (TCD) [5-6].
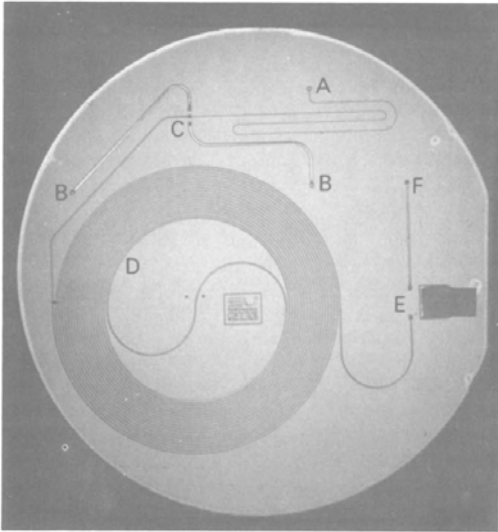
Fig. 2.2 - Photograph of a µGC system fabricated by Terry and co-workers at Stanford University. The view is through the 5-cm Pyrex cover plate.
(A) Carrier gas input feedthrough hole;
(B) sample gas input and exit feedthrough holes
(C) sample injection valve, backside of wafer;
(D) 1.5-m long separating column;
(E) detector gas channel, backside of wafer;
(F) vent to atmosphere [6].

Since that time, huge work has been accomplished on micro gas chromatographic systems in general [7-14] and also on their constitutive building blocks, including separation microcolumn [15-32] in particular, which is the main focus of this dissertation. The numerous works related to sample microinjector [33-37], preconcentrators, [11], [38-40], and microdetectors [11], [34], [37], [41-47] will not be discussed here.

In the following pictures, examples of an injector (Fig. 2.3a), a separation column (Fig. 2.3b) and a detector (namely a thermal conductivity detector, Fig. 2.3c) obtained through silicon micromachining techniques are shown [4]:

(a)   *(b)*   *(c)*
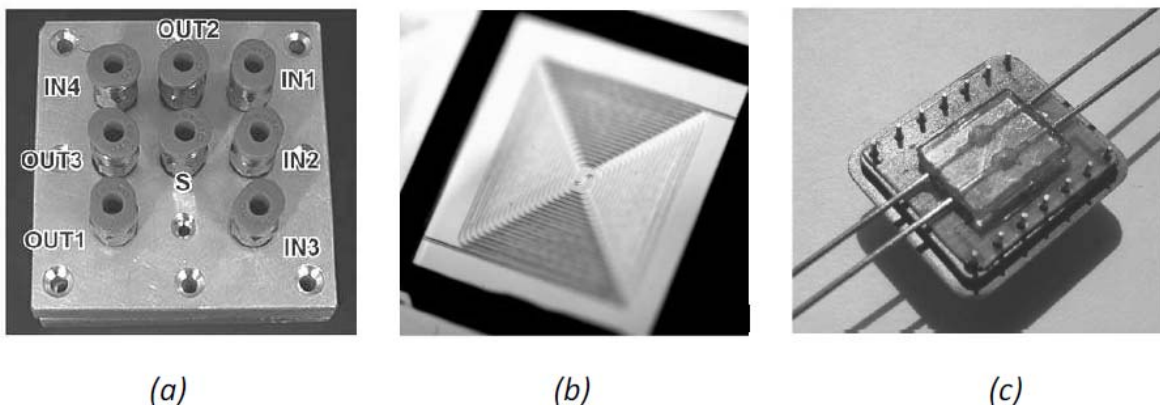
Fig. 2.3 – Examples of microfabricated components of a GC system: injection system (a), separation column (b) and thermal conductivity detector (c) [4].

Although Terry et al.'s GC system was a well-designed device, the system operation was not comparable to the conventional ones due to the poor separation performance of the microcolumn. The reason was the stationary phase pooling in the corners, due to the microcolumn rectangular cross-section (200 μm in width, 30 μm in depth) [48]. Generally, the microcolumn fabrication is followed by the functionalization process, namely the introduction of the stationary phase (see Chapter 3). Unlike the capillary column, having a round cross-section, in the microcolumn proposed by Terry at al., the rectangular design has prevented the uniform deposition of the stationary phase, resulting in the phenomenon known as "pooling".

From 1979 to date, attempts have been made for finding optimal geometric features and parameters of separation column but currently there are no design guidelines for column miniaturization. In particular, it is not known what wall profile a microcolumn should have for a better chromatographic performance.

Early efforts used trapezoidal wall profiles, which are obtained using potassium hydroxide (KOH) etching. Although KOH etching is a relatively easy fabrication method, the resulting channel profile is related to the silicon crystal planes and hence limits the column structures that can be fabricated.

To overcome this limitation, hydrofluoric acid-nitric acid (HNA) based isotropic etching for silicon, and hydrofluoric acid (HF) based iso-etching for glass was used to create circular channels by aligning and bonding two isotropically etched substrates with semicircular channels (Fig. 2.4). In this case, the alignment process is an equipment-intensive process, and typical alignment accuracies are around 3 μm to 5 μm, which is a very high degree of misalignment compared to the typical stationary phase thickness (50-200 nm). Stationary phase deposition in such a microcolumn is expected to create pooling of the phase in the misaligned structures.
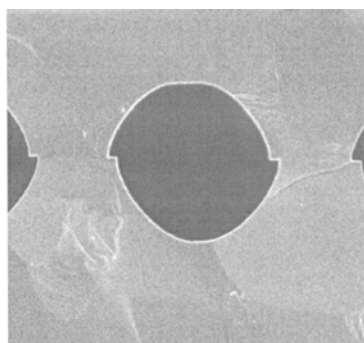
Fig. 2.4 - SEM image of a misaligned microchannel [48]

High aspect ratio rectangular columns are attractive for higher flow rate and sample capacity, although rectangular columns do not theoretically provide better separation characteristics compared to circular columns. As reported in Chapter 1, high aspect ratio microcolumns were generally made using deep reactive ion etching (DRIE) of microchannels in silicon followed by its capping with a Pyrex® cover via anodic bonding [21]. Unfortunately this rectangular design can lead the stationary phase accumulating in the sharp corners.
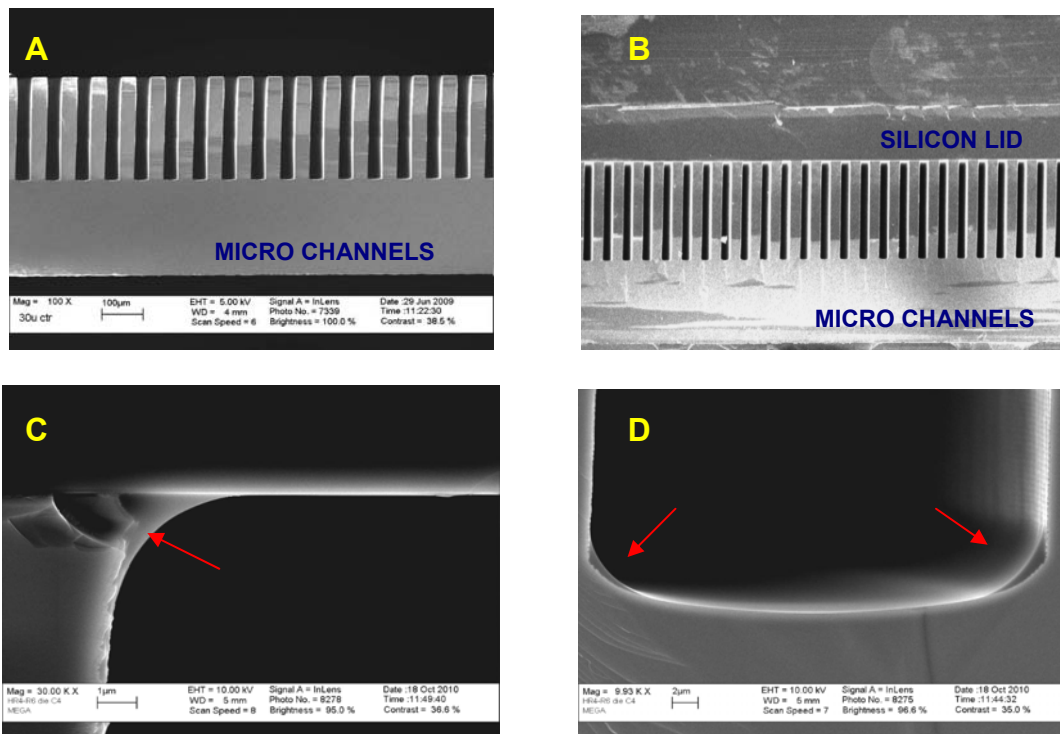
Fig. 2.5 - SEM images showing a 30 µm × 300 µm rectangular cross-section
of a DRIE silicon microchannels (A); microchannels covered with a silicon lid (B);
stationary phase pooling in the sharp corners at the top (C) ad bottom (D)
of the column. Red arrows indicates the stationary phase pooling.

Fig. 2.5A shows a 30 µm-width and 300 μm-depth rectangular cross-section of a DRIE microcolumn, which when capped with silicon lid results in four sharp corners (Fig. 2.5B) in which stationary phase can be deposited (Figs. 2.5C and D).

The issues related to the functionalization of rectangular cross-section channels can be solved by fabricating fully-rounded microchannels without the need for a highly-accurate alignment processes.

Tjerkstra et al. proposed such a solution for chromatography called the buried channel technology (BCT), where the channels were completely enclosed inside the silicon substrate; however, no results were reported for the buried microcolumns (Fig. 2.6) [49].
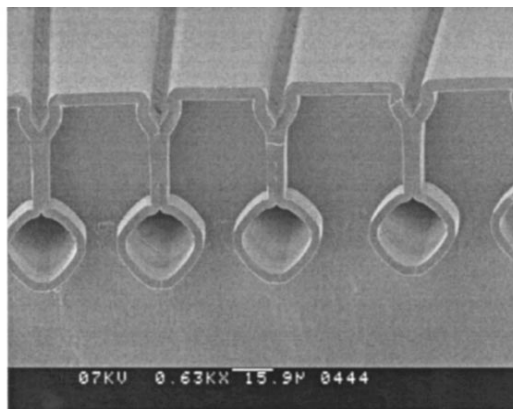
Fig. 2.6 - SEM picture of microchannels fabricated with BCT [49]

Agah et al. adopted the buried channel fabrication technique to make semicircular silicon-oxynitride (SiON) µGC columns (Fig. 2.7) aiming to make low thermal mass microcolumns for rapid temperature programming [21].
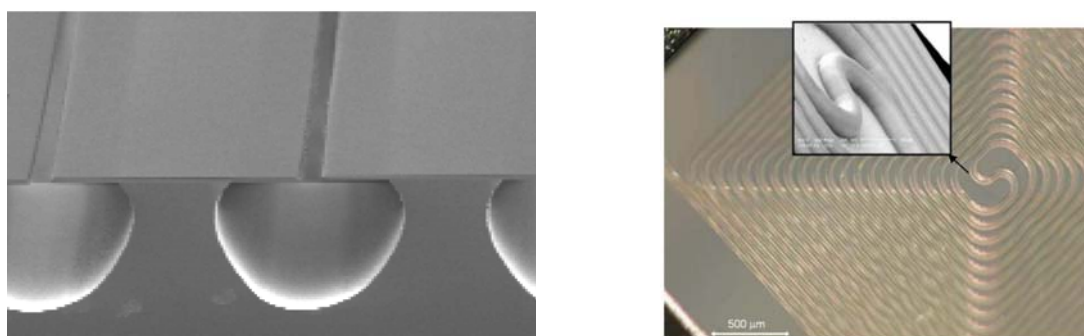
Fig. 2.7 - SEM photograph of unsealed channel using SiON (left); optical image of the column with a SEM close-up image (right) [20].

However, a limitation of this method was the mechanical stability of the released column especially under the vacuum conditions required to coat the column. Moreover, the separation performance was not comparative to the commercial columns, and no experimental Golay-plot data was reported [21].

Radadia et al. reported the fabrication of partially buried microcolumn (Fig. 2.8). A flattened circular column wall profile was accomplished using the partially buried channel fabrication method, a variation of BCT. A Pyrex[®] lid was anodically bonded to the silicon channels.
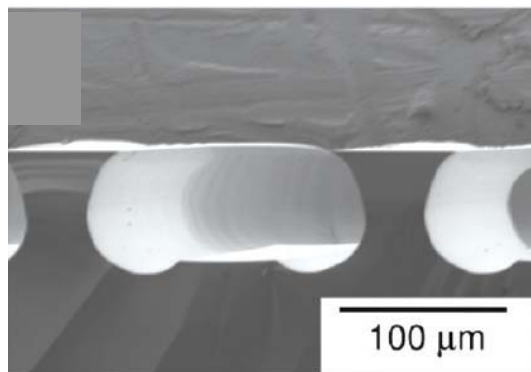
Fig. 2.8 - SEM image showing the 165 μm wide and 65 μm deep
cross-section of a partially buried microcolumn [21].

As shown in Fig. 2.8 the flattened shape of the microchannel does not ensure a uniform distribution of the stationary phase. Also, the bottom channel has a rectangular ridge that could again cause stationary phase accumulation.

Hence most of the microfabricated GC columns reported are made by machining channels in silicon and capping the channels with a Pyrex[®] lid via anodic bonding.

Replacement of the Pyrex[®] lid with silicon is preferable because (1) Pyrex[®] surface contains alkaline impurities that are difficult to passivate while passivation of silicon surfaces (native SiO_2) is relatively easy, which implies lower channel wall adsorption activity and hence decreased peak tailing and peak broadening of polar compounds with the use of an all-silicon column; (2) silicon has two orders of magnitude higher thermal conductivity and diffusivity compared to Pyrex[®]. For fast thermal cycling, Si-Pyrex[®] stack will create non-uniformities in temperature profile, which will cause a reduction in separation performance, and negate some of the benefits of micro-GC systems [21].

Recently Radadia et al. reported the fabrication of an all-silicon microcolumn, developing a novel procedure combining fusion bonding and gold eutectic bonding [24]. Although with this fabrication process the microcolumn can withstand the

temperature cycling required for temperature-programmed separation, a square-DRIE wall profile is obtained (see Fig. 2.9).
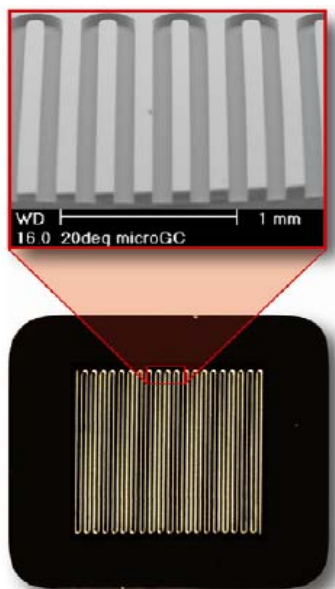
Fig 2.9 - SEM (top) and optical (bottom) images of the DRIE channels
of a microcolumn reported by Radadia et al.[24].

As reported in the previous examples and references, in the last two decades the development and the exploitation of silicon micromachining techniques and micrometric level fabrication processes became an important feature in the achievement of micro-systems to be employed in GC systems with reduced dimensions [4].

To date the works reported in literature deal with microcolumns for HSGC having either a completely rectangular cross-section or semicircular cross-section or square cross-section with smoothened corners. Furthermore, most of the previous microcolumns have been bonded with a Pyrex® lid.

In this work all-silicon microfabricated capillary columns are realized. The microchannel cross-section is circular and the inner wall profile is similar to that of a conventional OTC without discontinuity, interruptions and critical areas. In addition the absence of sharp corners prevents stationary phase pooling and improves separation performances. This has been extensively verified by an accurate characterization. In the following chapter the theory of HSGC will be presented together with the experimental results on the capillary microcolumns.

Also the fabrication and testing of a microinjector and a microdetector for HSGC applications will be reported. The microinjector is based on an innovative pneumatically driven microvalve, which consist of a polymeric actuating membrane. The microdetector is a micromachined thermal conductivity detector (micro-TCD). Among different detector types, TCD is non-destructive sensor, universal and easy to construct.

REFERENCES

[1]   Tswett M.S.; *Proc. Warsaw Soc. Nat., Biol. Sect.*, **14** (1905) 20-39.

[2]   James A.T., Martin A.J.P; *Biochem J.*, **50** (1952) 679-690.

[3]   Grob R.L., Barry E.F.: "Modern practice of Gas Chromatography"; 4th ed. Hoboken, NJ: Wiley (2004).

[4]   Cozzani E.; *Ph. D. Thesis, University of Bologna* (2011).

[5]   Terry S.C. et al.; *IEEE Trans. Electron Devices*, **26** (1979) 1880-1886.

[6]   Jerman J.H., Terry S.C.; *Environment International,* **5** (1981) 77-83.

[7]   Reston R.R., Kolesar, E.S. Jr.; *J. Microelectromech. Syst.*, **3** (1994) 134-146.

[8]   Kolesar, E.S. Jr., Reston R.R.; *J. Microelectromech. Syst.*, **3** (1994) 147-154.

[9]   Lu C.-J., et al.; *Lab Chip*, **5** (2005) 1123-1131.

[10]   Agah M. et al.; *J. Microelectromech. Syst.*, **15** (2006) 1371-1378.

[11]   Lewis P.R. et al.; *IEEE Sensors J.*, **6** (2006) 784-795.

[12]   Zampolli S. et al.; Sensors and Actuators B, **141** (2009) 322-328.

[13]   Zarejan-Jahromi M.A. et al.; *J. Microelectromech. Syst.*, **18** (2009) 28-37.

[14]   Kim S.-K. et al.; *Lab Chip*, **10** (2010) 1647-1654.

[15]   Tjerkstra R.W., et al.; *Electrochim. Acta*, **42** (1997) 3399-3406.

[16]   Lambertus G.R., et al.; *Anal. Chem.*, **76** (2004) 2629-2637.

[17]   Agah M., et al.; *J. Microelectromech. Syst*, **14** (2005) 1039-1050.

[18]   Zampolli S. et al.; *Sens. Actuators B, Chem.*, **105** (2005) 400-406.

[19] Potkay J.A., et al.; *J. Microelectromech. Syst*, **16** (2007) 1071-1079.

[20] Agah M., Wise K.D.; *J. Microelectromech. Syst*, **16** (2007) 853-860.

[21] A. D. Radadia, et al.; *Anal. Chem.*, **81** (2009) 3471-3477.

[22] Zareian-Jahromi M.A. and Agah M.; *J. Microelectromech. Syst.*, **19** (2010) 294-304.

[23] Radadia A.D. et al.; *Sens. Actuators B, Chem.*, **150** (2010) 456-464.

[24] Radadia A.D. et al.; *J. Micromech. Microeng.* **20** (2010) 1-7.

[25] Vial J., et al.; *J. Chromatogr. A*, **1218** (2011) 3262-3266.

[26] Masel R.I. et al.; *US 2009/0178563 A1*.

[27] Masel R.I., Radadia A.D.; *US 2009/0211452 A1*.

[28] Wise K.D. et al.; *US 2003/0233862 A1*.

[29] Wise K.D. et al.; *US 2004/0255643 A1*.

[30] Lehmann U. et al.; *US 2006/0243140 A1*.

[31] Lehmann U.; US *2008/0092626 A1*.

[32] Mc. Gill et al.; US *2009/0272270 A*.

[33] Lehmann U., et al.; *Proc. MicroTAS* (2000) 167–170.

[34] Bessoth F.G., et al.; *J. Anal. At. Spectrom.*, **17** (2002) 794-799.

[35] Dziuban J.A., et al.; *Sens. Actuators A, Phys.*, **115** (2004) 318-330.

[36] Nishiyama T., et al.; *Anal. Sci.*, **23** (2007) 389-393.

[37] Bhushan A., et al.; *Analyst*, **135** (2010) 2730-2736.

[38] Lu C.-J., Zellers E.T.; *Analyst*, **127** (2002) 1061-1068.

[39] Tian W.-C., et al.; *J. Microelectromech.Syst.*, **12** (2003) 264-272.

[40] Tian W.-C., et al.; *J. Microelectromech. Syst.*, **14** (2005) 498-507.

[41] Park J., et al.; *Anal. Chem.*, **71** (1999) 3877-3886.

[42] Grate J.W.; *Chem. Rev.*, **100** (2000) 2627-2648.

[43] Cai Q.Y., Zellers E.T., *Anal. Chem.*, **74** (2002) 3533-3539.

[44] Tienpont B., et al.; *Lab Chip*, **8** (2008) 1819-1828.

[45] Rastrello F. et al.; *Sens. Actuators A, Phys.*, **178** (2012) 49-56.

[46] Rastrello F. et al.; 2012 *IEEE I2MTC, Proceedings*, Art. No. 6229304, pp. 1226 - 1230

[47] Rastrello F. et al.; IEEE Transact. on Instrument. and Measurem., Vol. PP; No. 99, pp. 1 - 8 (2012) Article in Press.

[48] Zareian-Jahromi M.A.; *M. S. Thesis*; Virginia Polytechnic Institute and State University (2009).

[49] de Boer M.J. et al.; *J. Microelectromech. Syst.*, **9** (2000) 94-103.

3

MEMS BASED SILICON CAPILLARY COLUMNS FOR HIGH-SPEED GC

This chapter describes the theory of the gas chromatographic technique. Next, the separation microcolumn design and fabrication are presented together with the microfluidic interconnection system. Also the stationary coating process is illustrated. In the last section, experimental results are discussed.

3.1 - HSGC THEORY

The development of high-speed separation columns as the heart of the analytical system is of paramount importance in the world of µGC for on-field applications such as environmental monitoring, clinical chemistry and public safety.

After a brief overview of the basic gas chromatographic parameters, the equations that describe the performance of open tubular capillary columns will be considered.

3.1.1 - Basic Parameters

The basic parameters that need to be considered in a gas chromatographic analysis are: analysis time, separation efficiency and resolution.

The analysis time is strictly connected to the retention time of the various compounds of the sample mixture to be analyzed, and in particular to the retention time of the last component eluted from the column (t_R):

$$t_R = \frac{L}{u}(k+1) \tag{3.1}$$

where $\bar{u}$ is the average linear carrier gas velocity, L is the column length and k is the retention factor (or capacity factor) defined by:

$$k = \frac{(t_R - t_M)}{t_M} \tag{3.2}$$

where t_M is the holdup time, the time required for the elution of an unretained component.

The retention factor describes the migration rate of the solutes on the column. For a given column, the retention factor for a given component is constant under isothermal conditions but it varies with temperature as given by:

$$k = A \exp\left(\frac{B}{T}\right) \tag{3.3}$$

where *A and B* are empirical constants and *T* is the absolute column temperature.

Eq. (3.3) indicates the significant influence of the column temperature on the analysis time. Increasing the column temperature the retention factor is reduced and hence decreases the overall analysis time [1].

Considering Eq. (3.1), it seems evident that the analysis time can be significantly reduced if the column length used for an analysis is decreased and if the carrier-gas velocity is increased.

On the other hand, the use of excessively short columns and high flow rates results in significant losses in column resolving power, since the effects of extra-column band broadening are amplified and the resulting separation may contain peaks that are severely overlapped with one another. Common sources of extra-column band broadening include, for example, large injection volumes, non-uniform oven temperatures and/or temperature programs, and dead volumes at column connections and/or at the detector [2]. This amplifies the importance of using conditions that provide the maximum possible column efficiency, and by this purpose the choice of decreasing the inner diameter of the columns is the most promising.

The resolving power of a separation column can be quantified by the number of theoretical plates (*N*) and the height-equivalent-to-a-theoretical-plate (*HETP* or, more simply, *H*). The concept of plate theory was originally proposed for the performance

of distillation columns. Martin and Synge first applied the plate theory to partition chromatography. The theory assumes that the column is divided into a number of zones called "theoretical plates" in which a solute molecule equilibrates between the stationary and the mobile phase. To determinate the total resolving power of the column, the total number or theoretical plates N is calculated as follows:

$$N = \frac{L}{H} \tag{3.4}$$

where L is column length.

As general rule, more efficient columns have smaller H and more theoretical plates (N). The total number of theoretical plates can be also determined experimentally from an isothermal analysis by:

$$N = 16 \left(\frac{t_R}{w} \right)^2 \tag{3.5}$$

where t_R is the retention time and w is the width at the base of the peak (Fig. 3.1)
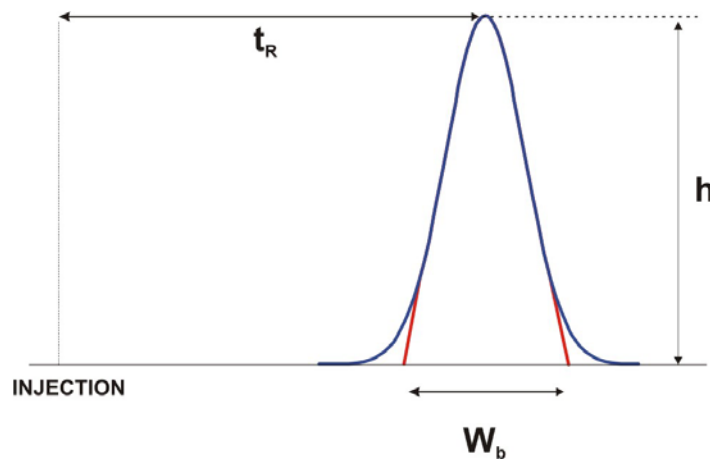
Fig. 3.1 - Experimental calculation of the theoretical plates number (N) by the full width at the base of the peak (w).

or by:

$$N = 5.545 \left(\frac{t_R}{w_h} \right)^2 \tag{3.6}$$

where w_h is the width of the peak at half height (Fig. 3.2).
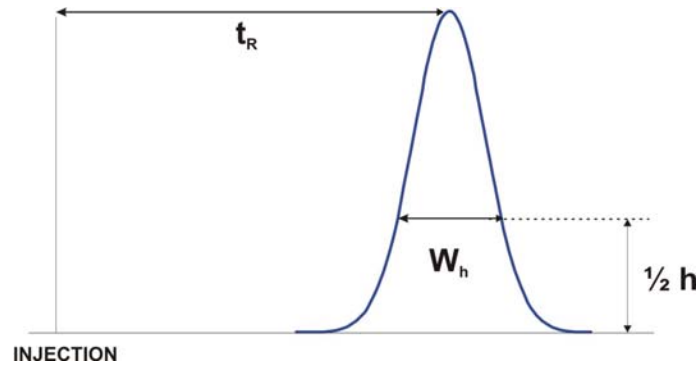
Fig. 3.2 - Experimental calculation of the theoretical plates number (N)
by the peak width at half height (w_h).

The term "effective plate number" N_{eff} was introduced to take into account the dead time (t_M) in the column when determining the efficiency:

$$N_{eff} = 5.545 \left(\frac{t_R - t_M}{w_h} \right)^2 \qquad (3.7)$$

The effective height-equivalent-to-a-theoretical-plate (H_{eff}) is then calculated by L / N_{eff} where L is the column length.

Another important parameter used for measuring the separation quality is the resolution. Resolution (R) is called overall separation efficiency, which is defined as the difference of retention time between two adjacent chromatographic peaks divided by the half of the sum of these two peak's bottom width (Fig. 3.3):

$$R = \frac{t_{R2} - t_{R1}}{\frac{1}{2}(w_1 + w_2)} = \frac{2(t_{R2} - t_{R1})}{w_1 + w_2} \qquad (3.8)$$
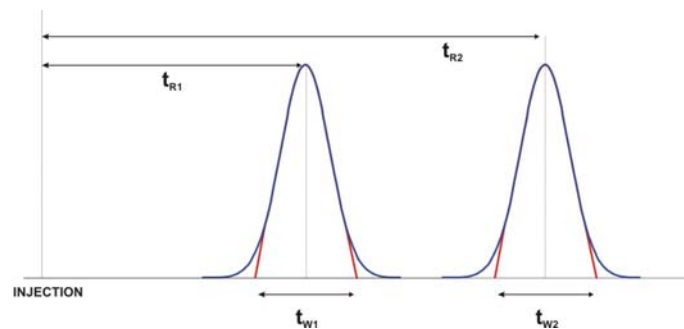
Fig. 3.3 - Resolution of the two adjacent chromatographic peaks.

The definition in Eq. (3.8) does not reflect all the factors which influence resolution, because it is effectively determined by column efficiency (N), selectivity factor (α) and capacity factor (k), hence the resolution also can be described by:

$$R = \left(\sqrt{\frac{N}{16}} \right) \left(\frac{\alpha - 1}{\alpha} \right) \left(\frac{k}{k+1} \right) \qquad (3.9)$$

Selectivity factor (α) is defined by Eq. (3.10):

$$\alpha = \frac{K_B}{K_A} \qquad (3.10)$$

where K is distribution constant for the solute A (less retained) and solute B (more retained) and it is defined as the concentration of a sample component in the stationary phase to its concentration in the mobile phase [3].

3.1.2 - HETP for Open Tubular Capillary Columns

The fundamental equation underlying the performance of a gas chromatographic column is the van Deemter expression which may be expressed as:

$$H = A + \frac{B}{u} + C\overline{u} \qquad (3.11)$$

where:

H = height equivalent to a theoretical plate.

A = multiple paths term. Constant that accounts for the effects of "eddy" diffusion in the column. The A term, generally used for packed columns, is not used with capillary columns because there is only one flow path and there is no packing material.

B = longitudinal diffusion contribution. Constant that accounts for the effect of molecular diffusion of the vapor in the direction of the column axis.

C = resistance to mass transfer term. Constant proportional to the resistance of the stationary phase to mass transfer of solute through it.

$\bar{u}$ = average linear velocity of carrier gas.

A representation of this equation (van Deemter plot) is given in Fig. 3.4, which shows the effect of *H* with changes in linear gas velocity.
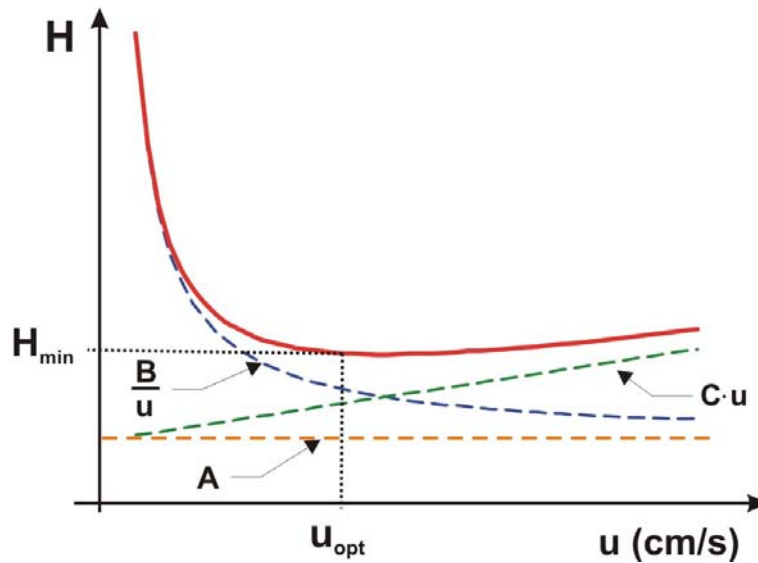
Fig. 3.4 - van Deemter plot.

Eq. (3.11) represents a hyperbole that has a minimum at velocity $u_{opt} = (B/C)^{1/2}$ and a minimum *H* (*H*_{min}) value at $A + 2(BC)^{1/2}$. The constants may be graphically calculated from van Deemter plot as shown in Fig. 3.4.

As reported previously, in the case of open tubular capillary column (OTC), *A* term (*A* = 2·d_p; where d_p is the particle size) is equal to zero because there is no packing material. Thus, Eq. (3.11) simplifies to:

$$H = \frac{B}{\bar{u}} + C\bar{u}$$
(3.12)

This abbreviated expression is often referred to as the *Golay equation*.

The B term may be expressed as:

$$B = \frac{2D_g}{\bar{u}}$$
(3.13)

where D_g is the binary diffusion coefficient of the solute in the carrier gas. Peak broadening due to longitudinal diffusion is a consequence of the residence time of the solute within the column and the nature of the carrier gas. This effect becomes relevant only at low linear velocities or flow rates and is less pronounced at high velocities.

However, the major contributing factor to band broadening is the C term, in which the resistance to mass transfer can be represented as the composite of the resistance to mass transfer in the mobile phase C_g and that in the stationary phase C_s:

$$C = C_g + C_s \qquad (3.14)$$

where [3]:

$$C_g = \frac{\left(1 + 6k + 11k^2\right)}{24\left(1+k\right)^2} \frac{r^2}{D_g} \qquad (3.15)$$

$$C_s = \frac{2}{3} \frac{k}{\left(1+k\right)^2} \frac{d_f^2}{D_s} \qquad (3.16)$$

where r is the capillary column radius, k is the solute retention factor, d_f is the stationary phase film thickness, and D_S is the diffusion coefficient of the solute in the stationary phase.

With open tubular capillary columns, C_S term is small and can be neglected. Hence the Golay equation may be rewritten as follow:

$$H = \frac{B}{\bar{u}} + C_g \bar{u} = \frac{2D_g}{\bar{u}} + \frac{1 + 6k + 11k^2}{24\left(1+k\right)^2} \frac{r^2}{D_g} \bar{u} \qquad (3.17)$$

Differentiation of Golay equation with respect to $\bar{u}$ leads to Equations (3.18) and (3.19) for the minimum height equivalent to a theoretical plate (H_{min}) and the optimal average carrier gas velocity ($\bar{u}_{opt}$) needed to achieve the minimum plate height:

$$H_{min} = r \sqrt{\frac{1 + 6k + 11k^2}{3\left(1+k\right)^2}} \qquad (3.18)$$

$$\bar{u}_{opt} = \frac{j D_g}{r} \sqrt{\frac{48(k+1)^2}{1+6k+11k^2}} \tag{3.19}$$

where j is the Martin-James gas compressibility correction factor for the column inlet and outlet pressures p_i and p_o respectively [4]:

$$j = \frac{3(P^2-1)}{2(P^3-1)} \tag{3.20}$$

$$P = \frac{p_i}{p_0} \tag{3.21}$$

From Eq. (3.18) it is clear that smaller column radius favors greater column efficiency (smaller plate height), and from the Eq. (3.19) that small column radius and large binary diffusion coefficients favor high optimal carrier gas velocity, both of which are desirable in HSGC. Hence both equations clearly illustrate the importance of smaller diameter column for high efficiency and fast analysis. Large u_{opt} values are important for high speed analysis since they allow for higher carrier gas flow rates without losses in column efficiency. The dependence of u_{opt} on the choice of carrier gas is shown in Eq. (3.19) and reflects the preference for the lighter molecular weight like hydrogen or helium [3].

Rewriting Eq. (3.17) corrected for the gas compressibility along the column, we have [3]:

$$H = \frac{2D_g}{\bar{u}} f j + \frac{1+6k+11k^2}{24(1+k)^2} \frac{r^2}{D_g} \frac{f}{j} \bar{u} \tag{3.22}$$

where f is the Golay-Giddings gas compressibility factor defined as [5-7]:

$$f = \frac{9}{8} \frac{(P^4-1)(P^2-1)}{(P^3-1)^2} \tag{3.23}$$

Hence the efficiency of a capillary column is dependent on the carrier gas used, the length and inner diameter of the column, the retention factor of the particular solute

selected for the calculation of the number of theoretical plates, and the film thickness of stationary phase [3].

3.2 - COLUMN DESIGN, FABRICATION AND INTERCONNECTION

As reported in Chapter 2, most of the microfabricated GC columns are formed by silicon channels with rectangular cross-section sealed by a Pyrex® wafer. However, microcolumns with sharp corners show lower performance compared to conventional columns because of stationary phase accumulation in the corners (see Fig. 2.5). To overcome this problem a silicon micromachined capillary column with nearly circular cross-section has been designed according to the technological and microfluidic constraints. The column parameters have been determined starting from both theoretical and practical considerations. According HSGC theory (see section 3.1), short column length reduces analysis time and small inner diameter (ID) enhances the column resolution.

By this purpose, an all-silicon 2 meter-long capillary columns obtained through MEMS technology have been designed and fabricated to be employed in a miniaturized HSGC system. The twelve 2 cm square capillary columns chips are contained on a 4-inches silicon wafer as illustrated in Fig. 3.5.
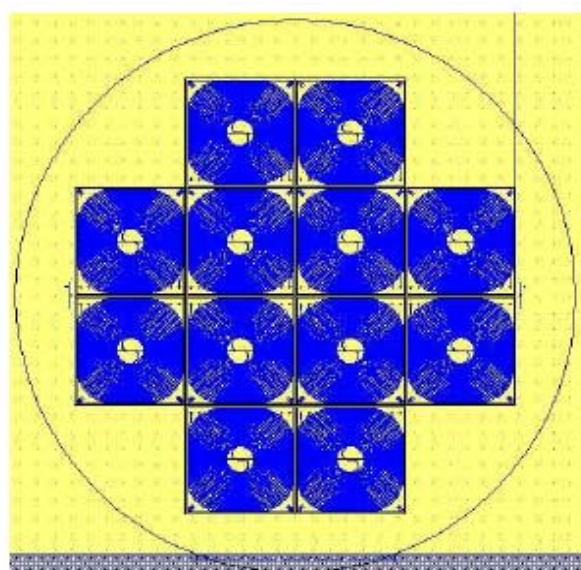
Fig. 3.5 - Twelve microcolumns chips placement over the wafer surface (mask layout).

Going into detail (Fig. 3.6), the microchannels configuration, forming the double spiral-shaped microcolumn, presents a circular cross-section with an ID = 100 µm.
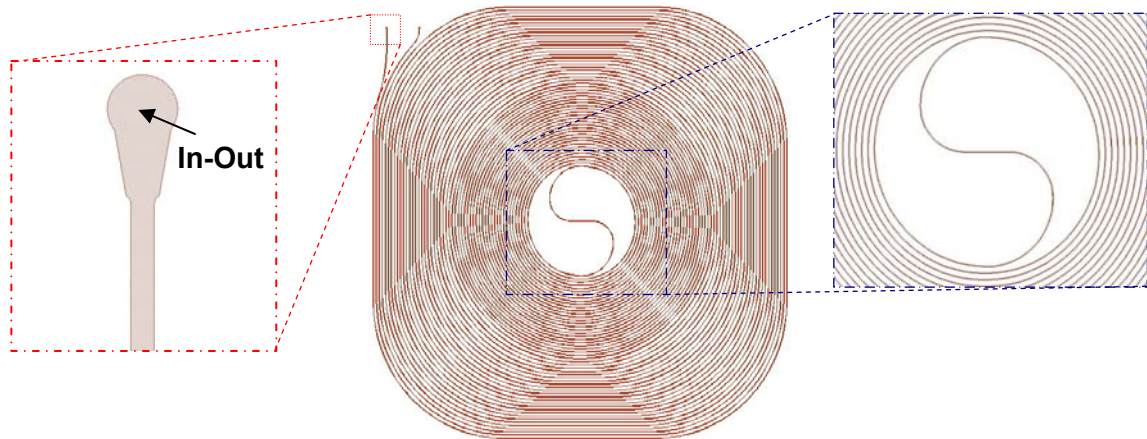
Fig. 3.6 - Double spiral-shaped MEMS column: details of In-Out hole (left) and central 'S' - section (right).

In Fig. 3.7, the main process steps for both the fabrication of the circular section spiral-formed microchannels and the in-outlet holes are reported and they are based on a proper sequence of anistropic/isotropic DRIE etching (see sections 1.1.4 and 1.1.5).

The sequence involves 500 µm and 300 µm thick double-side polished (DSP) 4 inch silicon wafers: on wafer A the circular cross-section microchannels have been realized (Fig. 3.7 steps A - F) while on wafer B the interconnection vias have been fabricated (Fig. 3.7 steps G - I). Then the wafers have been jointed by a SiO_2/SiO_2 high temperature hydrophilic fusion bonding (Fig. 3.7 step L). Finally, the last steps have been the opening of the via holes (Fig. 3.7 steps M - N).

The process flow for the fabrication of the microchannels (Wafer A) consists of the following main steps (Fig. 3.7 A - F):

A) A 2 µm thick Low Pressure Chemical Vapor Deposition (LPCVD) Low Temperature Oxide (LTO) layer has been deposited using SiH_4 and O_2 as precursor gases.

WAFER A

A) LTO deposition

B) LTO and anisotropic D-RIE silicon etching

C) Polysilicon LPCVD deposition and oxidation

D) SiO$_2$ RIE etchback

E) SF$_6$-Based ICP isotropic silicon etching

F) Hard mask wet etching and thin thermal oxide film grown

WAFER B

G) LTO deposition

H) LTO D-RIE etching

I) D-RIE silicon etching and thin thermal oxide film grown

WAFER A+B

L) Fusion bonding process

M) Patternig and vias opening

N) Wafer Cleaning by Plasma oxygen

Fig. 3.7 - Brief schematic outline of the fabrication process used to create circular microcolumns. More detailed process information is provided in the text.

B) The thin SiO$_2$ film has been patterned by a 4 µm thick OiR-908 positive photoresist and etched by an Inductively Coupled Plasma (ICP) C$_4$F$_8$/CH$_4$/He based plasma. Next, a 28 µm deep vertical sidewall trench has been realized by a Bosch® DRIE process.

C) Before realizing the microchannels into silicon substrate by isotropic silicon etching, the sidewalls of the structure have been protected by depositing a thin thermal oxide layer.

D) The grown thin oxide layer has been anisotropically removed by CHF$_3$/Ar RIE etching from the trench bottom, leaving the sidewall undisturbed.

E) The circular microchannels have been subsequently formed by an isotropic silicon etching using a fluorine-based high density plasma.

F) The hard mask and the sidewall protection were subsequently wet etched by a 10% wt. HF solution.

In Fig. 3.8 a SEM cross-section view of the fabricated microchannels and a detail of the circular shape microchannel are shown.

The silicon buried microchannels have been sealed by a second silicon wafer (wafer B) containing wafer-through holes. The inlet vias are perpendicular to the microchannels wafer and the microfluidic interconnections have been made at chip level by fused silica capillaries having ID =100 μm, and OD = 170 μm (Fig. 3.9).

The silicon vias (170 μm width) have been matched to the outer diameter of the capillary and in order to obtain as good as possible pneumatic interconnection, the holes have a tapered shape and have been realized by a modified Bosch® process.

In this way a press-fit like interconnection has been obtained. In the conventional GC, press-fit connectors are made out of borosilicate glass to connect two or more capillary columns having different inner and/or outer diameters.
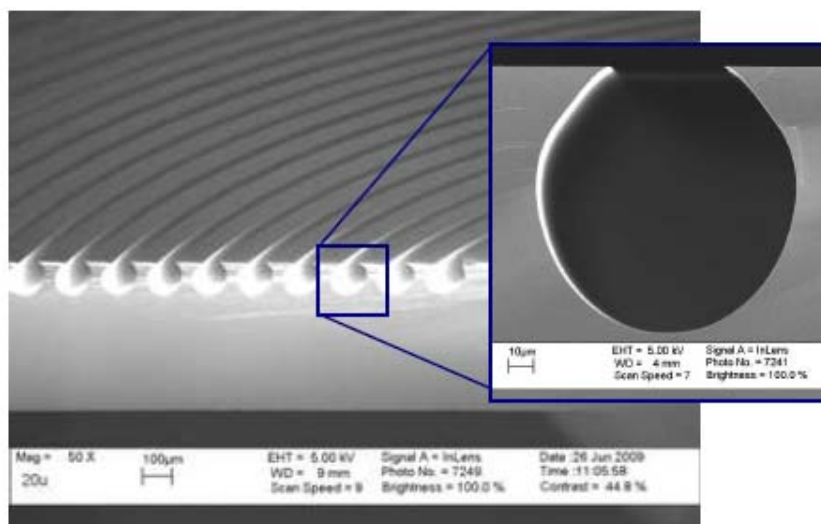
Fig. 3.8 - SEM image of cross-section circular microchannels.

Press-fit connectors, having a conical wall, allow both the attachment of the capillary column and the mechanical seal (Fig. 3.9).
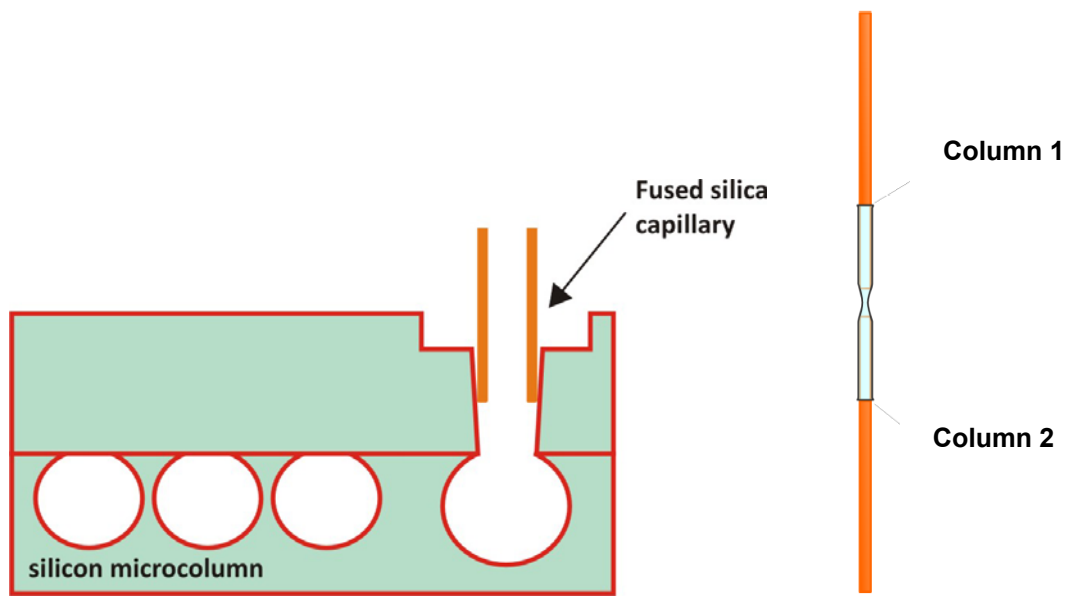
Fig. 3.9 - Press-fit like interconnection (left) and a conventional GC press-fit union (right).

The process flow for the fabrication of the interconnections vias (wafer B) consists of the following steps (Fig. 3.7 G - I):

G) A 3 µm thick layer of Low Temperature Oxide (LTO) have been deposited by Low Pressure Chemical Vapor Deposition (LPCVD) vertical furnace.

H) The thin silicon dioxide has been patterned by 4 µm positive photoresist thick and etched by DRIE.

I) 420 µm-deep holes have been realized by a modified Bosch® recipe. Subsequently, the wafer has been cleaned by oxygen plasma and EKC 830 solvent in order to remove the DRIE polymer and photoresist. The LTO hard mask was wet etched by hydrofluoric acid.

Subsequently wafer A and wafer B have been joined together and via holes have been opened. The process flow consists of the following steps (Fig. 3.7 L - N).

L) The microcolumns and via interconnections wafers have been then thermally oxidized in order to obtain microchannels with a hydrophilic surfaces. Then the wafers were jointed by a SiO_2/SiO_2 fusion bonding process.

M) Opening of the via holes by patterning the silicon dioxide and silicon by wet etching and DRIE respectively.

N) Removing of the photoresist by a plasma oxygen.
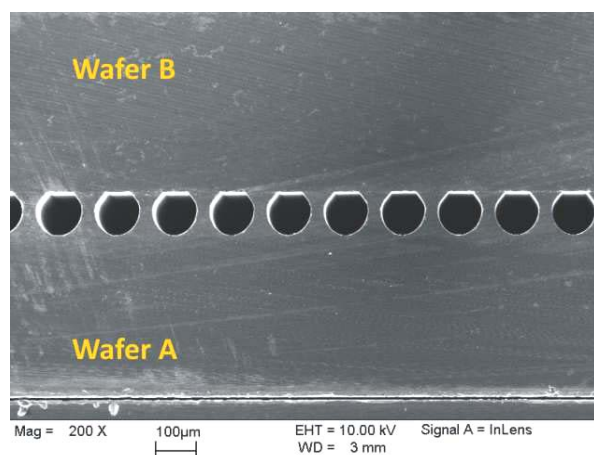
Fig. 3.10 - SEM image showing the all-silicon 100 μm diameter circular microcolumn cross-section. The silicon buried microchannels (wafer A) have been sealed by a second silicon wafer (wafer B).

Fig. 3.10 shows a SEM image of the fabricated all-silicon circular section buried microcolumns. The average diameter has been measured to be 100 μm.

Finally the single chips have been separated by a dicing saw. In the Fig. 3.11 a micromachined capillary column fabricated at CNR-IMM Bologna is shown.
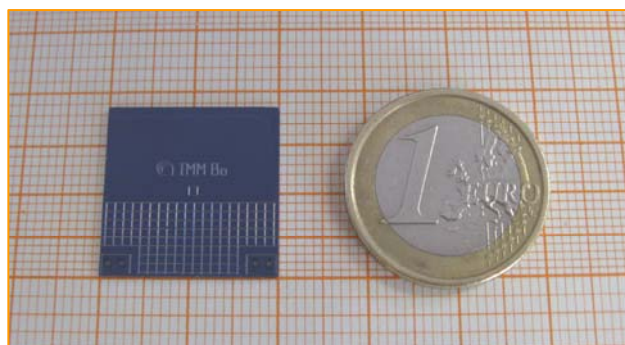
Fig. 3.11 - A CNR-IMM micromachined GC column compared with 1 euro coin.

The covering wafer has been micromachined to define the inlet/outlet holes where two fused silica capillaries (the interconnections of the capillary column chip with the other blocks of the system) are introduced and sealed to the silicon wafer with an appropriate glue.

In particular for favoring glue adhesion to silicon, the wafer surface has been micro-machined in correspondence of In-Out holes, aimed at defining circular concentric structures characterized by a high degree of roughness, obtained through DRIE etching (etch average depth = 60 μm) [8]. An optical micrograph of the circular structures is presented in Fig. 3.12:
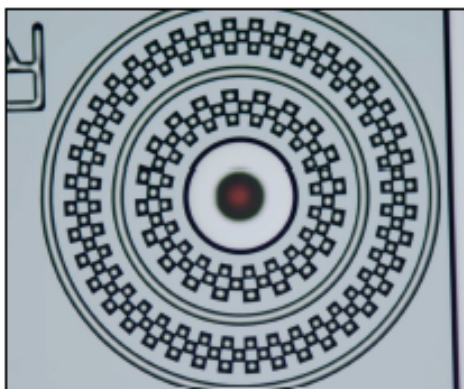
Fig. 3.12 - Optical micrograph of the micromachined circular geometries [8].

A polyimide resin (Pyrolin® Polyimide Coating, Supelco, Bellefonte PA) has been chosen as adhesive because polyimides are noted for their excellent thermal and radiation resistance properties resulting directly from their highly aromatic polymer structures. In addition also the fused silica connections tubing are covered with polyimide resin to make them stronger and more flexible.

In some works presented in literature [9-11] the microcolumn has been fluidically connected to the capillaries via Nanoport® (Upchurch Scientific) fitting. Although this connection mode is easy and ready to use, it is not suitable for high temperatures that the microcolumn can sometimes reach during both functionalization process and analysis. In fact the maximum operating temperature of the Nanoport® fitting not exceed 150 °C. Polyimde resin employed here, instead, is stable up to 350 °C.

Polyimides are formed from polyamic acid or polyamic ester precursors by heating to temperatures as high as 400 °C.

Polyimide precursors are synthesizes by reacting equimolar amounts of aromatic diamines with aromatic dianhydrides forming polyamic acids or polyamic ester as in Fig. 3.13a.
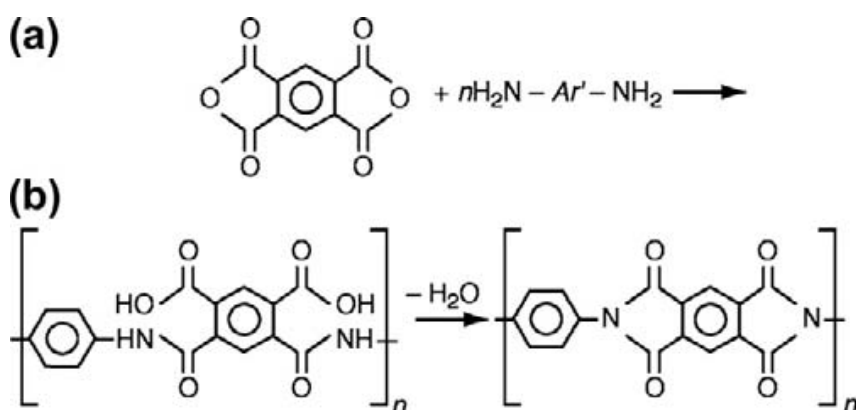
Fig. 3.13 - Polyimide reactions: preparation of polyimide precursors (a);
curing of polyimides by imidization (b) [12].

Curing is not the traditional crosslinking or chain propagation using curing agents, but it occurs by heating to eliminate water and close the imide rings along the chain forming the very stable polyimide structure (Fig. 3.13b). The process of ring closure is known as *imidization* and requires step curing, which, in our case is from 40 °C to 200 °C at 5 °C/minute, followed by 10 minutes at 200 °C.

The initial temperature exposure assures the removal of the N-methyl-2-pyrrolidone (NMP), a solvent that is present in almost all polyimide precursor formulation [12].

In Fig. 3.14 a 2 cm square microcolumn chip with inlet/outlet fused silica capillaries is shown on the left, while a micrograph of fused silica capillaries introduced into inlet/outlet holes and sealed with glue is shown on the right.

Capillaries with outer diameter of 170 µm and inner diameter of 100 µm have been chosen to be insert into the holes for a depth more than twice their diameter (~ 400 µm), increasing the interconnection mechanical robustness.
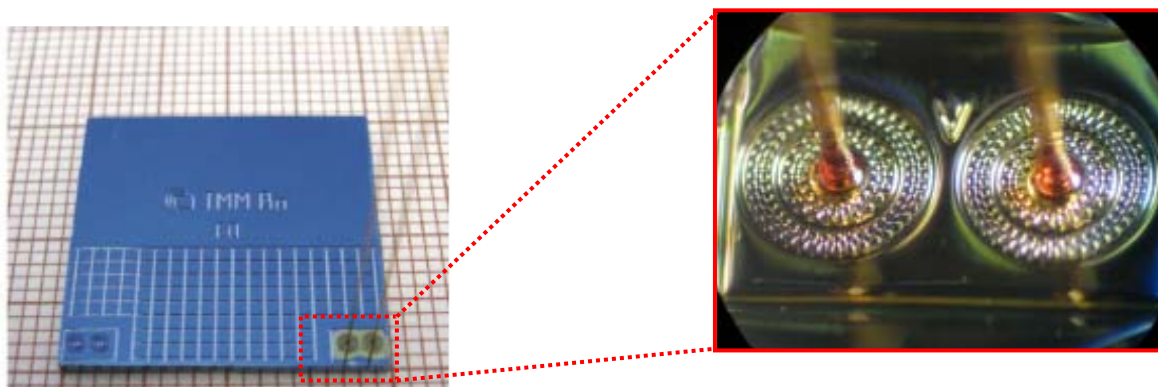
Fig. 3.14 - Images showing a 2 cm square microcolumn chip with inlet/outlet fused silica
capillaries (left); detail of fused silica capillaries introduced into
in/out holes and sealed with polyimide resin (right).

3.3 - EXPERIMENTAL RESULTS

In this section, experimental results obtained with the MEMS capillary columns are reported. After a short description of the microfabricated capillary columns characterization, both Grob Test chromatograms and real samples chromatograms are discussed.

3.3.1 - MEMS Columns Characterization

Prior to stationary phase introduction into the capillary columns, every chip has been subjected to two tests, performed at room temperature, for verifying the presence of leaks and for measuring the volumetric flux. To this purpose, the column inlet capillary has been connected to a laboratory pipeline supplying nitrogen, while the microcolumn has been placed into a beaker filled with de-ionized water (see Fig. 3.15). By means of a pressure sensor and a relief valve, nitrogen flow entered the inlet capillary at different pressure values (from ambient pressure to a maximum of ~ 7 bar, constantly keeping outlet capillary at ambient pressure), allowing to check for the presence of any bubbles in the beaker, index of microcolumn fluidic leakage. Volumetric flux test has been performed in order to check possible defects due to fabrication process (i.e. microchannels tight spots or melting points). For different pressure value the time employed by nitrogen flow to travel the whole column length has been measured.
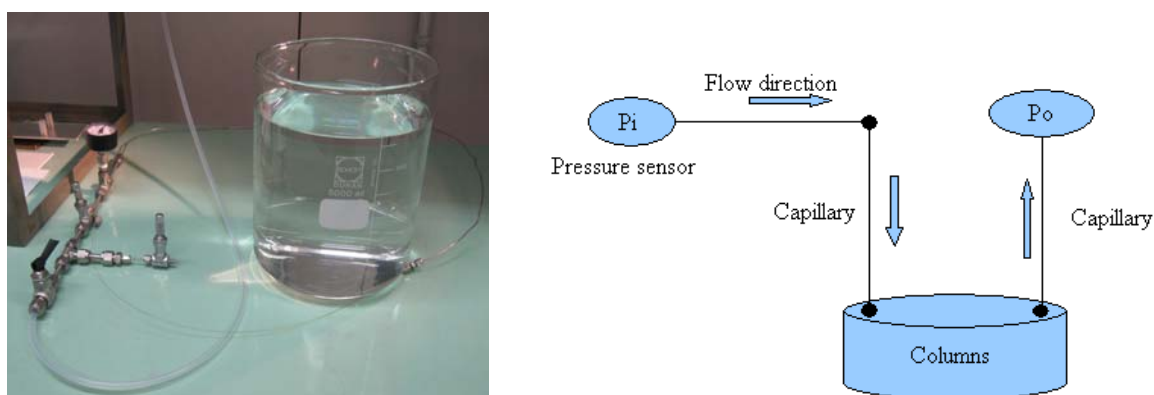
Fig. 3.15 - Experimental set-up (left) and schematic representation (right) for fluidic tests.

Finally thermal stress test has been done for verifying the interconnections resistance to high temperature (up to 300 °C) and pressure (~ 7 bar).

3.3.2 - Stationary Phase Coating

Stationary phase deposition has been performed with the procedures usually adopted for wall-coated open-tubular fused-silica columns (WCOT) after the deactivation treatment of the interior microcolumns surface.

Generally, the deactivation process is performed to reduce surface activity and improve adhesion of the stationary phase to the channel walls. In fact without any pre-treatment of the interior surface, the tendency of the stationary phase to form minute droplets rather than a uniform coating was observed. This depends on the balance between the interfacial surface tension of the phase and the tube surface and the intrinsic surface tension of the phase itself. Polar liquids, which usually have higher surface tensions, are more likely to give this problem. Droplet formation results in a poor column performance, because of slower mass transfer and adsorption at uncovered active sites between the droplets. Another problem is the presence of active sites. They are usually silanol groups at the silica surface, which can interact with the polar groups of the sample. Absorption effects at these sites reduce the resolution of the column. For this reason, an effective deactivation treatment is mandatory during column preparation [13].

There are two methods more frequently used for the production of WCOT: dynamic coating and static coating.

With the first, a plug of stationary phase in a suitable solvent is pushed through the column by the flow of a inert gas. Stationary phase film thickness can be controlled by means of the plug velocity and the stationary phase concentration in the solvent. After the plug is expelled from the end of the column, the excess solvent is evaporated by continued gas flow leaving behind a film of stationary phase on the wall of the fused-silica tube.

For static coating, the entire column is filled with the stationary phase solution, one end is sealed, and a vacuum applied to the open end. A front representing the liquid-vapor transition point propagates through the column away from the low-pressure end. The coating is complete once the solvent is completely pumped away.

Static coating usually is preferred over dynamic coating for two reasons. First, all of the stationary phase initially introduced is deposited on the column wall; thus, the calculation of average film thickness is straightforward, using the surface area of the column, the concentration of stationary phase in the solution, and the density of the stationary phase. Second, the stationary phase coating may be more uniform than with dynamic coating due to the lack of axial motion of the stationary phase during deposition [14].

The deactivation and functionalization processes have been performed by MEGA s.n.c. (Legnano, Milano, Italy). It should be stressed that the process steps will not be described in detail since MEGA s.n.c. has not given consent to their pubblication.

Every microcolumn has been treated with concentrated hydrochloric acid to enhance the wettability of the microchannels' inner surface. The second step has been the conversion of the silanol groups to methyl groups with silylating agent such as hexamethyldisilazane (HMDS). Once the deactivation process has been carried out, column was ready for the functionalization.

All the microcolumns have been filled by a static coating method with a known concentration of stationary phase in a volatile solvent. The film thickness of the stationary phase has been calculated from the weight and density of the solution used to fill them. The microcolumns have been functionalized by a non-polar and polar stationary phases.

3.3.3 - MEMS Columns Performance Testing

Microcolumns have been extensively characterized on a standard gas chromatographic benchmark mixture, named Grob test, for monitoring their performance. Grob test mixture (contents listed in Tab. 3.1) is a diagnostic mixture containing various classes of organic components including hydrocarbons, fatty acids methyl esters (FAMEs), alcohols, acids and bases.

These compounds, having different functional groups which encompass acidic/basic and polar/apolar structures, interact in different ways with the stationary phase. Thereby Grob test provides information about important aspects of column quality such as separation efficiency, adsorptive activity, acidity/basicity and stationary film thickness [3].

A Thermo Scientific Focus GC/FID system has been used for all experiments. The conventional capillary column inside the gas chromatograph has been replaced by the MEMS columns (2-m-long; 100-µm-ID) and the microdevices have been connected to a split/splitless injection system and to a flame ionization detector.
Hereafter Grob test chromatograms of the microcolumns functionalized with both non-polar and polar stationary phase are shown. In addition the chromatograms of real samples analyses are also reported.

3.3.3.1 - Non-polar stationary phase

In the first test, a microfabricated capillary column (named **MC1**) has been functionalized with SE-52 (5% phenyl 95% dimethylpolysiloxane) stationary phase. The coating thickness has been calculated to be about 0.1 µm. The injection volume of of Grob test mixture has been 1 µL.

Probe	Function
2,3 butanediol (D)	More rigorous test of silanol detection
n-decane (10)	Column efficiency
1-octanol (OI)	Detection of silanol groups
2,6-dimethylphenol (P)	Acid-base behavior
2-ethylexanoic acid (S)	More stringent test of acid-base character
2,6-dimethylaniline (A)	Acid-base character
n-dodecane (12)	Column efficiency
methyl decanoate (E10)	Column efficiency
dicycloexylamine (Am)	More stringent test of acid-base character
methyl undecanoate (E11)	Column efficiency
methyl dodecanoate (E12)	Column efficiency

Tab. 3.1 - Grob Test components and role. Abbreviations of the components in the Grob mix are indicated in parentheses.

The chromatographic conditions are reported in Tab. 3.2 and hydrogen has been used as carrier gas at constant pressure of 70 kPa.

Injector mode	split
Split Flow	80 mL/min
Injector Temperature	250 °C
Oven program	40 °C, 10 °C/min
FID Temperature	250 °C

*Tab. 3.2 - Gas chromatographic conditions for Grob test analysis on microcolumns **MC1** and **MC2** coated by ~ 0.1-µm-thick SE-5 stationary phase.*

In Fig. 3.16 Grob test chromatogram is shown. The plot suggests that microcolumn **MC1** has a good efficiency based on *n*-alkanes and FAMEs peaks shape. There is some tailing in the polar compounds peaks indicating the presence of some active sites (such as silanol groups) in the microcolumn. The reason is expected to be in a non-optimal deactivation process. This problem could be overcome by increasing the stationary phase thickness.
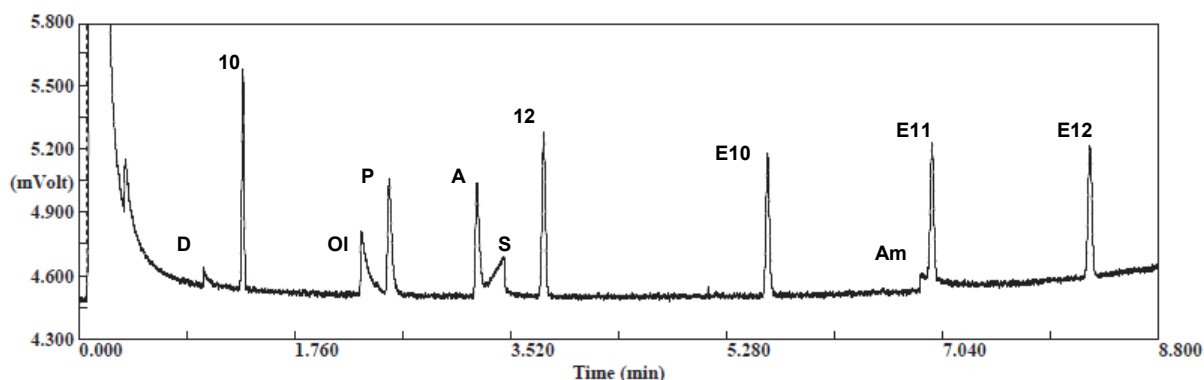
*Fig. 3.16 - Grob test mixture chromatogram on microcolumn **MC1** coated by ~ 0.1-µm-thick SE-52 stationary phase. Peaks name are listed in Tab. 3.1.*

In addition the microcolumn has poor chemical inertness based on aliphatic amine peaks shape.

Finally the peak shape of 2-ethylexanoic acid (S) is similar in commercial fused-silica capillary columns coated with the same stationary phase (see Fig. 3.17).
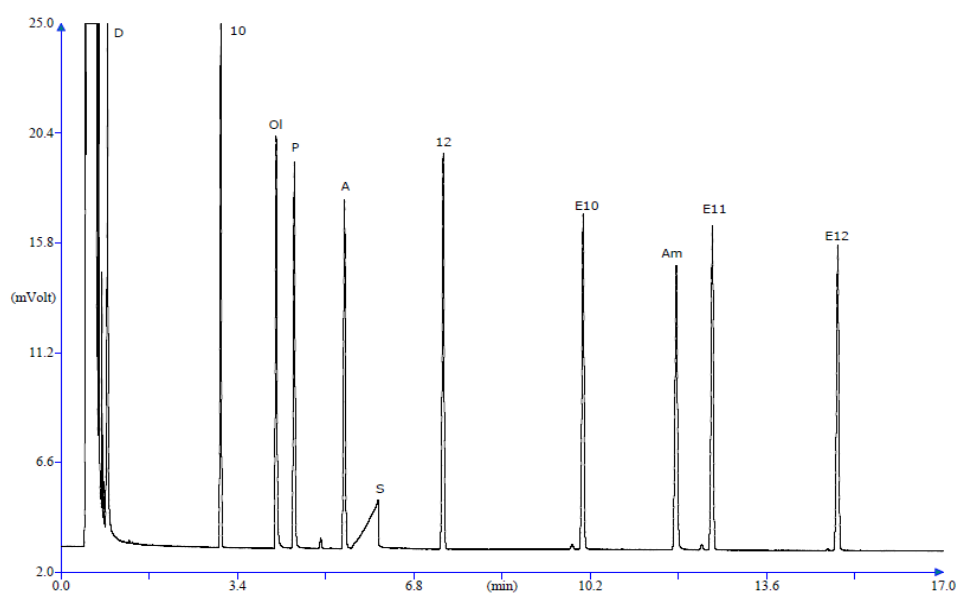
Fig. 3.17 - Chromatogram of Grob test mixture showing the performance of 10-m-long, 250-µm-ID commercially column coated by 0.10-µm-thick non-polar stationary phase.

In order to verify the reliability of the analytical data, another microcolumn (named **MC2**) has been functionalized with the same stationary phase (0.1-µm-thick layer). The injection volume of Grob test mixture has been 1 µL. Hydrogen has been used as carrier gas at constant pressure of 70 kPa. The experimental conditions are listed in Tab. 3.2. The chromatogram is reported in Fig. 3.18:
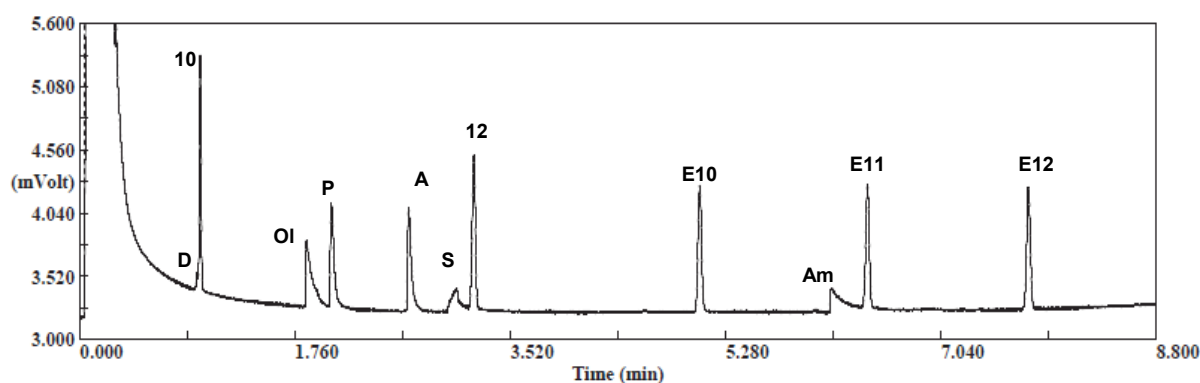
Fig. 3.18 - Grob test mixture chromatogram on microcolumn **MC2** coated by ~ 0.1-µm-thick SE-52 stationary phase.

All components have been separated with an acceptable resolution. Since the coating performance has been found to be the same as those obtained with microlcolumn **MC1**, this suggests that active sites still exist on the surface of the

microchannels. Hence the next step has been to increase the stationary phase thickness.

As reported in section 3.1, the performance of a capillary column is conventionally measured in terms of effective number of theoretical plates (N_{eff}), a measure of the resolving power of the column. The effective number of theoretical plates has been calculated experimentally by using the Eq. (3.7).

For the microcolumns, the number of theoretical plates has been calculated from isothermal separation (110 °C) based on the methyl dodecanoate peak (E12) at constant pressure of 60 kPa.

A two-meter long column and 100 μm ID is expected to have approximately 20000 theoretical plates, and MEMS HSGC prototypes have yielded an average number of plates greater than 19000 on Grob test mixture. Fig. 3.19 shows the height-equivalent-to-a-theoretical-plate (H) as a function of the average carrier gas velocity using methyl dodecanoate at 110 °C. Minimum height equivalent to a theoretical plate (H_{min}) is achieved at an optimal flow velocity of 0.270 mL/min corresponding to a linear velocity of about 57 cm/s.
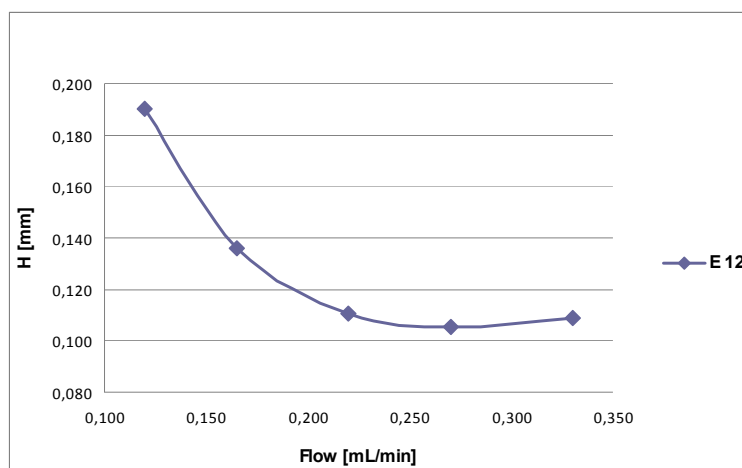
*Fig. 3.19 - van Deemter plot for 2-m-lomg column generated from
an isothermal run using methyl dodecanoate at 110 °C.*

Furthermore, a comparison between experimental and theoretical data derived from the GC theory (see section 3.1.2) has been performed. In particular, the minimum height equivalent to a theoretical plate (H_{min}) and the optimal average carrier gas velocity ($\bar{u}_{opt}$) values have been calculated using Equations (3.18) and (3.19),

respectively. By this purpose, the methyl dodecanoate retention factor (k_{E12}) has been calculated using Eq. (3.2). Since the holdup time has been of 0.038 min and the E12 retention time has been 2.31 min, k_{E12} has been calculated to be about 60 under isothermal operating conditions. In the following tables, a comparison between theoretical and experimental values for H_{min} and $\bar{u}_{opt}$ is reported, assuming the microcolumn mean radius (r) of 50 µm.

Minimum height equivalent to a theoretical plate (H_{min})		Theoretical value (mm)	Experimental value (mm)
$H_{min} = r\sqrt{\dfrac{1+6k+11k^2}{3(1+k)^2}}$	(3.18)	0.095	0.105

Tab. 3.3 - Comparison between H_{min} theoretical and experimental values.

Using the Fuller-Schettler-Giddings equation [15], the diffusion coefficient of the E12 in hydrogen (D_g) at 110 °C has been calculated to be about 0.2 cm^2/s. The Martin-James gas compressibility correction factor (j) has been calculated using Eq. (3.20).

Optimal average carrier gas velocity ($\bar{u}_{opt}$)		Theoretical value (cm/s)	Experimental value (cm/s)
$\bar{u}_{opt} = \dfrac{jD_g}{r}\sqrt{\dfrac{48(k+1)^2}{1+6k+11k^2}}$	(3.19)	64	57

Tab. 3.4 - Comparison between $\bar{u}_{opt}$ theoretical and experimental values.

As can be easily disclosed from the Tables 3.3 and 3.4, the experimental values are very close to the theoretical ones.

The next step has been the analysis of real samples, specifically 1µL of a *Citrus Bergamia* essential oil has been injected into the microcolumn **MC2**.

Injector mode	split
Split Flow	100 mL/min
Injector Temperature	250 °C
Oven program	45 °C (0.5 min), 15 °C/min
FID Temperature	250 °C

Tab. 3.5 - Gas chromatographic conditions for Citrus Bergamia
*essential oil analysis on microcolumn **MC2**.*

The chromatographic conditions used for the analysis are listed in Tab. 3.5 and helium has been used as carrier gas at constant pressure of 50 kPa.

Peak #	Compound
1	α-Pinene
2	β-Pinene
3	Mycene
4	p-Cimene
5	Limonene
6	γ-Terpinene
7	Linalol
8	Lynalil Acetate

Tab. 3.6 - Components of Citrus Bergamia essential oil.

The components of the *Citrus Bergamia* essential oil are listed in Tab. 3.6.

In Fig. 3.20 the chromatogram is shown: the elution time has been less than four minutes and all the peaks are well defined and resolved. The peak shape of p-cimene (4) is similar in commercial fused-silica capillary columns coated with the same stationary phase (see Fig. 3.21).

Comparing the previous chromatogram with the one obtained by injecting 1 µL of the same essential oil in a conventional capillary column (5-m-long, 100-µm-ID; 0.1 µm film thickness), which is longer than the microcolumn **MC2**, one can notice that the results are reproduced perfectly (see Fig. 3.20).
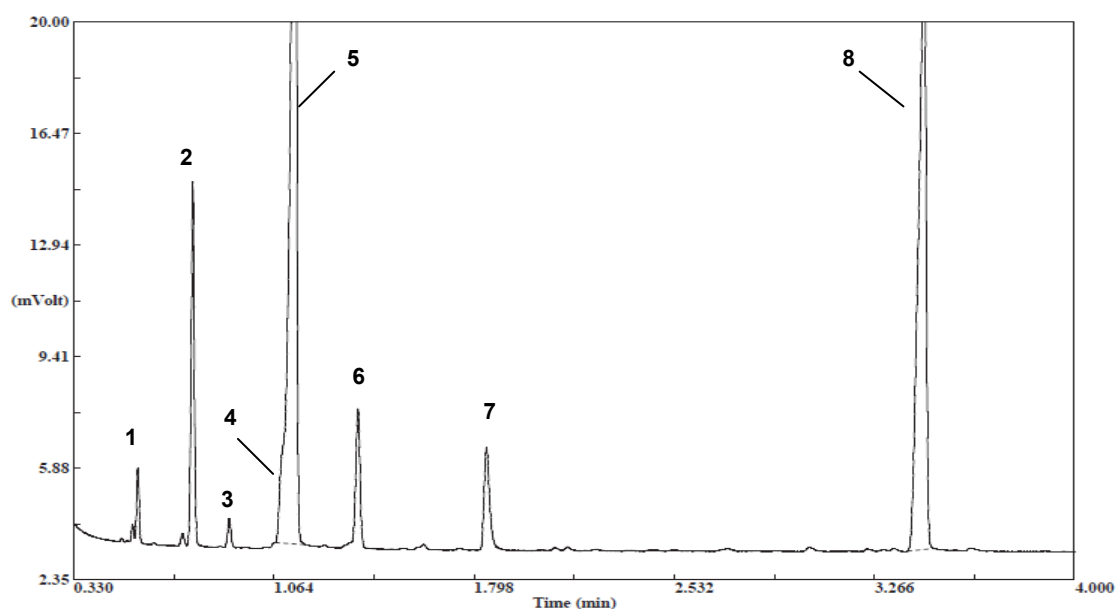
Fig. 3.20 - Citrus Bergamia essential oil on microcolumn MC2.

In order to avoid polar compounds peak tailing, next microcolumn (named **MC3**) has been functionalized increasing the stationary phase thickness, from 0.1 µm to 1 µm. This has been done for covering some defects related to the deactivation treatment. Hydrogen has been used as carrier gas.
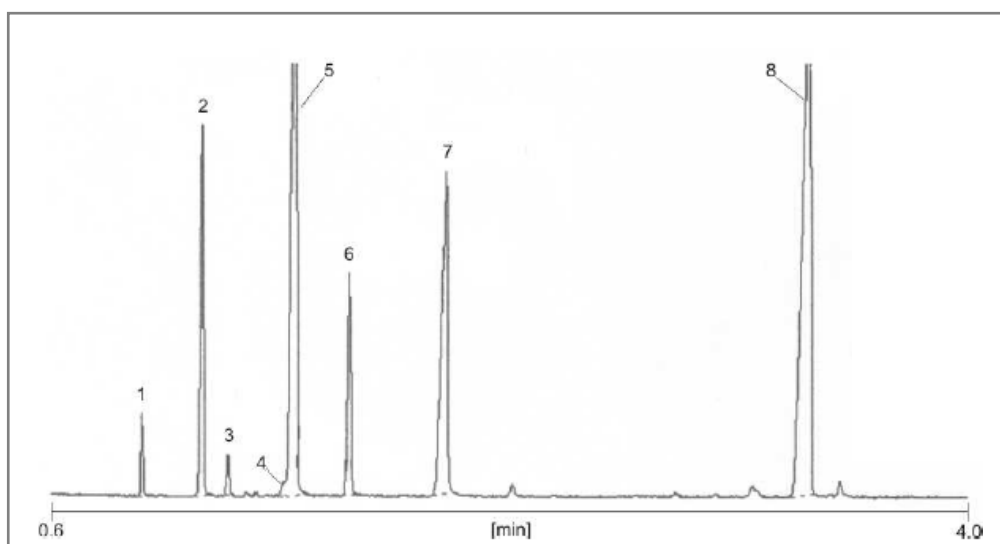
Fig. 3.21 - Citrus Bergamia essential oil on 5-m long, 100 µm ID fused-silica capillary column.

The chromatographic conditions are reported in Tab. 3.7.

Fig. 3.22 shows the chromatogram obtained by an injection volume of 1 µL of Grob test mixture.

Injector mode	split
Injector Temperature	250 °C
Oven ramp	40 °C to 200 °C (20 °C/min)
FID Temperature	250 °C
H_2 Pressure	75 kPa
Flow rate	60 mL/min

*Tab. 3.7 - Gas chromatographic conditions for Grob test chromatogram on microcolumn **MC3** coated by 1-µm-thick SE-5 stationary phase.*

The microcolumn has been able to separate all the components of the mixture and the individual peaks have been resolved with a marked symmetrical appearance. In addition no peak tailing has been observed, suggesting the absence of free silanol groups on microchannels walls.
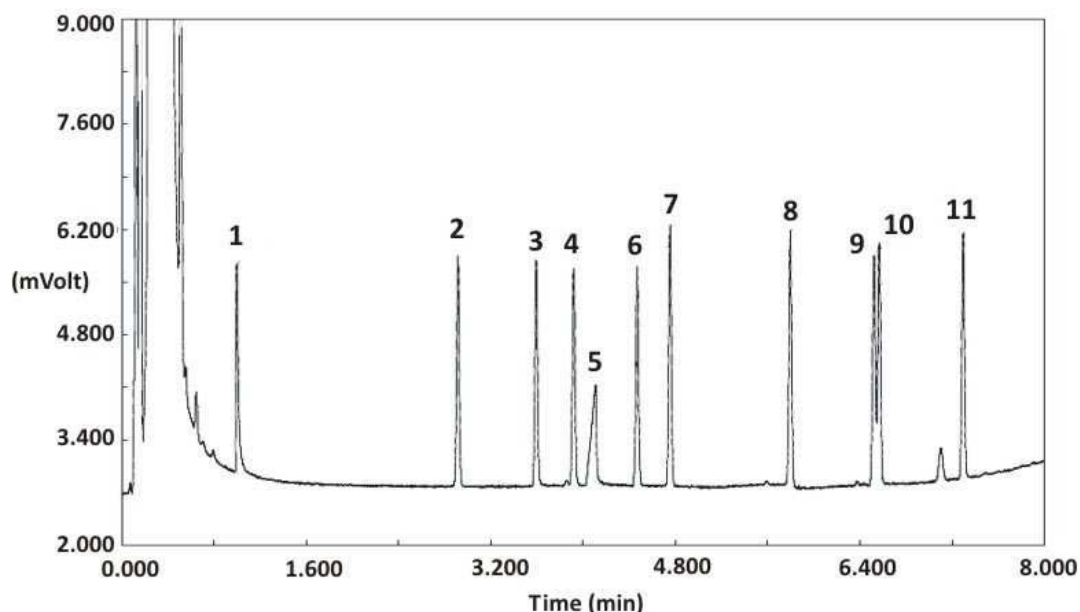
*Fig. 3.22 - Grob test mixture chromatogram on microcolumn **MC3** coated by 1-µm-thick SE-5 stationary phase.*

The presence of acids and bases peaks indicates that the proposed MEMS capillary microcolumn is chemically inert. The performance of the microcolumn has been also tested by analyzing a benzene, toluene and xylene (BTX) mixture. Hydrogen has been used as carrier gas. The chromatographic conditions are listed in Tab. 3.8.

Injector mode	split
Injector Temperature	250 °C
Oven	50 °C
FID Temperature	250 °C
H_2 Pressure	60 kPa
Flow rate	60 mL/min

Tab. 3.8 - BTX mixture chromatographic conditions
*on microcolumn **MC3**.*

The chromatogram of the 1 µL of BTX mixture is shown in Fig. 3.23. The analytes have been separated in less than 150 seconds. The peaks are symmetric and well resolved. It is important to note that the two xylene isomers (m/p-xylene, superimposed in peak 4) are difficult to separate with any column.
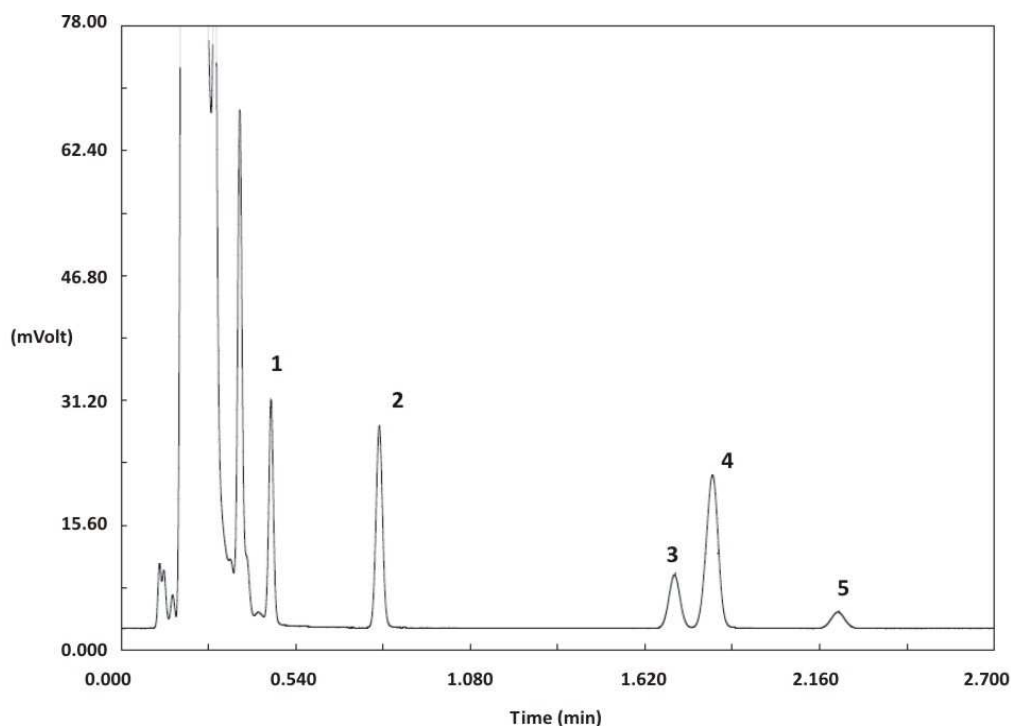
Fig. 3.23 - Separation of benzene (1), toluene (2), ethylbenzene (3),
*m/p-xylene (4), o-xylene (5) mixture on microcolumn **MC3**.*

3.3.3.2 - Polar Stationary Phase

Another experiment has been performed functionalizing a new column (named **MC4**) with polar stationary phase, specifically Carbowax, having 0.2 μm coating thickness. The chromatographic conditions are reported in Tab. 3.9.

Split Flow	80 mL/min
Injector Temperature	250 °C
Oven	40°C, 20 °C/min, 150 °C
FID Temperature	250 °C
H_2 Constant Pressure	50 kPa

*Tab. 3.9 - Gas chromatographic conditions for Grob test chromatogram on microcolumn **MC4**.*

From Fig. 3.24, peak shape and column inertness are good. Peaks are well defined and resolved and there is no tailing. The peaks name and the function of each compound are both explained in Tab. 3.1.
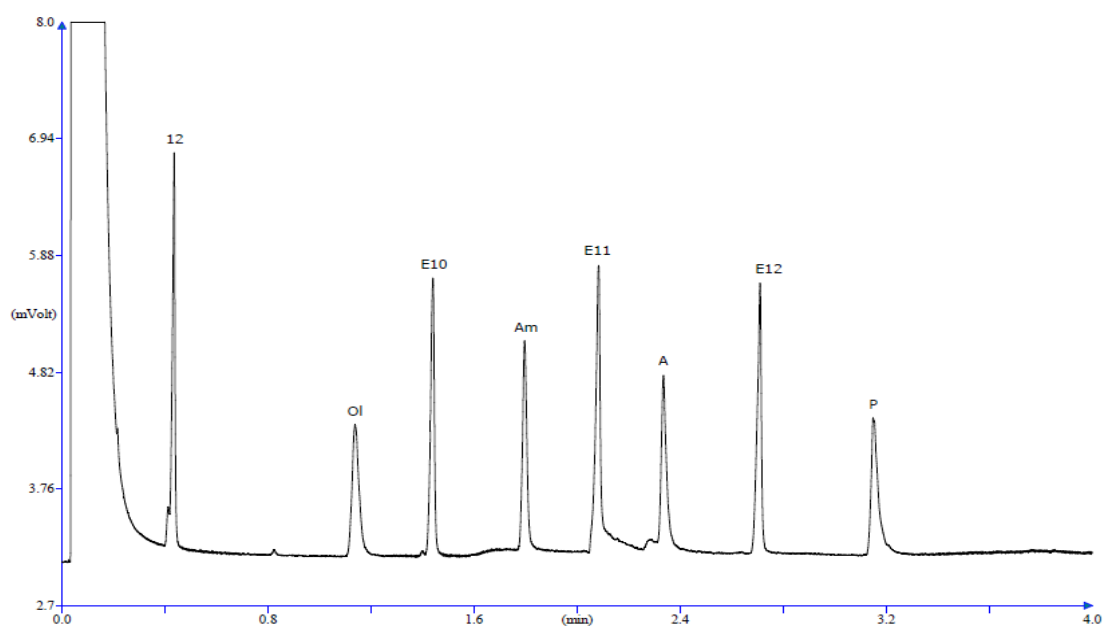
*Fig. 3.24 - Grob test mixture on microcolumn **MC4** coated by a polar stationary phase.*

Comparing the above chromatogram with one obtained from a standard capillary column, functionalized with the same stationary phase (see Fig. 3.24), 2-ethylexanoic acid peak (S) is absent in both the columns due to the type of the stationary phase used, whereas the diol peak (D) is absent only for the microcolumn. The reason is expected to be in a non-optimal deactivation process.

The separation in Fig. 3.25 represents a column efficiency of ~ 7950 plates/m. Although this is a lower performance than previously analyzed MEMS columns (which have achieved ~ 10000 plates/m), this result is encouraging and must be confirmed by other tests.
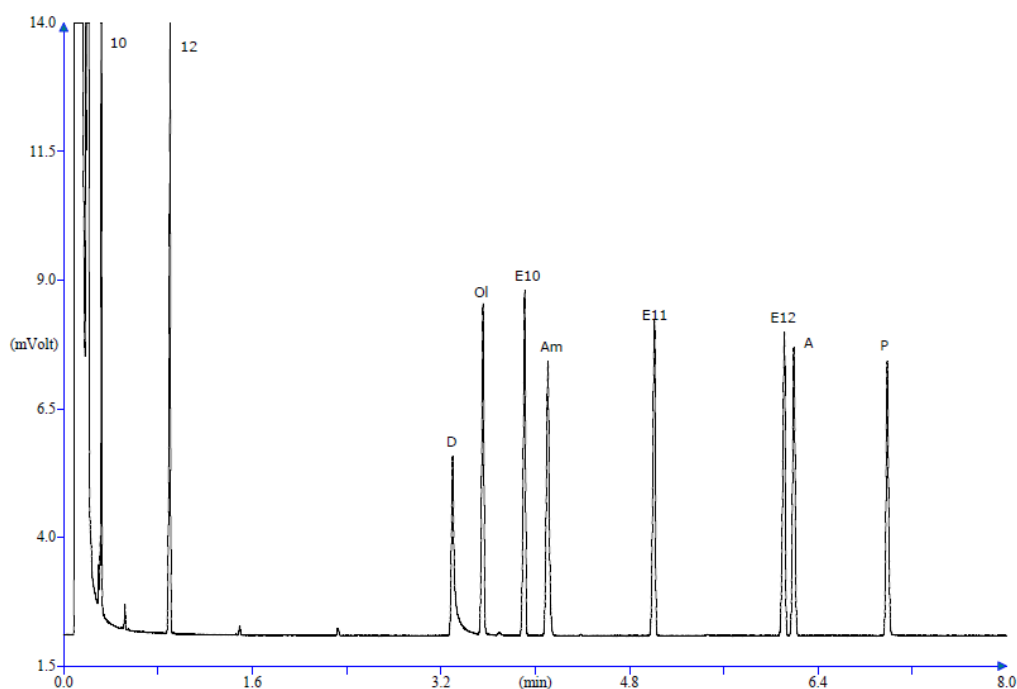
Fig. 3.25 - Chromatogram of Grob test mixture showing the performance of 5-m-long, 100-µm-ID commercially coated column coated by 0.10-µm-thick polar stationary phase.

REFERENCES

[1] Agah M. et al.; *J. Microelectromech, Syst.*, **15** (2006) 1371-1378.

[2] Reid V.R. and Synovec R.E.; *Talanta*, **76** (2008) 703-717.

[3] Grob R.L., Barry E.F.: "Modern practice of Gas Chromatography", *John Wiley & Sons, 4th edition* (2004).

[4] James A.T. and Martin A.J.P; *Biochem J.*, **52** (1952) 238.

[5] Giddings J.C.; Unified Separation Science, Wiley, New York, 1962.

[6] Giddings J.C.; *Anal. Chem.*, **36** (1964) 741.

[7] Giddings J.C.; *Anal. Chem.*, **35** (1963) 353.

[8] Cozzani E.; *Ph. D. Thesis, University of Bologna* (2011).

[9] Radadia A.D. et al.; *Anal. Chem.,* **81** (2009) 3471–3477.

[10] Radadia A.D. et al.; *Sensors and Actuators B*, **150** (2010) 456–464.

[11] Radadia A.D. et al.; *J. Micromech. Microeng.*, **20** (2010) 015002 (7pp).

[12] Licari J.J. and Swanson D.W.: "Adhesive technology for electronic applications", *Elsevier Inc. 2th edition* (2011).

[13] Lorenzelli L. et al.; *Biosensors and Bioelectronics*, **20** (2005) 1968–1976.

[14] Reidy S. et al.; Anal. Chem., **78** (2006) 2623-2630.

[15] Fuller E.N. et al.; *Ind. Eng. Chem.* **58** (1966) 18-27 (Equation 4).

4

MINIATURIZED INJECTION AND DETECTION SYSTEM FOR HIGH-SPEED GC

In the previous chapter we have focused on the separation column, the heart of a GC system. Here the development of a miniaturized injection and detection system for high-speed gas chromatography will be described. In particular, the design and fabrication of each microdevice will be presented together with the experimental results.

4.1 - MICRO-INJECTION SYSTEM

As reported in Chapter 2, the injection system has the function to inject the sample mixture into a separation column. To be employed in HSGC, the injector should deliver a very narrow vapor plug to the capillary column and guarantee low dead volumes, in order to avoid extra-column band broadening. These constraints must be strictly observed when an injection system for HSGC is to be microfabricated.

For the successful miniaturization of integrated microfluidic devices involving MEMS technology, it is desirable to have a reliable non-leaking microvalve that can be used in a wide temperature range and that is chemically inert.

Microvalves are a basic component of microfluidic systems since they permit fluid transfer, switching and control. MEMS technology has provided an opportunity for microvalves to be packaged onto a board with integrated fluidic channels to interconnect all the parts.

This section first describes the design and characterization of an innovative pneumatically driven microvalve based on a polymeric actuating membrane [1].

Then, the microinjection system will be presented together with the experimental results.

4.1.1 - SU-8 Photoresist: Composition, Chemical Reactions and Properties

The negative tone epoxy-based SU-8 photoresist has been chosen to fabricate the polymeric membrane because it is photopatternable, chemically resistant, mechanically reliable and, most important, chemically inert. In addition since it is also a biocompatible material it is often used in bio-MEMS applications.

The main component of the resist is EPON$^{®}$ SU-8 resin (Shell Chemical), which is dissolved in an organic solvent (γ-butyrolacton, GBL). The amount of solvent determines the viscosity and thus, the range of available thicknesses, extending from tens of nanometers to millimeters. The resin is made photosensitive by the addition of a triarylsulfonium salt (such as triarylsulfonium hexafluorantimonium), which acts as photo-acid generator.

The Fig. 4.1a shows the molecular structure of SU-8 (left: monomer; right: monomer unit in the crosslinked polymer) with eight epoxy sites per monomer. This demonstrates high epoxide functionality per molecule, which allows a high degree of crosslinking to be obtained to give high aspect-ratio and straight sidewall profiles after exposure.

Polymerization of SU-8 is based on chemical amplification. A single photoevent, known as protolysis, initiates a cascade of subsequent chemical reactions that induce the crosslinking process. In particular, when exposed to UV-light, the triarylsulfonium salt decomposes and generates a strong acid, the cationic photoinitiator (Fig. 4.1b), which initiates cationic polymerization by ring-opening and subsequent cross-linking of the epoxy groups (Figs. 4.1c and 4.1d).

The photoacid is not consumed in the initiation process and can function to initiate several chains. The crosslinking process ultimately yields a dense, stable network where each epoxy monomer is connected to seven others on average [2].
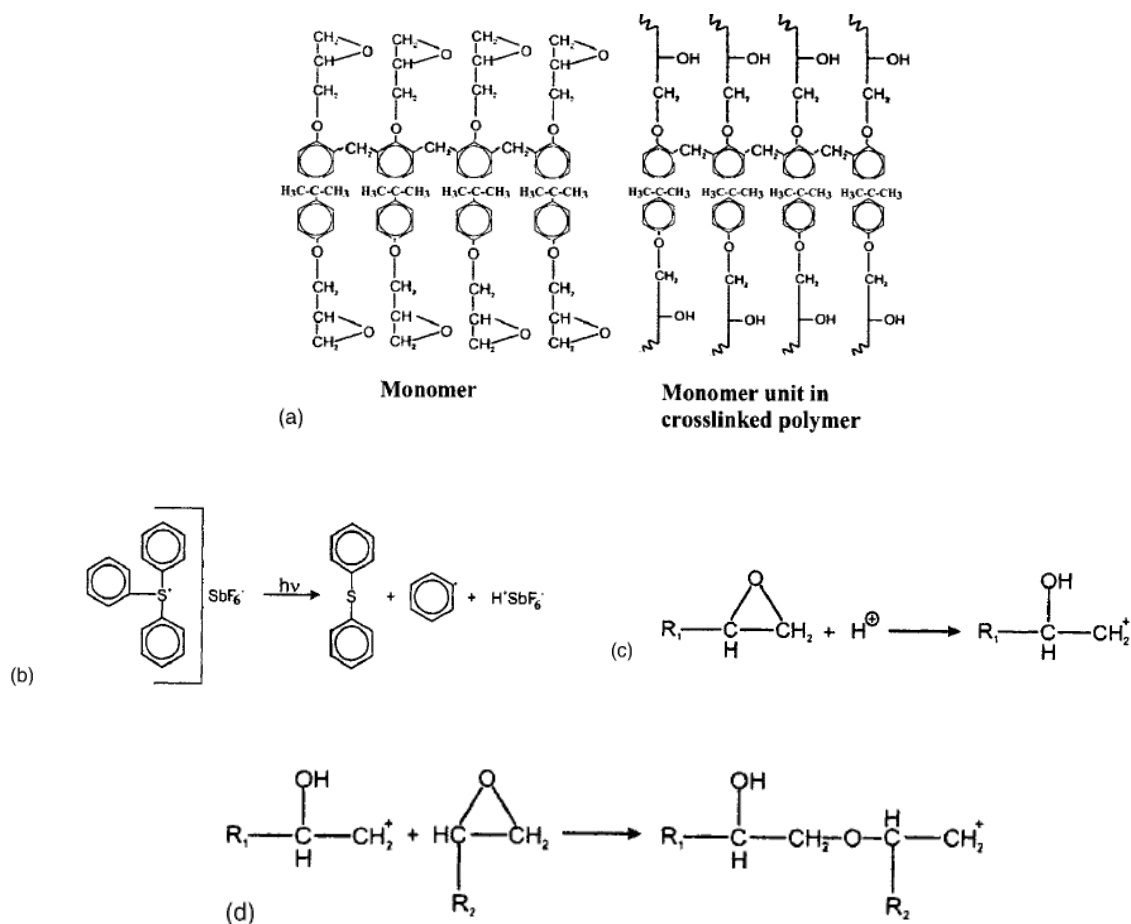
Fig. 4.1 - (a) Molecular structure of EPON SU-8: the monomer (left) and the monomer unit in the crosslinked polymer (right). (b) Generation of acid upon UV exposure as a result of protolysis of the cationic photoinitiator. (c) Initiation of polymerization (crosslinking) via opening of the epoxy group. (d) Chain propagation of the crosslinking process [2].

A typical SU-8 processing consists of four main steps: resist coating, exposure, curing, and development. The SU-8 is spin coated onto a substrate (Fig. 4.2A) and than soft backed for evaporating the solvent. In the exposure step the SU-8 film is subjected to near-UV light through a photolitographic mask (Fig. 4.2B). Once initiated in the exposure, the polymerization process is assisted by thermal energy (Fig. 4.2C) in the so-called post-exposure bake (PEB). Finally the unexposed SU-8 is dissolved by organic solvent (Fig. 4.2D), leaving the cross-linked SU-8 structures on the substrate [3]. In Fig. 4.3 a SEM image of some structures 10 µm-thick fabricated with SU-8 3010 (Microchem®) [4] is shown.
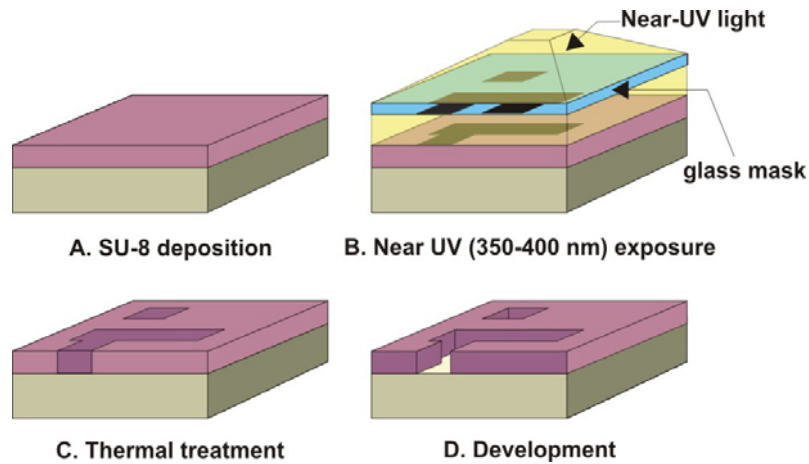
Fig. 4.2 - Typical SU-8 processing consisting of resist coating (A), exposure (B), curing (C) and development (D).
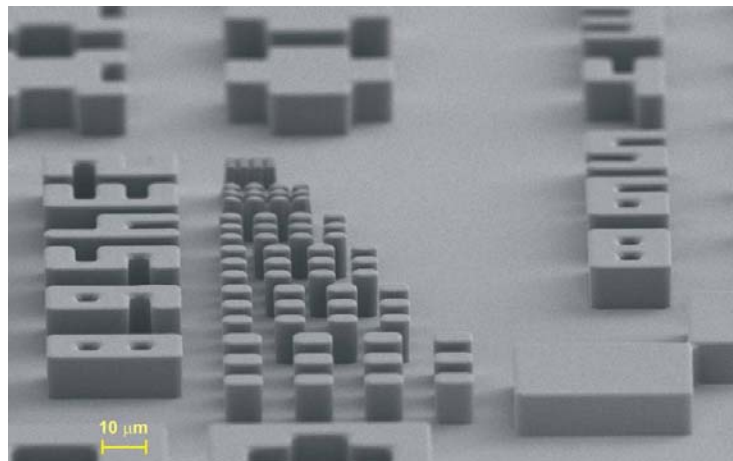
Fig. 4.3 - SEM image of SU-8 3010 10 µm thick structures.

In Tab. 4.1 some physical and mechanical properties of SU-8 3010 photoresist are listed [4].

SU-8 3010 Physical and Mechanical Properties	
Young's modulus (GPa)	2.0
Poisson's modulus	0.22
Tensile strength (MPa)	73
Thermal expansion coefficient (ppm/°C)	52

Tab. 4.1 – Physical and Mechanical properties of SU-8 3010 photoresist [4].

4.1.2 - A Normally Open Microvalve: Design and Characterization

The 2-ways normally open microvalve proposed consists of an SU-8 3010 10 µm thick membrane layer deposited between two micromachined silicon wafers. On the upper wafer, the actuation hole extending all through the silicon substrate is fabricated for enabling the deformation of the membrane. In the lower wafer, the fluidic circuit is manufactured.

A schematic cross-section view describing the operation of the microvalve is shown in Fig. 4.4: when no pressure is applied through the actuation hole, the membrane is flat above the gas path, and the gas flows from the inlet to the outlet of the microvalve (Fig. 4.4A). If sufficient pressure is applied, the membrane is deflected onto the ring, stopping the gas flow and closing the microvalve (Fig. 4.4B).
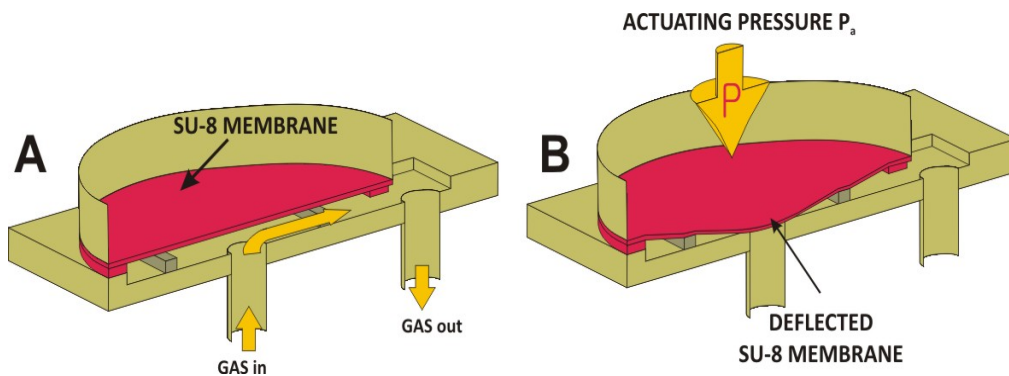
Fig. 4.4 – Actuation principle of the microvalves. (A) with no actuation pressure applied, the microvalve is open. (B) The deflection of the polymeric membrane due to a pressure applied closes the microvalve.

Preliminarily, a wafer containing test structures for the characterization of single membrane valves was fabricated. The main fluid path inside the test structures consist of (Fig. 4.5): a rectangular channel having a length of 8200 µm, a width (W_{ch}) ranging from 120 µm to 240 µm and a depth (t_c) of 30 µm; inlet and outlet pipes with circular sections of 80 µm diameter. All the membranes studied in this work have a thickness (t) of 10 µm and a constant ring radial (R_{ring}) width of 10 µm. The other main geometric parameters of the membranes are the membrane diameter (D) and the supporting ring inner diameter (D_i), and for each of these parameters two different values were studied, as reported below.
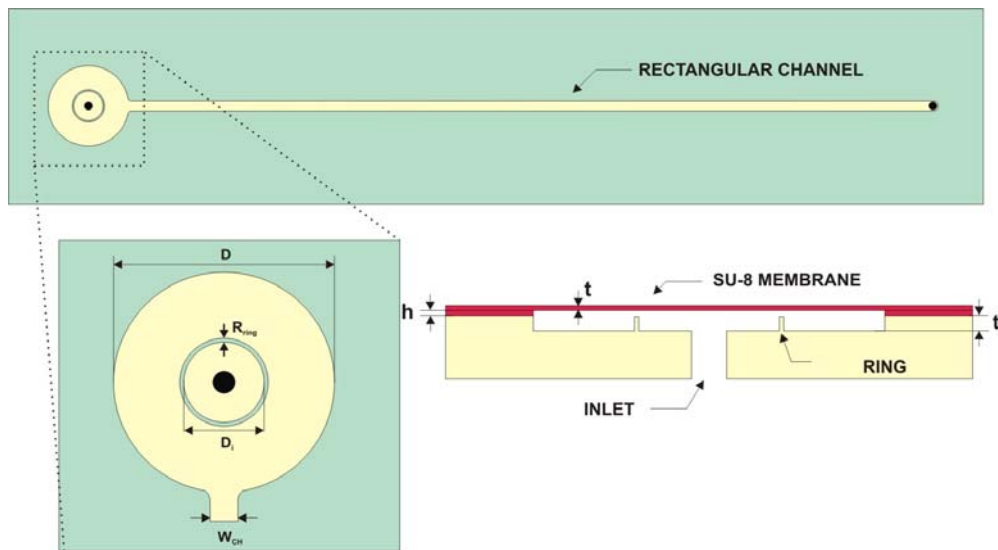
Fig. 4.5 - Microvalve main geometrical parameters and fluidic paths.

The purpose of the ring is twofold:

a) its height determines the microvalve discharge area (A_v):

$$A_v = \pi D_i h \tag{4.1}$$

which allows to control the maximum flow rate and where h is the thickness of the second layer of SU-8, with a constant value for all microvalves of 10 µm

b) its radius D_i allows to change the actuating pressure: by increasing the value D_i up to the membrane diameter (D), a higher actuating pressure is required to seal the carrier gas orifice.

The microvalve has been fabricated by assembling and bonding two different sub-systems (Fig. 4.6), which are separately fabricated: a) the upper part which consists of the SU-8 membrane and the hole for the microvalve actuation on a silicon wafer, (the actuation system); b) the lower part which consists of a second silicon wafer with the flow channels and the microvalve ring (the microfluidic system).

It should be stressed that all the fabrication process is performed at wafer level using standard MEMS technology: through-wafer holes and chamber are realized by DRIE and than the wafers have been assembled by an adhesive bonding at wafer level (see Chapter 1), using the same SU-8 photoresist layer as structural layer and adhesive layer.
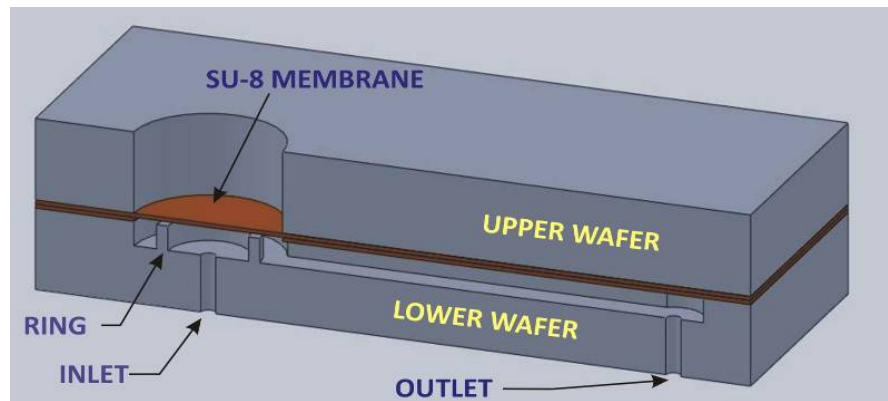
Fig. 4.6- Microvalve cross-section with SU-8 membrane.

In Fig. 4.7, a micrograph of the resulting microvalve can be seen.
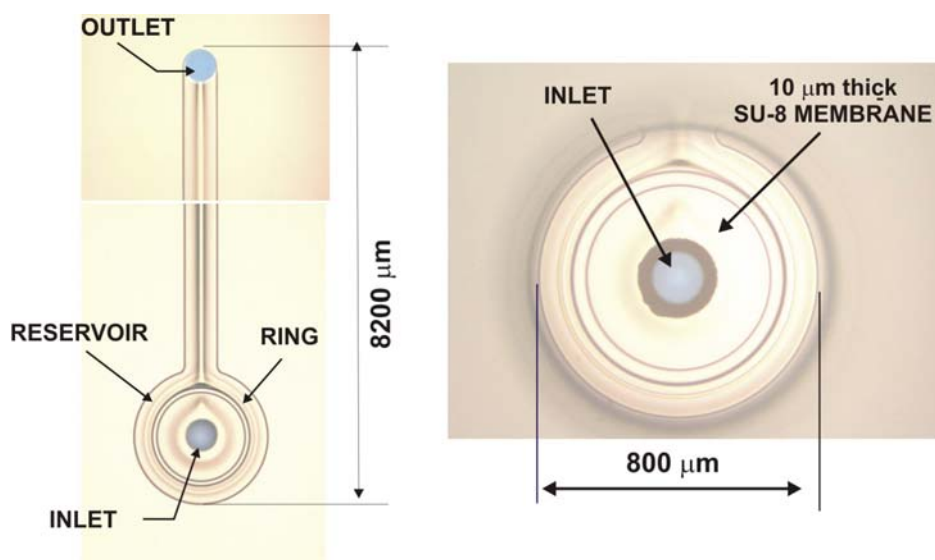
Fig. 4.7 – Optical micrograph of the microvalve with SU-8 membrane.

All the microvalves have been tested on a dedicated experimental setup, illustrated in Fig. 4.8. The experiments have been performed to determine the actuating pressure (P_a) required for sealing the microvalve, when the membrane is subjected to different carrier gas pressures (P_{in}) and to asses the durability of the microvalves under simulated heavy duty cycles (more than 400 000 cycles without any significantly change of the valve performance). To measure P_a the following procedure has been set up: a given pressure P_{in} has been set using nitrogen as carrier gas and then the actuating pressure P_a has been slowly increased until the carrier gas flow stopped.
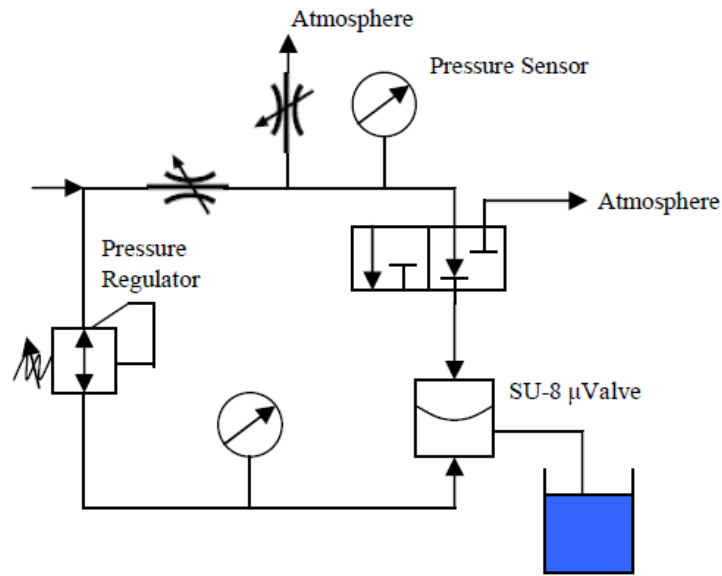
Fig. 4.8 - Schematic of the experimental setup [1].

The overpressure *ΔP* has been then evaluated as follows:

$$\Delta P = P_a - P_{in} \tag{4.2}$$

The carrier gas pressure P_{in} varies between 1.6, 2.0 and 2.5 bar in all the experiments. These values represent the typical carrier gas pressure that the microvalve has to counterbalance for closing the orifice. Tab. 4.2 shows the averaged values obtained during the measurements campaign. Considering microvalves with the same diameter *D*, it can be observed the marked decrease in actuating pressure required for sealing with the lower ring diameters [1].

	ΔP (bar)			
	D = 800 μm		**D = 500 μm**	
	D$_i$	**D$_i$**	**D$_i$**	**D$_i$**
P$_{IN}$ (bar)	200 (μm)	520 (μm)	150 (μm)	200 (μm)
1.6	0.38	1.32	0.70	1.30
2.0	0.35	1.24	0.62	1.03
2.5	0.32	1.32	0.56	1.03

Tab. 4.2 - Averaged measured microvalves actuating pressures [1].

4.1.3 - Micro-Injection System: Conceptual Layout and Experimental Results

The proposed injection system consists of a 12 x 12 mm^2 silicon chip integrating five pneumatically driven microvalves (based on a SU-8 actuating membrane reported above) and a 2 µL-volume sample loop (Fig. 4.9).

It should be stressed that, unlike previously reported micro-machined injectors [5], our chips are completely fabricated at wafer level by using standard MEMS technology with 8 photolithographic masks: in particular, the devices are produced by bonding three different 300 µm-thick silicon wafers exploiting two 10 µm-thick SU-8 layers as bonding adhesive (see Chapter 1). The simplified structural schematic is depicted in Fig. 4.9.
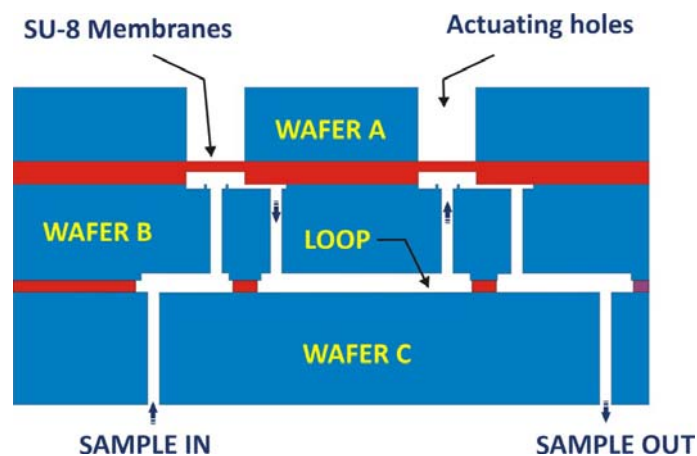
Fig. 4.9 - Structural schematic of the microinjector.

The basic operation of the microinjector proposed is sketched in Fig. 4.10. The pneumatic actuation of the polymeric membranes is controlled by switching five commercial electrovalves (response time ~ 1 ms) through a properly designed control electronics with the support of a dedicated software.

1. First step (*sampling*): VALVE 1 and VALVE 2 are closed and carrier gas flows into the reference and analytical GC column via VALVE 5, while the sample reaches the loop via VALVE 3 and VALVE 4.

2. Second step (*loop pressurization*): VALVE 1, VALVE 2 and VALVE 3 are closed, while VALVE 4 and VALVE 5 are open. Loop is pressurized with carrier gas via VALVE 4 and so the sample is blocked in the loop.

3. Third step (*injection*): VALVE 1 and VALVE 2 are opened, while VALVE 3, VALVE 4 and VALVE 5 are closed. Carrier gas reaches the loop via VALVE 1 and carries the sample to the separation column via VALVE 2.
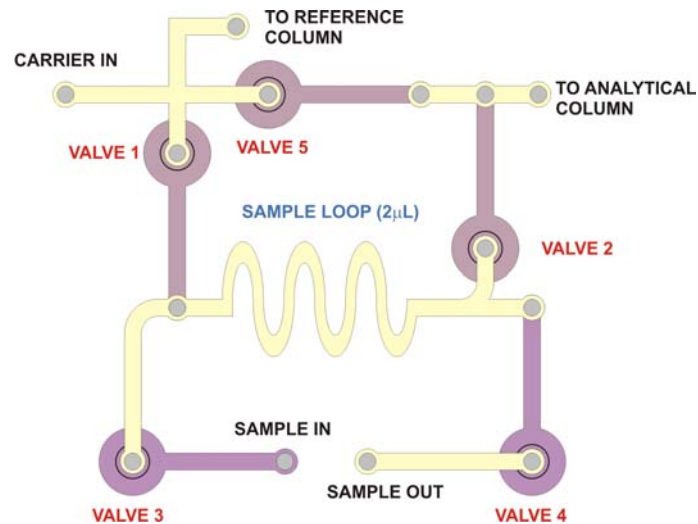
Fig. 4.10 - Functional schematic of the microinjector.

In the Fig. 4.11, an injector mask layout is depicted together with an image of the microdevice. Triple wafers (each 300 μm - thick) bonding process with SU-8 multi-layers has been set-up for device fabrication.
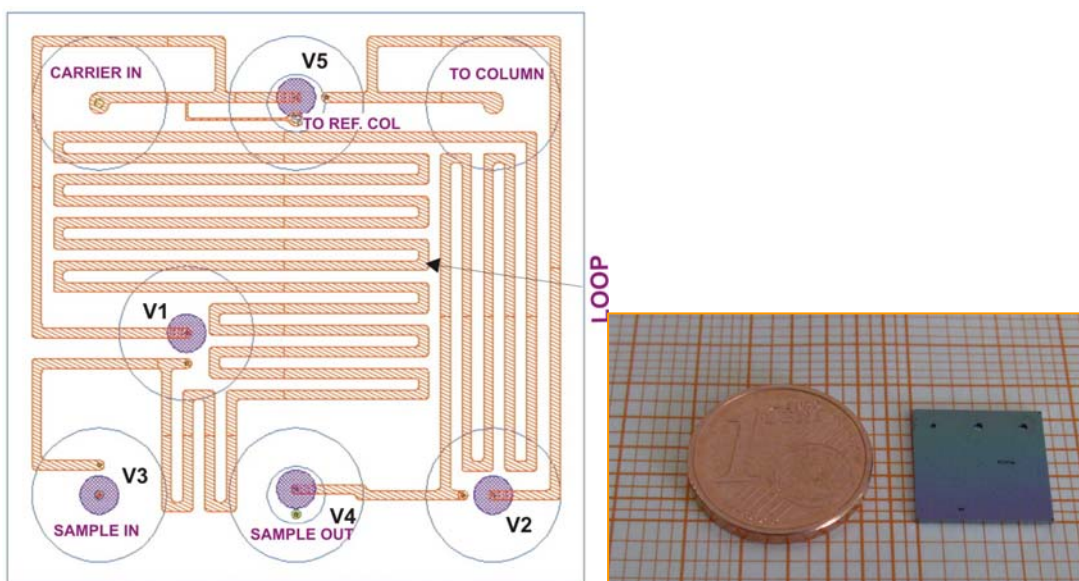
Fig. 4.11 - Microinjector mask layout (left); photograph of the fabricated injector die of overall size 12 mm x 12 mm x 0.9 mm, placed near a cent coin (right).

In order to evaluate the performances of the device, the microinjector has been housed in an appropriate manifold and connected via 1/16" PEEK tubes (ID = 500 μm) and fused silica capillaries (ID = 100 μm) to the sample bag, the sampling pump, and the carrier gas (helium) line.

In addition, the device has been connected to a commercial Thermo Scientific FOCUS-GC, equipped with standard capillary column (3.2-m-long, 75-μm-ID; MEGA-1μm film thickness) and a Flame Ionization Detector (FID).

The functional characterization of the device has been performed in three steps by injecting a natural gas sample consisting of a certified mixture of compounds (whose concentrations are listed in Tab. 4.3).

Peak #	Compound	Concentration
1	Methane	95.22%
2	Ethane	3.40%
3	Propane	0.85%
4	*i*-Butane	0.14%
5	*n*-Butane	0.20%
6	*i*-Pentane	0.05%
7	*n*-Pentane	0.05%
8	Hexane	0.09%

Tab. 4.3 - Natural gas sample and concentration of the compounds.

In the first experiment, the repeatability of the injecting mechanism has been tested, by performing 30 consecutive measurements of natural gas sample; the graph reported in Fig. 4.12 shows that the area of the methane peaks (considered as reference) remains basically constant (standard deviation = 0.2%).

In the second test, the linearity of the injecting mechanism has been investigated: the graph reported in Fig. 4.13 shows the area of the propane peak as a function of the injection time and the linear behavior of the device in the [400 ms ÷ 3 s] range can be easily disclosed.
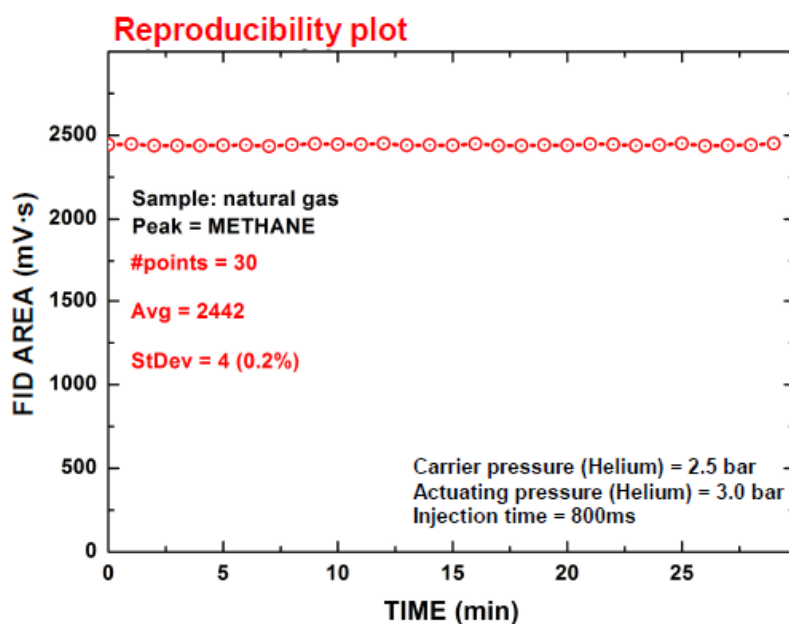
Fig. 4.12 - Area of methane peaks due to 30 consecutive
injections of sample natural gas.

In the last experiment, complete chromatograms of the natural gas sample have been performed. Natural gas analysis is challenging due to the very different concentrations of the single compounds (methane >98%, pentane 0.05%) and to the very similar retention times of methane and ethane, which are very demanding on the entire analysis system.
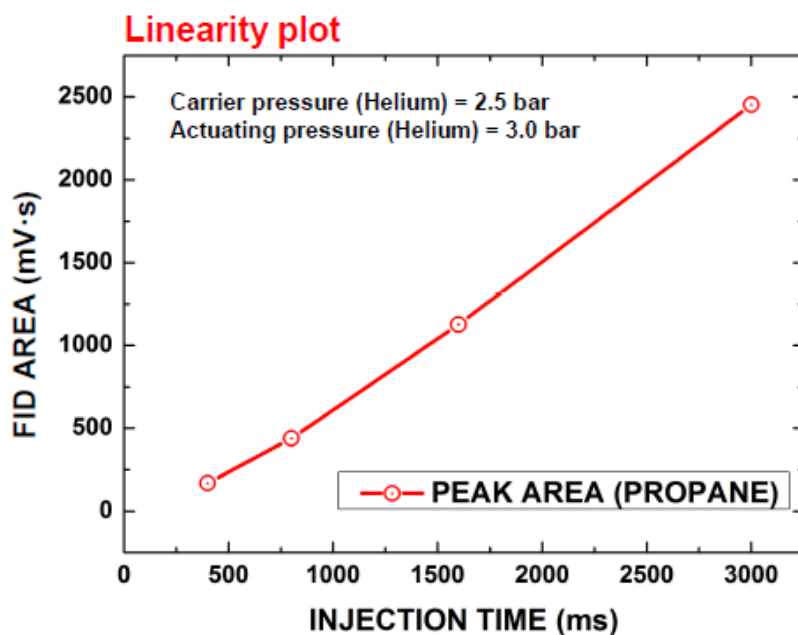
Fig. 4.13 - Area of propane peaks as a function of the injection time.

A typical result is reported in Fig. 4.14 (the correspondence between peak number and single compound is the same reported in Tab. 4.3): the excellent separation between the peaks and their perfectly Gaussian shape are an index of the good working operation of the injector chip.
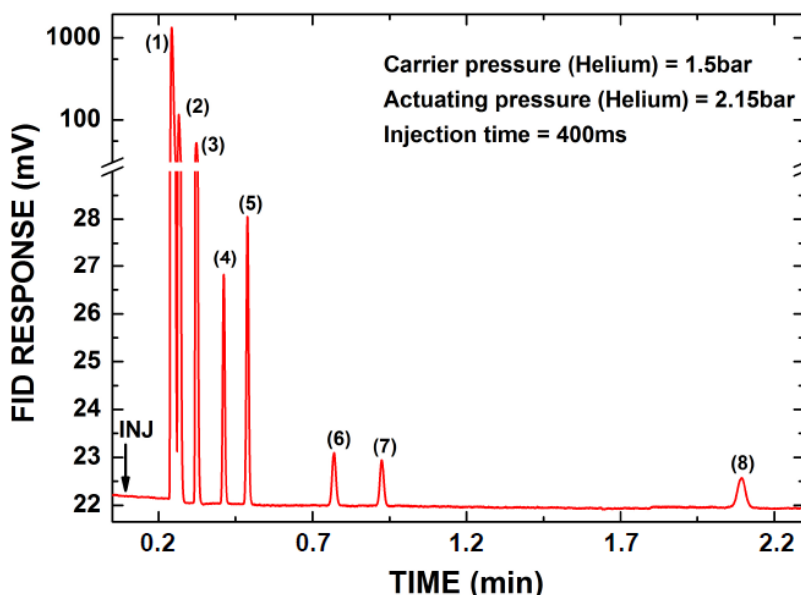
Fig. 4.14 - Chromatogram of a natural gas mixture (components are listed in Tab. 4.3) performed with a standard capillary column (3.2-m-long, 75-µm-ID; MEGA-1µm film thickness).

By a series of several experiments, we have noticed that the microinjector is able to ensure reduced dead volumes, fast injection times and repeatable results.

Finally, a further characterization has been performed aimed at investigating the chemical inertness of the polymeric membrane. This property has been tested by continuously exposing the polymeric membranes to injection of three different type of potentially corrosive solvent, such as trichloroethylene, toluene and isopropyl alcohol. These tests have showed that, despite the harsh working conditions the chip has been submitted to, the injecting performances of the microdevices remained unchanged.

4.2 - MICRO-DETECTION SYSTEM

The third main component of a gas chromatograph is the detector i.e. the sensitive element that, interacting with the analytes of the sample mixture eluting from the separation column, reveals and quantifies their individual amount. In literature, a great variety of detection systems for GC is proposed, e.g. thermal conductivity detector (TCD), flame ionization detector (FID), photo ionization detector (PID), electron capture detector (ECD), mass spectrometer (MS), and one must select the appropriate typology for the particular application.

As already mentioned in the Introduction, since the aim of this research activity is the development of a completely microfabricated HSGC-system, constraints related to small sizes and low power consumption must be taken into account, to fulfill the requirement of extremely low dead volumes.

Unlike ionization sensors that are mass sensitive (i.e. flame ionization detectors, FIDs), thermal conductivity detectors (TCDs) are non-destructive, concentration based sensors. Thus, their integration with micromachining techniques is very common and miniaturization does not worsen their performances. In fact, while mass decreases, concentrations remain unaffected [6].

4.2.1 - TCD Working Principle

Thermal conductivity detector (TCD) is a well known sensor for flow measurement and gas analysis. It is identified as a physical detector, since it responds to a difference in the thermal conductivity (a physical property) of a carrier gas caused by the presence of the eluted components.

The most common example of TCD is represented by a wire filament heated by the electrical current flowing through it. Using a wire with a temperature (T) dependent resistance (R), the temperature of the wire can be measured according to the well known relation:

$$R(T) = R_0 \cdot (1 + \alpha \cdot T) \tag{4.3}$$

being α the temperature coefficient of resistance for the wire filament and R_0 the resistance at the reference temperature of 0 °C.

If the filament is surrounded by a reference gas, small changes in gas thermal conductivity due to the presence of the analytes (different from the reference gas) cause variations in temperature T, that can be detected by the change in wire filament resistance.

The TCD is commonly operated using helium or hydrogen as the carrier gas, since their thermal conductivity (respectively 0.142 W/m·K and 0.160 W/m·K at 298 K) is higher than that of all the typical eluted components.

The TCD working principle is clearly suitable for implementing a differential measurement scheme: the presence of the analyte, in fact, can be better revealed by comparing the thermal conductivity of the pure carrier gas with the thermal conductivity of the gas mixture represented by the carrier gas in addition with the analyte.
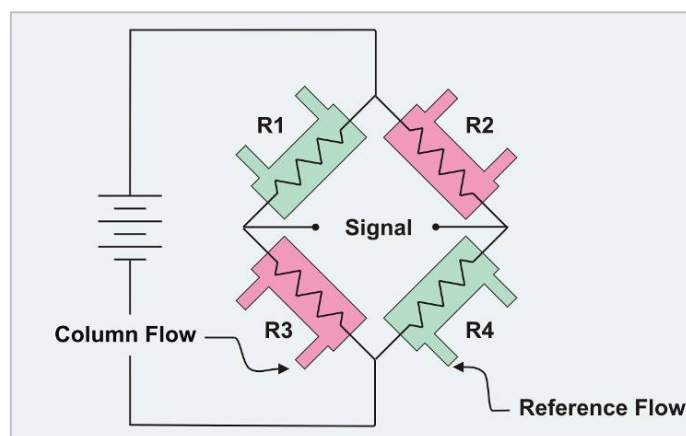
Fig. 4.15 - Wheatstone bridge configuration.

A typical arrangement for a TCD is represented by four filaments put within a Wheatstone bridge configuration, as illustrated in the Fig. 4.15.

The pure carrier gas (reference) flow enters resistor R_4, while the flow from analytical column (carrier gas + eluted sample components) enters resistor R_3. The four resistors are designed such that, in absence of sample eluted from the column, the Wheatstone bridge results balanced, that is:

$$R_1 \cdot R_4 = R_2 \cdot R_3 \tag{4.4}$$

and, as a consequence, $V_B = 0V$.

As a substance elutes from the column and enters R_3 (together with the carrier gas), thermal conductivity of the analytical flow differs from thermal conductivity of the carrier gas that enters R_4; for this reason, temperature of R_3 differs from temperature of R_4 and, from eq. 3, $R_3 \neq R_4$.

Hence, Eq. (4.4) is not verified and, as a consequence, a nonzero voltage measurement is obtained ($V_B \neq 0V$), revealing the presence of the sample substance [6]. In the most common TCD implementations, both resistors R_2 and R_3 are subject to the column flow, and both resistors R_1 and R_4 to the reference flow, further improving the signal of the Wheatstone bridge.

4.2.2 - Design and Characterization

Figure 4.16 shows mask layout (with geometrical dimensions) and an optical micrograph of the designed configurations for the single resistors forming the Wheatstone bridge.
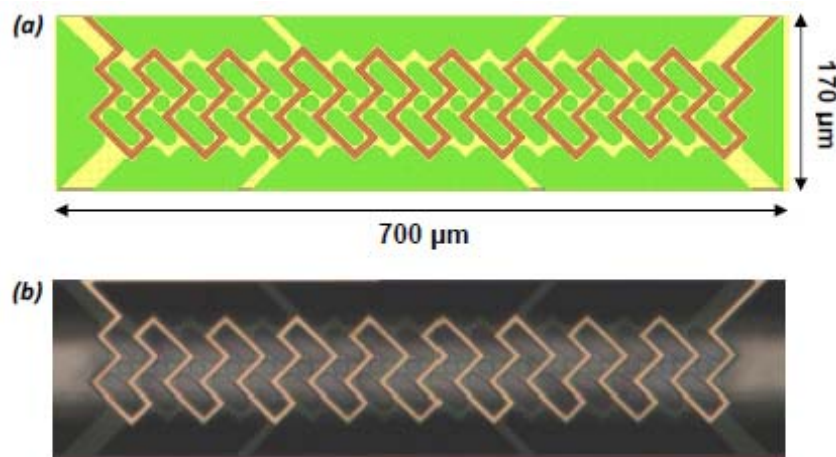
Fig. 4.16 - Example of mask layout (a) and optical micrograph (b) for the single resistor of the Wheatstone bridge [6].

The microfabricated TCD has been obtained using conventional silicon micromachining techniques.

The resistors are made of a thin film of platinum. In order to improve the thermal insulation between the heaters and the highly thermally conductive silicon substrate, the resistors are fabricated on an insulating suspended membrane obtained by bulk

micromachining technique. The silicon substrate underneath the membrane has been removed by a TMAH solution.

The silicon chip (dimensions 5 mm x 5 mm) containing the suspended structures is encapsulated, through an anodic bonding technique, with a mechanically micro-machined Pyrex® wafer implementing ultralow-volume microchambers (the reference channel and the analytical channel, both with square cross-section of 250 x 250 μm^2 (Fig. 4.17) [6].
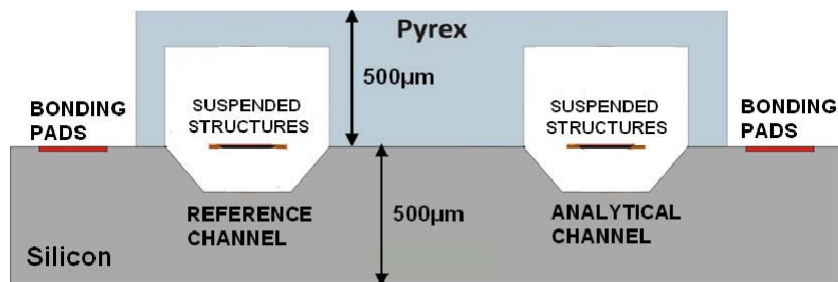
Fig. 4.17 - Cross-section of the TCD encapsulated with the Pyrex® microchambers [6].

In Fig. 4.18, a picture of the micromachined TCD is shown together with an enlarged image of the microdevice.
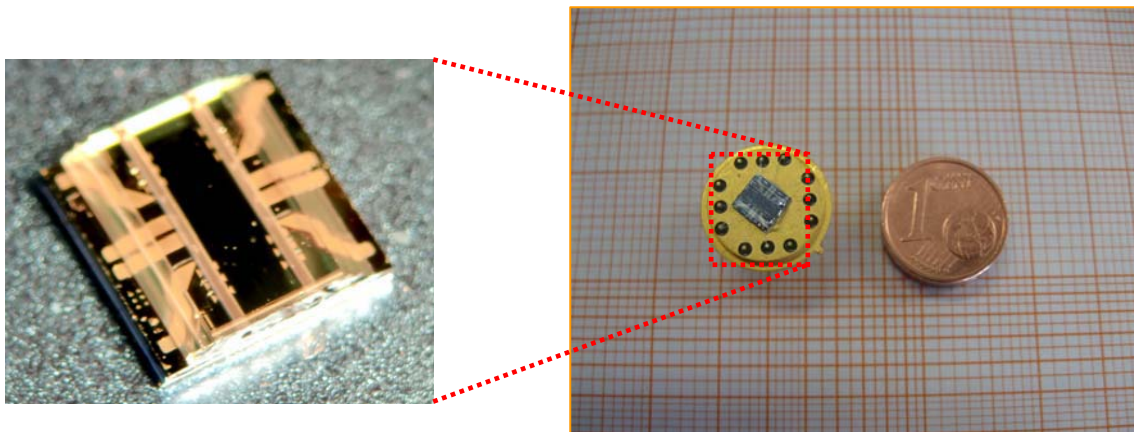
Fig. 4.18 - Pictures of the micromachined TCD bonded over a TO8 case compared with 1 cent coin (right) and an enlargement of the microdevice with its Pyrex® cover (left).

To preliminarily investigate the sensitivity of microfabricated TCD with respect to changes in gas carrier composition, an experimental set up has been prepared in order to characterize the device (Fig. 4.19) when two different carrier gases (nitrogen and helium) are injected into the miniaturized chamber.
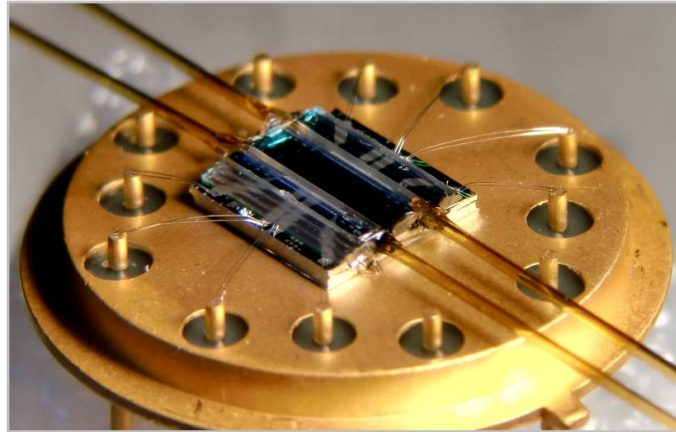
Fig. 4.19 - Pictures of the micromachined TCD (bonded over a TO8 case)
with fused silica capillaries inserted both in analytical and reference branches [6].

The experimental setup is shown in Fig. 4.20: one of the capillaries (fused silica tubes with ID = 100 μm) is the carrier gas inlet of the TCD, and it is connected on one side to the TCD and on the other side to a pressure sensor, which is used to measure the local absolute pressure before the carrier gas enters the capillary. Upstream of the pressure sensor, a relief valve is used to regulate the gas flow coming from helium (or nitrogen) piping system.
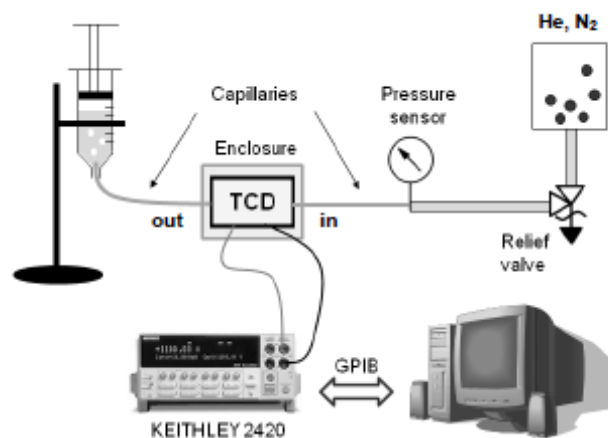
Fig. 4.20 - Experimental set-up used for TCD electrical characterization [6].

The other capillary is the carrier gas outlet, which can be inserted into the orifice of a vertically suspended syringe (filled with de-ionized water) for volumetric flow measurements.

The small capillary diameter, blocking the ingestion of water into the capillary, acts as a one-way valve, so that the gas flowing into the syringe determines, with the plunger blocked, the release of water, giving a visual measurement which can be converted in Standard Cubic Centimeters per Minute (sccm).

A constant gas carrier volumetric flow rate of 0.5 sccm (typical of HSGC) has been provided for both helium and nitrogen, and Heater resistance vs. Power curves are depicted in the following graph:
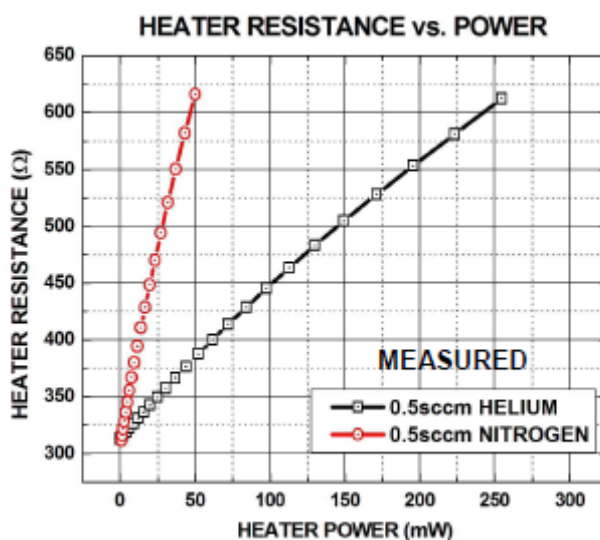
Fig. 4.21 - Measured Temperature vs. Power curves at 0.5 sccm flow rates: nitrogen (red line) and helium (black line) [6].

As can be easily disclosed from the trends in fig. 4.21, the temperature of the TCD filament, as indicated by its resistance in accordance to equation 4.3, at a given heater power dissipation is much higher in the case of nitrogen flow, due to the lower thermal conductivity of nitrogen compared to helium.

4.2.3 - Experimental Results

The miniaturized TCD has been first connected to the outlet of a commercial Varian GC/TCD system for preliminary comparative tests. The system includes a sample loop of 2 µL and a 8-meter long and 150-µm-ID standard fused silica capillary column coated with a DMPS stationary phase. The chromatogram has been acquired in isothermal mode at 60 °C. Helium has been used as carrier gas at a constant pressure of 200 kPa and a flow rate of 1.5 mL/min for the detection of a toluene

headspace sample at room temperature. The analytical branch and reference branch of the miniaturized TCD have been connected downstream of the commercial Varian GC/TCD. This results in the slight peak broadening and longer retention times of microfabricated TCD due to the interconnections dead volumes. Nevertheless the peak area and the baseline noise are comparable for both detectors (Fig. 4.22) [7].
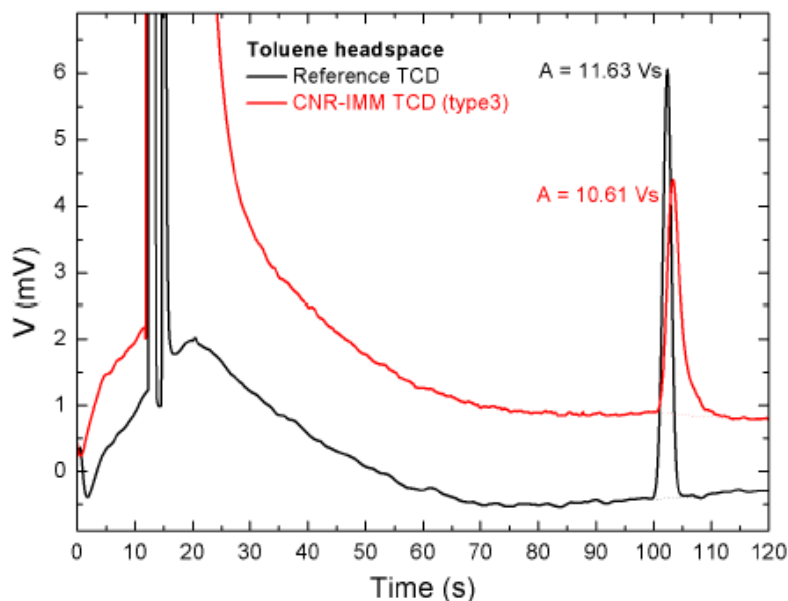
Fig. 4.22 - Comparison between chromatograms of toluene in He acquired with a commercial Varian GC/TCD and with the micromachined TCD [7].

In a second experiment, the analytical branch of the microfabricated TCD has been connected to the outlet of another commercial GC system, i.e. a Thermo Scientific Focus GC, equipped with a 5 m-long, 50-µm-ID standard fused silica capillary column coated with a DMPS stationary phase. The column has been operated at a constant helium carrier pressure of 400 kPa. An empty fused silica capillary (1-m-long; 50-µm-ID) has been used as reference branch and it has been operated at constant helium carrier pressure of 135 kPa. In these conditions, the flow inside both columns is estimated to be the same, nominally 0.086 mL/min. The columns have been installed inside the same GC oven, which has been operated in isothermal mode at 60 °C. The microfabricated TCD temperature set-point has been 300 °C. Liquid toluene has been injected at very high split ratios between 1:1500 and 1:4500, resulting in masses below one microgram. As can be disclosed from the Fig. 4.23, the signal shape is very well defined over the baseline with these amounts of toluene,

and the detection limit is expected to be much lower and will be determined once the final specifications for the GC column geometry and for the microfluidic section will be defined. Since the response of a TCD a function of the analyte concentration, the good response to masses in the range of nanograms is due to the extremely low volume of the sensing chamber of the proposed microfabricated TCD, as enabled by MEMS technology [8].
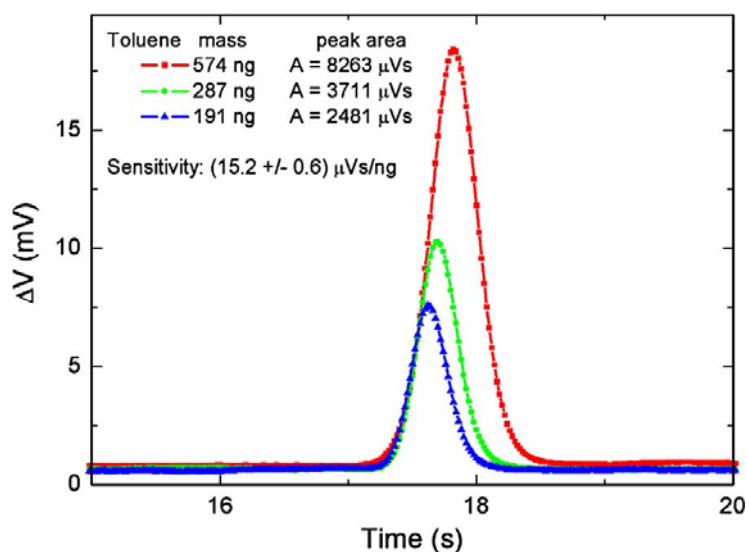
Fig. 4.23 - Sensitivity tests on several toluene masses. The vertical scale shows the Wheatstone bridge imbalance [8].

The 191 ng of toluene ideally eluted into the 0.3 µL microchamber result in an equivalent concentration as high as $6.37*10^5$ µg/L. The peak area is also reported in the plot. Several tests on masses of toluene revealed the good sensitivity of 15.2±0.6 µVs/ng: it makes the microfabricated TCD suitable for many portable applications like in-line quality control, industrial security and safety [8].

In a third experiment the miniaturized TCD has been connected downstream of the 3.2-meter long and 75 µm-ID conventional capillary column coated with 1 µm of DMPS stationary phase. An empty fused silica capillary column (1.5- m-long; 50-µm-ID) has been used as reference branch. The columns have been installed inside the same GC oven, which has been operated in isothermal mode at 35 °C. Helium has been used as carrier gas at constant pressure of 125 kPa and at a flow rate of 0.14 mL/min.

A volume of 1 microliter of natural gas mixture has been injected using a gas-tight syringe and the split injector at very high split ratio of 1:1820, resulting in 0.55 µL in column. The data associated with revealed compounds are shown in Tab. 4.4 where the thermal conductivity (TC) in helium of each analyte is also reported. Helium TC is equal to 142.6 mW/m·K [8].

Peak #	Compound	TC (mW/m·K)	Nominal Concentration (%)*	Peak Area (mV·s)	Measured Concentration (%)
1	Methane	32.8	95.22	105.9	95.20
2	Ethane	18.1	3.40	4.98	3.32
3	Propane	15.2	0.85	1.44	0.88
4	*i*-Butane	13.6	0.14	0.261	0.15
5	*n*-Butane	13.6	0.20	0.378	0.22

Tab. 4.4 - Name and concentration of the compounds in a natural gas mixture.

(*) reference concentration as certified by the cylinder calibrated

natural gas supplier: SIAD Gas Speciali, Osio Sopra (Italy) [8].
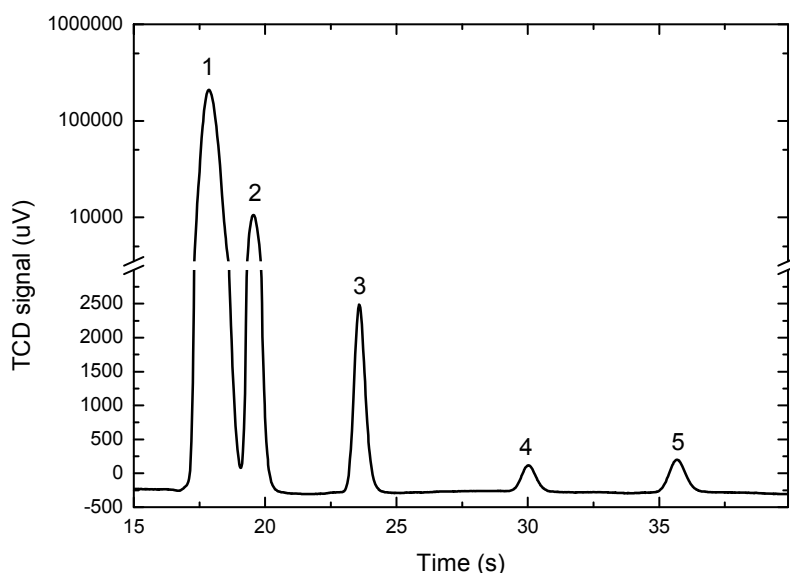
Fig. 4.24- Separation of a five-components natural gas

mixture. Peaks name are listed in Tab. 4.4.

As can be disclosed from the Fig. 4.24, where all the peaks of the 5 compounds are clearly acquired despite their very different concentrations, the microdevice shows a good sensitivity and a very wide dynamic range.

4.3 - MICRO-INJECTOR AND MICRO-DETECTOR ASSEMBLY

In all the tests reported up to now, the micromachined devices i.e. injector, separation column and detector have been tested individually, replacing from time to time the three functional blocks of a conventional gas chromatograph.
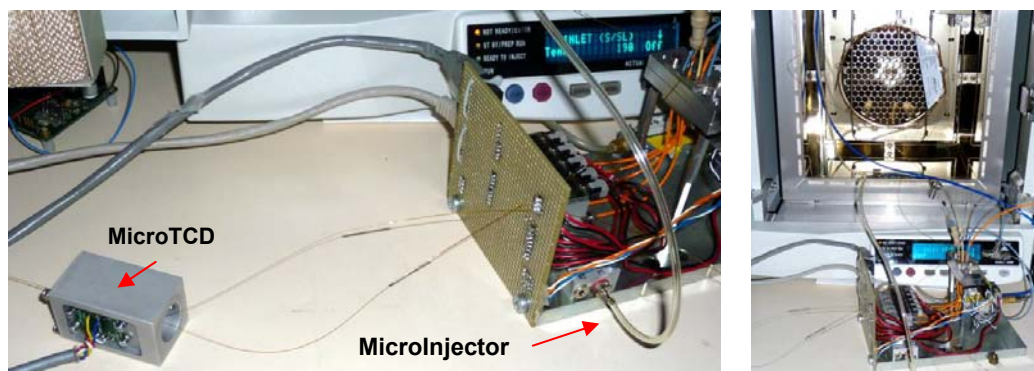
Fig. 4.25 - Micro-Injector and Micro-TCD assembly. MicroInjector and MicoTCD have been housed in appropriated manifolds (left) and connected to a fused silica capillary column placed in a Thermo Scientific® FOCUS/GC oven (right).

Since our goal is to assemble the three microdevices in order to obtain a micro-GC system, the first step has been to connect the micromachined injector and TCD to a conventional fused silica capillary column for HSGC (3.2-m-long; 75-µm-ID) coated with 1 µm of DMPS stationary phase (Fig. 4.25).

An empty fused silica capillary column (1.5-m-long; 50-µm-ID) has been used as reference branch. Both columns have been fed by injector chip and the temperature of both columns was left floating at room temperature. Helium has been used as carrier gas and the injector temperature has been 30 °C. The chromatographic conditions are listed in Tab. 4.5.

Carrier gas pressure (P_{IN})	200 kPa
Actuating pressure (P_{act})	277 kPa
Pressurization time	800 ms
TCD temperature	300 °C

Tab. 4.5 - Chromatographic conditions for the analysis of natural gas mixture.

In a first experiment (Fig. 4.26A) an eight-components natural gas mixture has been introduced at two different injection times: 600 ms and 800 ms.

Since methane and ethane peaks are overlapped, in a second experiment, the injection time has been shortened (Fig. 4.26B) and the separation between methane and ethane peaks is more evident.
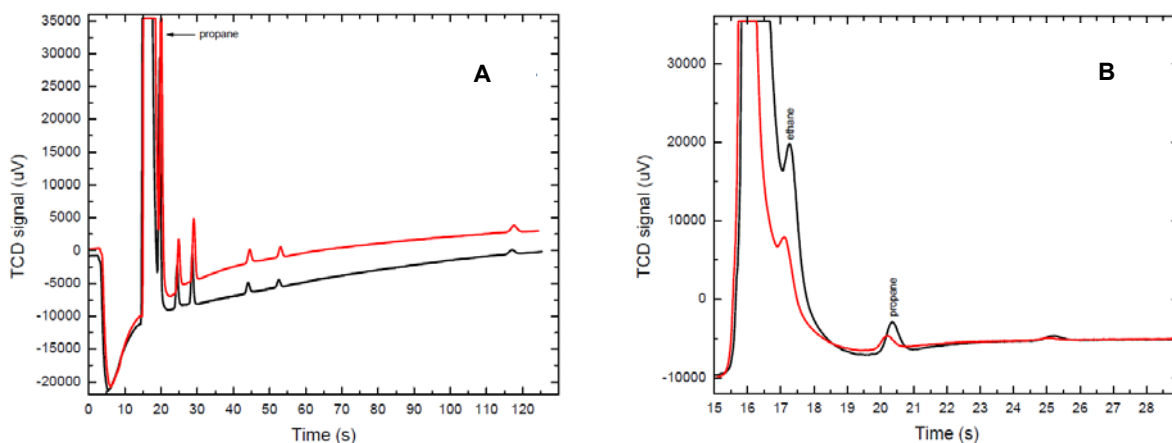
Fig. 4.26 - Natural gas mixture chromatogram at different injection times:
A. 600 ms (black); 800 ms (red), in order from left to right: methane; ethane;
propane; i-butane; n-butane; i-pentane; n-pentane; n-hexane;
B. 50 ms (black); 20 ms (red).

In the last experiment (Fig. 4.27) TCD temperature has been decreased in order to reach a better stability of the detector base-line.
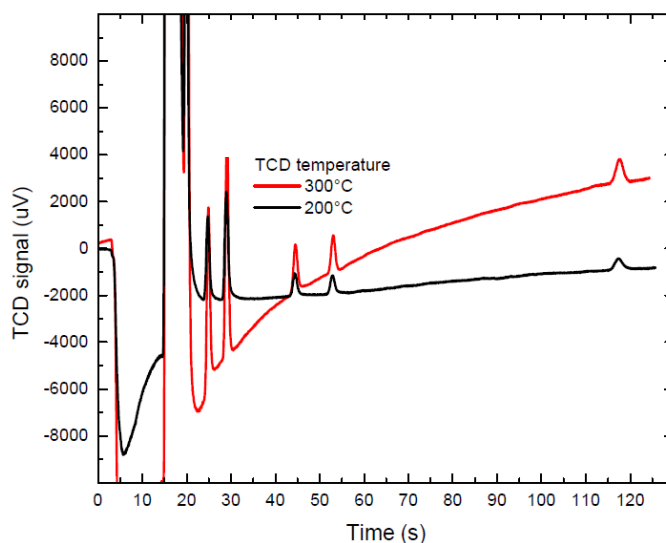
Fig. 4.27 - Effect of lower TCD temperature on baseline stability and response.
The chromatographic conditions are listed in Tab. 4.4.

Concerning the assembly of the complete prototype integrating all three of the micromachined components, the integration work is currently ongoing. A photograph of the prototypal miniaturized HSGC system is shown in Fig. 4.28. Unfortunately, no experimental results can be reported at this stage.
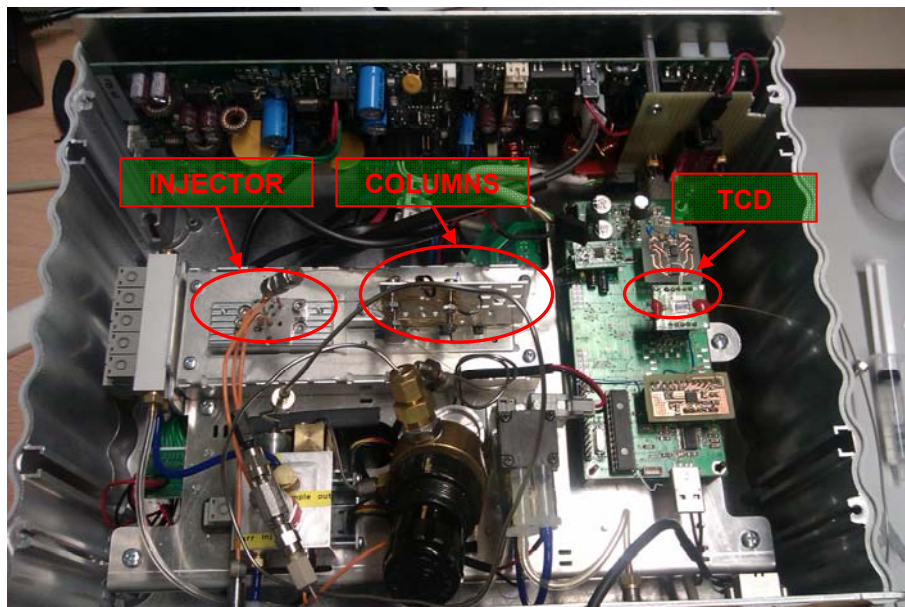
Fig. 4.28 - Micro-GC system assembling. The overall dimension, including all the accessories and the control electronic, is 35 x 15 x 25 cm^3.

REFERENCES

[1] Nubile A., et al.; *Technical Proceedings of the 2012 NSTI Nanotechnology Conference and Expo, NSTI-Nanotech* (2012) 172-175.

[2] Teh W.H. et al.; *Journal of Applied Physics,* **97** (2005) 054907.

[3] Anhoj T.A.; *Ph. D. Thesis*, Technical University of Denmark (2007).

[4] http://www.microchem.com/

[5] Dziuban J.A. et al.; *Sensors and Actuators A*, **115** (2004) 318-330

[6] Cozzani E.; *Ph. D. Thesis*, University of Bologna (2011).

[7] Rastrello F. et al.; *2012 IEEE I2MTC - International Instrumentation and Measurement Technology Conference, Proceedings*, (art. no. 6229304) 1226-1230.

[8] Rastrello F. et al.; *IEEE Transaction on Instrumentation and Measurement*, Article in Press (DOI 10.1109/TIM.2012.2236723).

5

MINIATURIZED GRAVITATIONAL FIELD-FLOW FRACTIONATION CHANNEL

In this chapter, after a brief overview on the field-flow fractionation (FFF) technique, including general principles and operation modes, the design and fabrication of a micromachined channel for gravitational field-flow fractionation (micro-GrFFF) will be presented. In addition, the preliminary experimental results obtained with micro-GrFFF will be discussed and compared with those obtained with traditional GrFFF devices.

5.1 – INTRODUCTION

The last decade has seen an exponential growth in the development of micro-total-analysis-system (μTAS) or lab-on-a-chip (LOC) devices for creating better, faster, and cheaper chemical and biological analysis platforms [1]. In addition, the "Point-Of-Care-Testing" (POCT) devices have the aim of performing clinical chemistry analysis directly where the sample is obtained in order to resolve, for example, the time lag between test results and patient care. For meeting diagnostic and analytical requirements, a POCT device should combine portability and minimum sample pre-treatment as well as the possibility to perform simultaneous detection of several biomarkers (multiplexing) in a short assay time and with small sample volumes. Depending on the analysis type, sample pre-treatment (i.e. pre-analytical sample preparation and clean-up) is often the most critical point. For example in many bioassays conducted on complex biological samples (such as blood, urine, or saliva), sample pre-treatment is important to achieve the needed specificity and detectability. In this regard the "soft" separation mechanism of field-flow fractionation (FFF) makes this separative technique particularly suitable to analyze biological samples (from

relatively small biomolecules to living cells), with maintenance of their native characteristics such as cell integrity and viability or enzymatic activity. FFF is a family of separative techniques with specific ranges of application to dispersed analytes.

The gravitational FFF (GrFFF) variant, exploiting the Earth-gravity field to structure the separation, appears to be particularly suited for its implementation in POCT systems thanks to the simplicity of its separation device, amenability to miniaturization, and the potential easy on-line integration with specific analytical modules [2]. In this regard, a silicon/Pyrex® micromachined GrFFF channel will be presented together with the experimental results.

5.2 - FIELD-FLOW FRACTIONATION: AN OVERVIEW

In the field of analytic separations, Field-Flow Fractionation (FFF) occupies a unique niche because of its capability to separate analytes in a 10^{15} molar mass range, from macromolecules to micron-sized particles. The name "*field-flow fractionation"* was coined in the first publication on FFF by J. C. Giddings in 1996 [3].
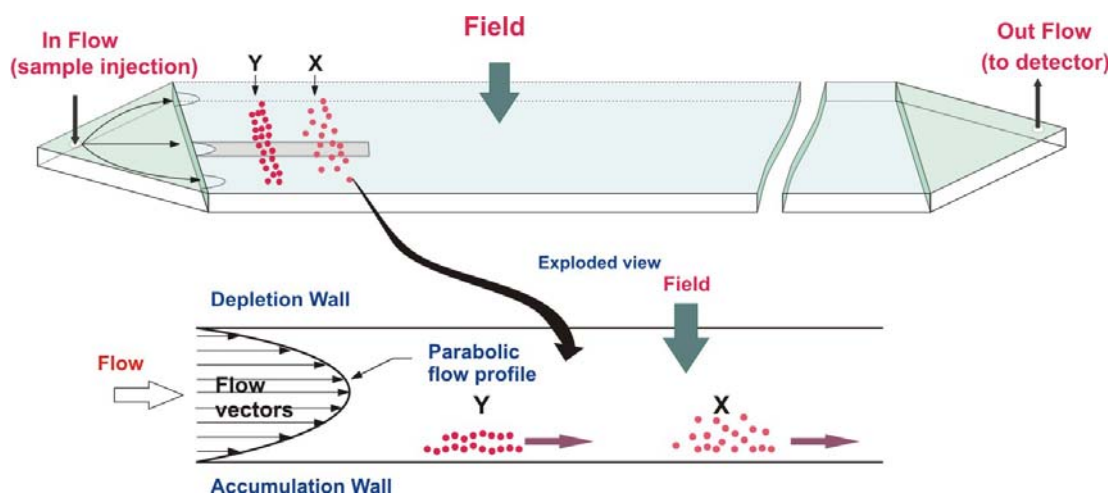

Fig. 5.1 - Ribbon-like channel structure typically used in FFF technique (top)
and parabolic flow profile inside the channel (bottom).

FFF, together with liquid chromatography (LC), is a flow-assisted separation technique. As in LC, a mobile phase flow drives the sample components along the separative device; unlike LC, FFF has no stationary phase and the separation is

performed in an empty capillary device, *the channel*. Separation is induced by the interaction of sample components with an externally generated field, which is applied perpendicularly to the direction of the mobile phase flow (Fig. 5.1) [4].

The channel has conventionally a rectangular shape with two plates used as channel walls. The field is applied orthogonally with respect to mobile phase and across the faces of the channel, driving components away from one channel wall (the depletion wall) and toward the opposite channel wall (the accumulation wall).

The FFF instrumentation scheme has been directly derived from classical LC where the separation column is replaced by the FFF channel; a scheme is reported in Fig. 5.2.
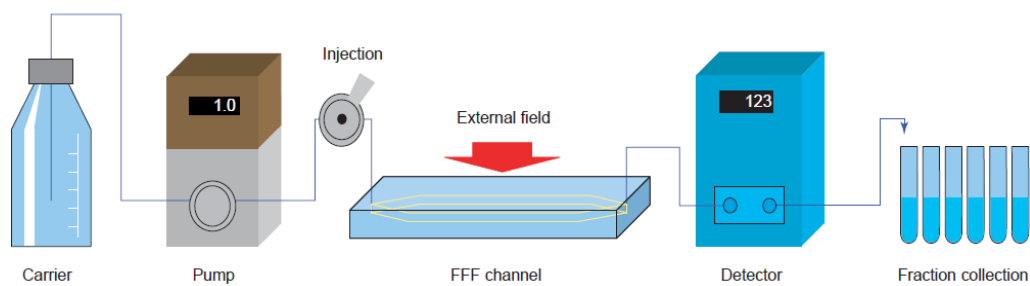
Fig. 5.2 - FFF instrumentation scheme [4].

The mobile phase flow inside the channel is usually delivered by a pump which can be a peristaltic or a syringe pump in the simplest variant of FFF. Sample mixtures are injected into the channel inlet through an injection port.

A detection system with a flow-through sample cell is connected downstream of the channel outlet for online recording of the signal generated by the eluted analyte. A fraction collector can be positioned downstream of the detection system if the fractionated analytes need further characterization or to be reused. The result of the analysis is a fractogram, i.e. a detector response versus elution time (or elution volume) curve (Fig. 5.3).

Most commonly used detection systems are the ultraviolet–visible (UV-Vis) spectrophotometric detectors for LC. Laser light scattering, refractive index, luminescence detectors and, most recently, soft-impact mass spectrometers have also been combined with UV-Vis detection [4].
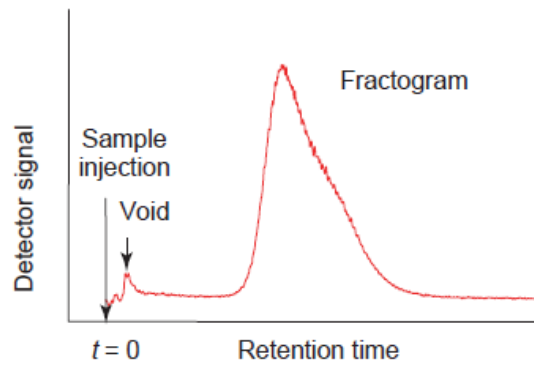
Fig. 5.3 - A typical fractogram [4].

In a FFF channel, sample separation is obtained in three steps:

1. *Injection*: when the sample plug is injected, an injection flow drives the particles to the beginning of the channel.

2. *Stop-flow relaxation*: after sample injection, the flow is stopped and the applied field drives the particles toward the accumulation wall.   Particles reach an equilibrium position across the channel thickness due to the opposing forces that counteracts the primary forces due to the fields (see below). These forces are related to native morphological properties of analytes.

3. *Elution*: after the relaxation time, the mobile phase flows is restored and it drives the separated components to the detector. Based on the equilibrium positions, particles elute with different velocities.

5.2.1 - Fields and Channel Geometry in FFF

Depending on the nature of the applied field, different variants of FFF were developed, each suitable for a specific analyte. Typical fields include gravitational force, electrical potential, temperature gradient, magnetic, a cross-flow stream, centrifugal force, dielectrophoretic and standing acoustic wave and fields. These give rise to several FFF techniques including gravitational FFF (GrFFF), electrical FFF (ElFFF), thermal FFF (ThFFF), magnetic FFF (MgFFF), flow FFF (FlFFF or F4), sedimentation FFF (SdFFF), dielectrophoretic FFF (DEP-FFF), and acoustic FFF (AcFFF). Each type of field interacts with a different physicol-chemical property of the analyte; consequently, analyte retention and separation are achieved according to

different analyte properties such as size, thermal diffusion, charge, density, mass, and magnetic susceptibility [5].

Conventional FFF channels are constructed by clamping a thin spacer (usually of Mylar or polyimide) with the desired geometric between two blocks with flat surfaces. The block material must be compatible with the carrier liquid and transmit the applied field. The ribbon-like channel is the most commonly employed channel geometry (Fig. 5.4).
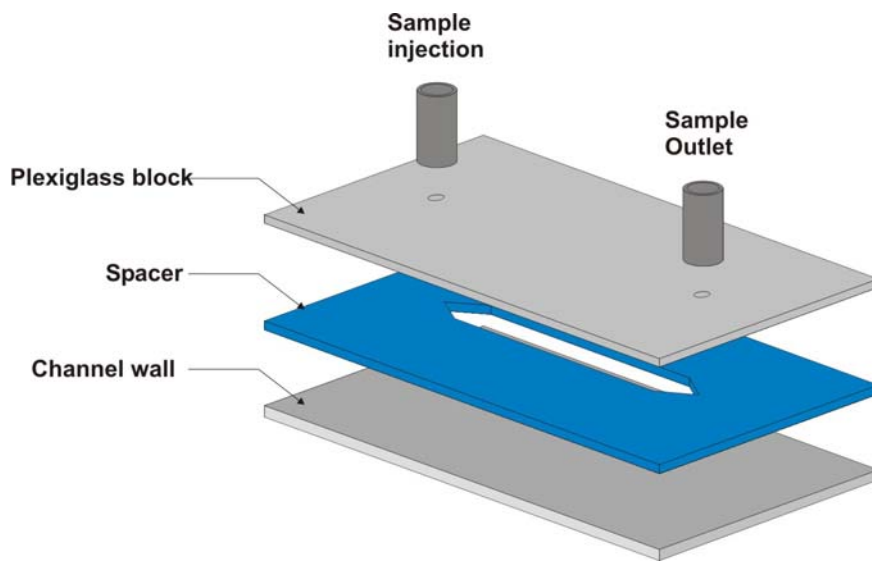
Fig. 5.4 - Ribbon-like channel cut from thin spacer and sandwiched between two walls.

Because of diffusion is a slow process, the channel thickness must be small enough to assure the capillarity geometry and that the sample reaches equilibrium in a reasonably short time. The length of the channel needs to be long enough to allow adequate retention time differences between the analytes. Typical channel dimensions are: thicknesses of 50 – 500 µm, breadth of 2 cm, and tip-to-tip lengths of 25 – 90 cm for a total volume of some milliliters [5].

5.2.2 - General principles and operating modes

Due to the high aspect ratio, the FFF rectangular channel can be considered as two infinite parallel plates in which a laminar parabolic flow profile is developed, with flow velocity increasing from near zero at the channel walls to a maximum at the centre of

the channel (Fig. 5.1). The perpendicularly applied force drives the sample toward the accumulation wall. A counteracting diffusive force develops due to the concentration build up at the wall and drives the analyte towards the centre of the channel. When the forces balance, steady state equilibrium is reached and an exponential analyte concentration profile is built up. Retention occurs when analytes reside in flow velocity zones slower than the average flow velocity of the carrier liquid passing the channel. Separation occurs because different analytes reside in different flow velocity zones (see Fig. 5.1).

In FFF, analytes can be separated by different operating modes. The mode of operation determines the elution order of analytes, along with other separation characteristics such as selectivity and resolution [5]. The three widely used modes of operation are:

1. *Normal mode* (based on Brownian motion of the analyte in the channel) drives the elution of macromolecules and submicrometer particles. As the macromolecules or particles that constitute the sample are driven by the field toward the accumulation wall, their concentration increases with decreasing distance from the wall (Fig. 5.5).
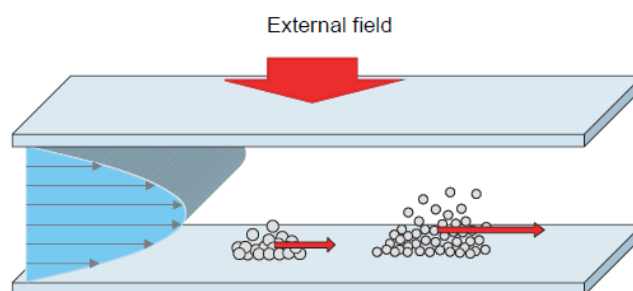
Fig. 5.5 - Normal FFF mode [4].

This creates a concentration gradient that causes sample diffusion away from the wall. When these two opposite transport processes balance, the sample cloud reaches a characteristic average elevation from the wall. The lower the molar mass or size of the sample component, the greater the component cloud elevation, the deeper the cloud penetration into the faster streamlines of the parabolic flow profile and the shorter the time required by the component to exit the channel. Retention time in normal FFF is therefore shorter for lower molar mass or size [4].

2. *Steric mode* is governed by the physical (steric) barrier of the accumulation wall (Fig. 5.6).
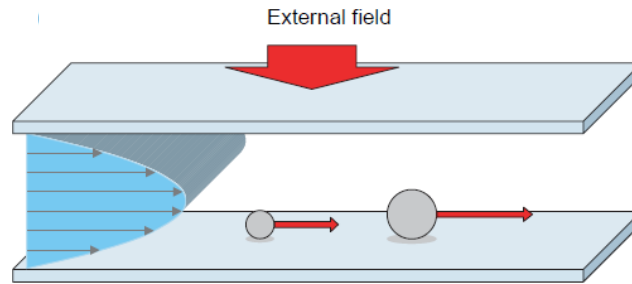
Fig. 5.6 - Steric FFF mode [4].

If the sample components are micron-sized particles, their diffusion away from the wall is negligible. Particles are in fact driven by the field directly to the accumulation wall and particles of a given size form a thin layer of a given thickness, hugging the wall. Larger particles form thicker layers that penetrate into faster streamlines of the parabolic flow profile, and they are eluted more rapidly than smaller particles. This is just the opposite of normal mode elution: it is then referred to as a reversed mode. Retention in steric FFF then depends only on particle size [4].

3. *Lift or hyperlayer mode* occurs when particles' moves toward the wall are opposed by mobile phase flow-induced lift forces (Figure 5.7, green arrows). When particles are driven from the wall by a distance that is greater than their diameter, the retention mode is called hyperlayer (Fig. 5.7). Retention in hyperlayer mode is still reversed with respect to particle size but it also depends on the various physical features of the particles, which will have a varying influence on the intensity of the flow-induced lift forces [4].

Fig. 5.7 - Lift or hyperlayer FFF mode [4].

5.3 - GRAVITATIONAL FIELD-FLOW FRACTIONATION: TOWARDS THE MINIATURIZATION

The GFFF is the simplest FFF variant and it employs the Earth's gravity field as applied perpendicular field. [6]. The channel profile is 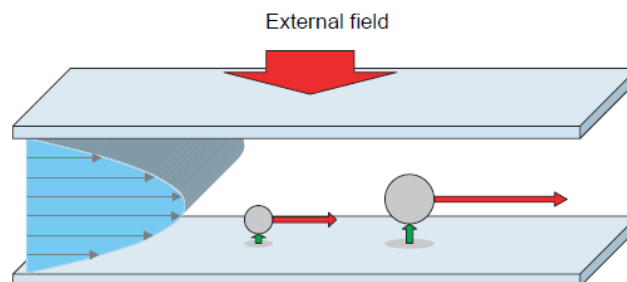cut out from a thin plastic foil, which is sandwiched between two bars (the so-called channel walls) made of glass or plastics (see Fig. 5.4) resulting in a channel volume of some millilitres. The GrFFF device is so low-cost that it is potentially suited to disposable usage. Due to the weakness of applied field, its range of application is directed to micrometer-sized analytes, among which cells. The simplicity of the separation device makes GrFFF particularly interesting for implementation in biomedical protocols aiming at the development of methods for sorting/fractionation of living cells. The absence of a stationary phase, the gentle fractionation mechanism, the use of plastic channel walls, and the easy maintenance of sterile conditions make GrFFF a highly biocompatible technology for cell fractionation, which was shown to be able to fully preserve cell viability. Cells collected after GrFFF can be further characterized or reused. GrFFF was successfully used to fractionate different types of cells, among which bacteria, monocellular parasites, wine-making yeast, murine stem cells, human blood cells and stem cells [7].

In order to obtain a compact GrFFF device easily integrated in a microfluidic system for POCT applications, a silicon/Pyrex® micromachined GrFFF channel has been developed. This device, which is a modification of a design originally prepared as a packed column for gas chromatography, has been chosen as a first prototype for a feasibility study having the aim to investigate the microchannel performance in the GrFFF context.

5.3.1 - Channel Design, Fabrication and Interconnection

The prototype consisted in a 50-cm-long double spiral shaped separation column obtained through silicon micromachining techniques (see sections 1.1.4 and 1.1.5). The surface of the 4-inches silicon wafer, containing the rectangular cross-section microchannels (800 µm wide, 100 µm deep), has been encapsulated with a Pyrex® wafer. In Fig. 5.8 a GrFFF microchannel layout is shown.
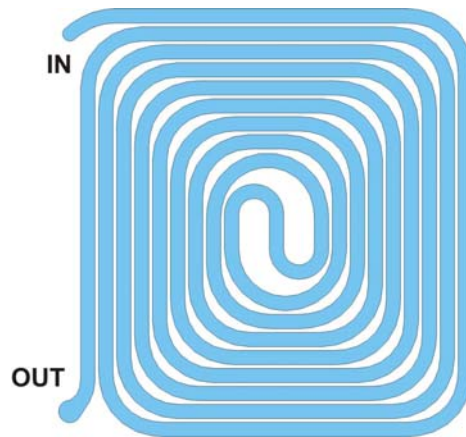
Fig. 5.8 - GrFFF microchannel mask layout and In-Out holes.

The process flow for the fabrication of the GrFFF microchannel is depicted in Fig. 5.9 (A – F) and consists of the following steps:

A. On the surfaces of a 4 inches – double polished silicon wafer (thickness = 500 μm), a thin Low Thermal Oxide (LTO) layer has been deposited.

B. The LTO layer has been patterned on the front side, acting as mask layer for the subsequent etching.

C. 100 μm deep channels have been realized by a DRIE process (see section 1.2.2.3)

D. Photoresist and LTO were removed by an oxygen plasma and a diluted HF solution, respectively.

E. A thin silicon oxide film is grown.

F. Finally, channels inlet and outlet are obtained on a Pyrex® wafer through laser cutting process and the two wafers (Silicon + Pyrex®) are fixed together via anodic bonding process (see section 1.2.2.3) to enclose the microchannels.
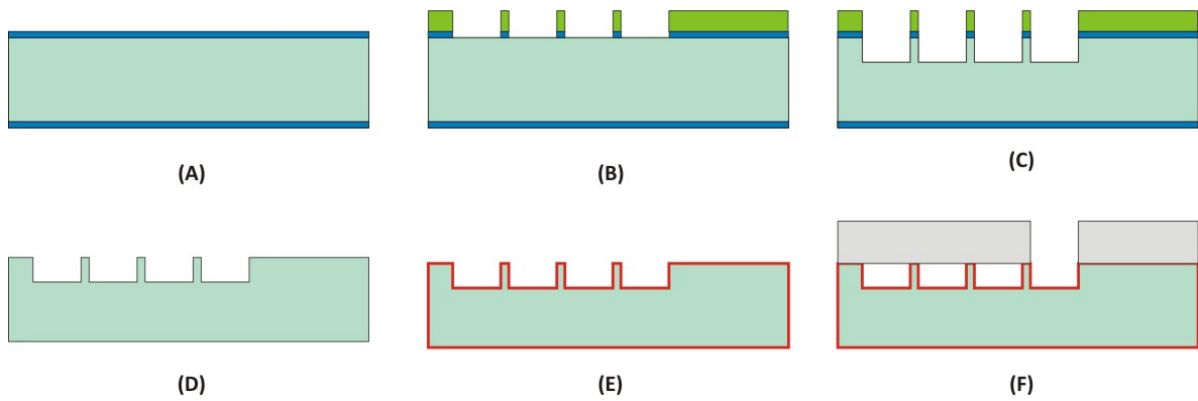
Fig. 5.9 - Technological process for GrFFF microchannel fabrication.

In Fig. 5.10 a SEM cross-section view of the fabricated silicon microchannels is shown.
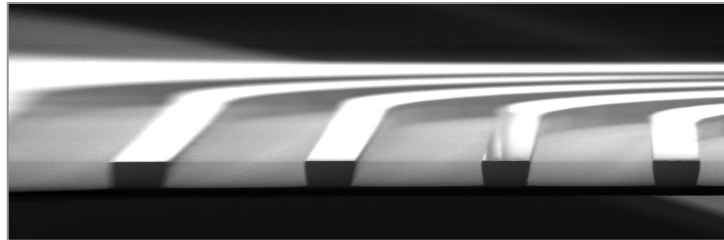
Fig. 5.10 - SEM image of cross-section rectangular microchannels.

Finally the single chips (size 2.5 cm x 2.5 cm) have been separated by a dicing saw and the MEMS GrFFF channel fabricated at CNR-IMM Bologna is shown in Fig. 5.11.
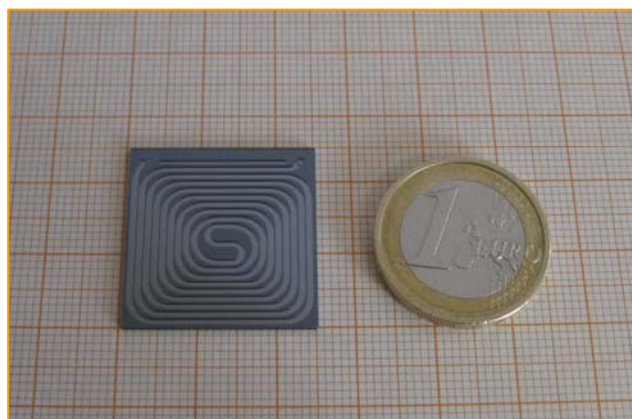
Fig. 5.11 - A MEMS-GrFFF microchannel compared with 1 euro coin.

When dealing with miniaturized devices, a critical point is developing macro-to-micro fluidic interfaces, in fact this is an active research area and a suitable standard does not exist [8].

In the first prototype, a fluidic interconnection system has been obtained by means of 1/16'' OD PEEK tubing supplied by Upchurch® Scientific. PEEK tubings (ID 125 µm) have been inserted in the In-Out holes of the GrFFF microchannel. The 8-cm long connecting lines have been sealed in the fluidic ports by means of an epoxy resin (Varian Torr Seal®) (Fig. 5.12).
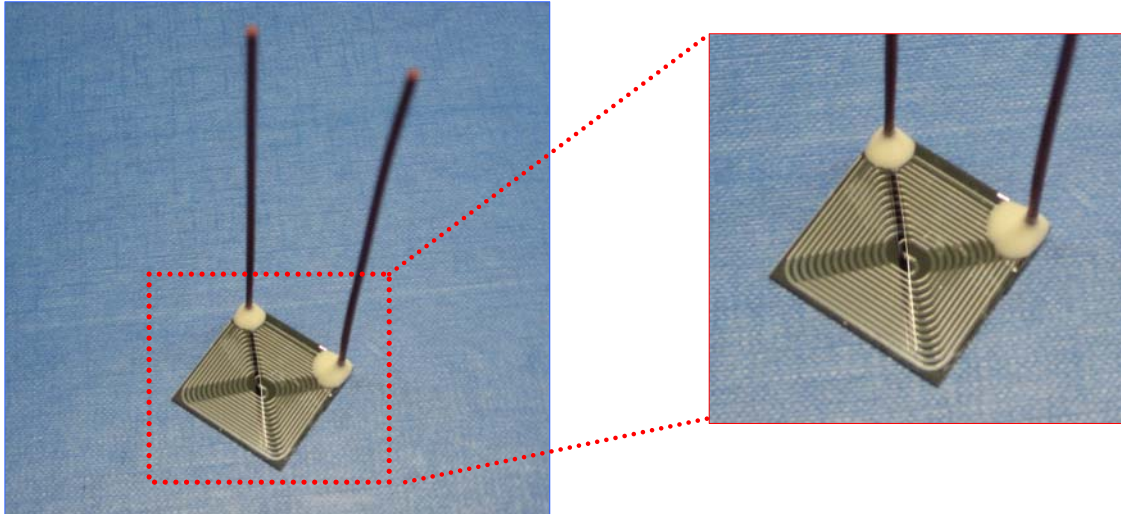
Fig. 5.12 - PEEK tubings (1/16" OD; 125 µm ID) interconnection sealed with Varian Torr Seal®. Detail of fluidic interconnetcion is shown on the right.

Unfortunately, this typology of fluidic interconnection has not been able to withstand the mechanical stresses over time and then a new device has been developed for ensuring more robustness to the fluidic system.
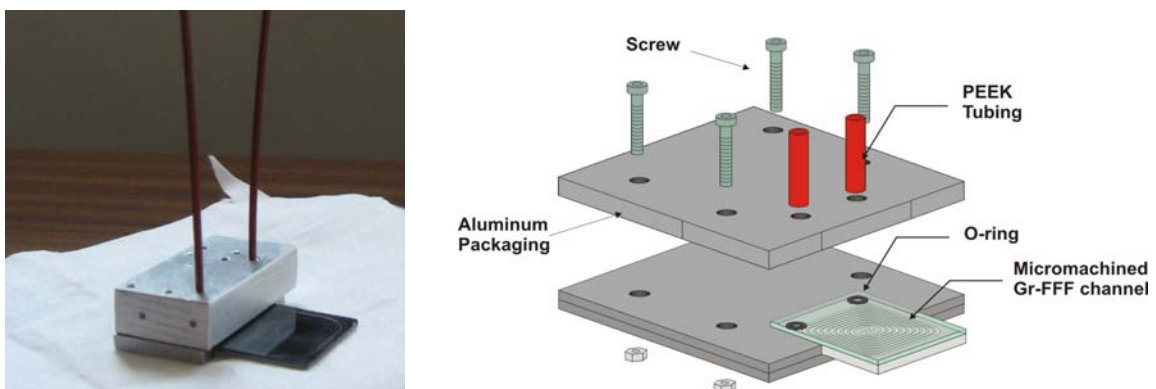
Fig. 5.13 - Photograph (left) and schematic representation (right) showing the aluminum manifold packaging for the GrFFF microchannel

As depicted in Fig. 5.13, the GrFFF microchannel has been housed in appropriate aluminum manifold packaging. This device has been fabricated by assembling two aluminum blocks by means of four screws and PEEK tubings have been connected to the In-Out holes through silicone O-rings.

5.3.2 - Experimental Results

The experiments have been conducted using the apparatus depicted in Fig. 5.14. In order to explore the potentialities for the application of microGrFFF to cell fractionation, cultivated bacteria samples were employed.

The carrier flow has been delivered by a syringe pump (KDScientific, KDS100). Samples have been injected in the microchannel by a Rheodyne Model 7125 valve (Rheodyne, Cotati, CA) equipped with a 1 µL PEEK loop. The eluting fractions have been detected by a flow-through UV–Vis detector (UV6000 LP, ThermoQuest, Austin, TX) connected to the microchannel outlet.
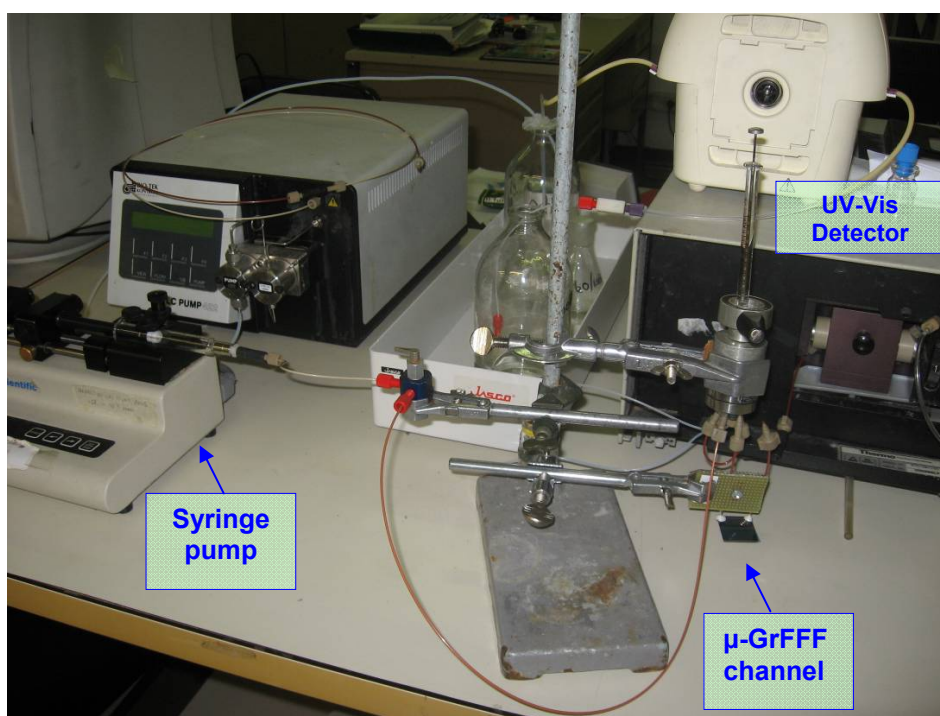
Fig. 5.14 - Experimental apparatus.

The mobile phase has been phosphate buffered saline (PBS) 150 mM at pH = 7.4, able to preserve cell integrity during fractionation process.

The sample (*Escherichia Coli* bacteria cells with 1.2-4 μm as cell length and a rod shape) has been injected for 6 s at a flow rate of 0.05 μL/min and then the flow has been stopped for 10 min to allow the sample relaxation (stop-flow). At the end of the stop-flow time, sample elution has been started at a flow rate of 50 μL/min. The signal from eluted cells has been recorded at λ = 600 nm.

Results are reported in Fig. 5.15. It is shown that by introducing a relaxation phase with respect to a flow injection analysis (FIA), a retention peak is obtained. The first band represents the void peak corresponding to unretained analytes; the second band corresponds to retained *E. Coli* cells. For preventing the presence of false peaks due to possible system perturbations, only the mobile phase (blank signal) has been injected in the same experimental conditions. As depicted in Fig. 5.15, the signal obtained with blank stop-flow is near to zero and only a slight disturbance in correspondence of the void peak is visible. This result allows confirming that the elution signal is due to sample.

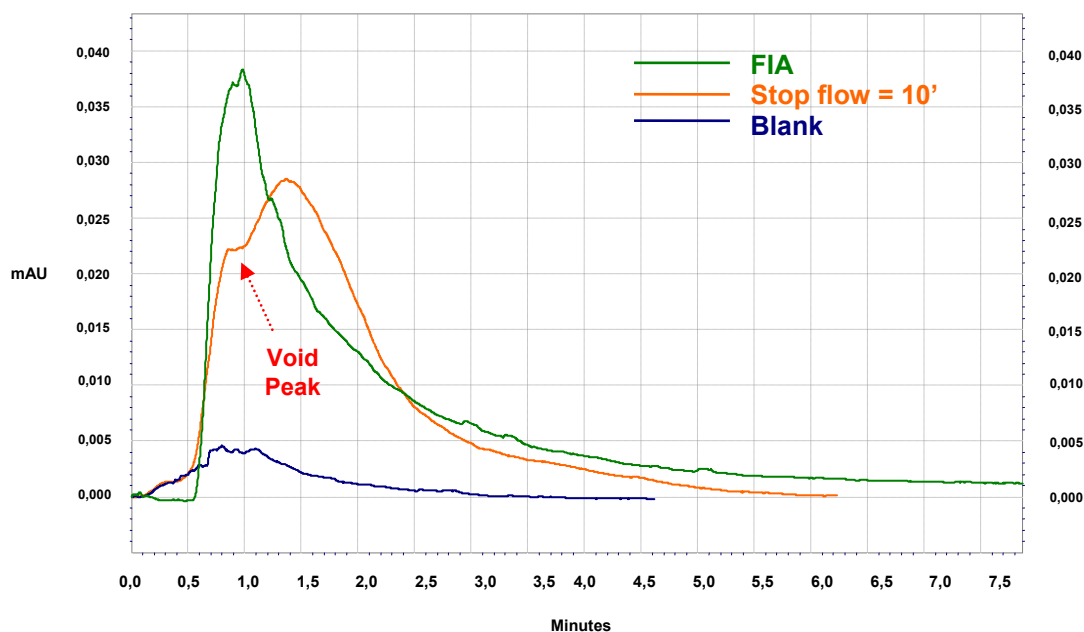*Fig. 5.15 - Micro-GrFFF fractionation of E.Coli (orange line); elution flow rate = 50 μL/min; relaxation time 10 min and fractographic profile registered at 600 nm. Flow injection analysis (FIA) is in green line, whereas the only mobile phase (blank) is in blue.*

The retention peak is more evident if the stop-flow time is increased (Fig. 5.16), according to the FFF theory.

The result can be considered satisfactory since the microchannel is able to fractionate the analyte also injecting 1 µL of dilute sample dispersion (OD_{600} = 0.017; $3X10^7$ cells/mL) and its represent the first example of a miniaturized GrFFF device. The next step has been the comparison of the fractograms obtained with the microchannel and those obtained with the conventional macro-channel.
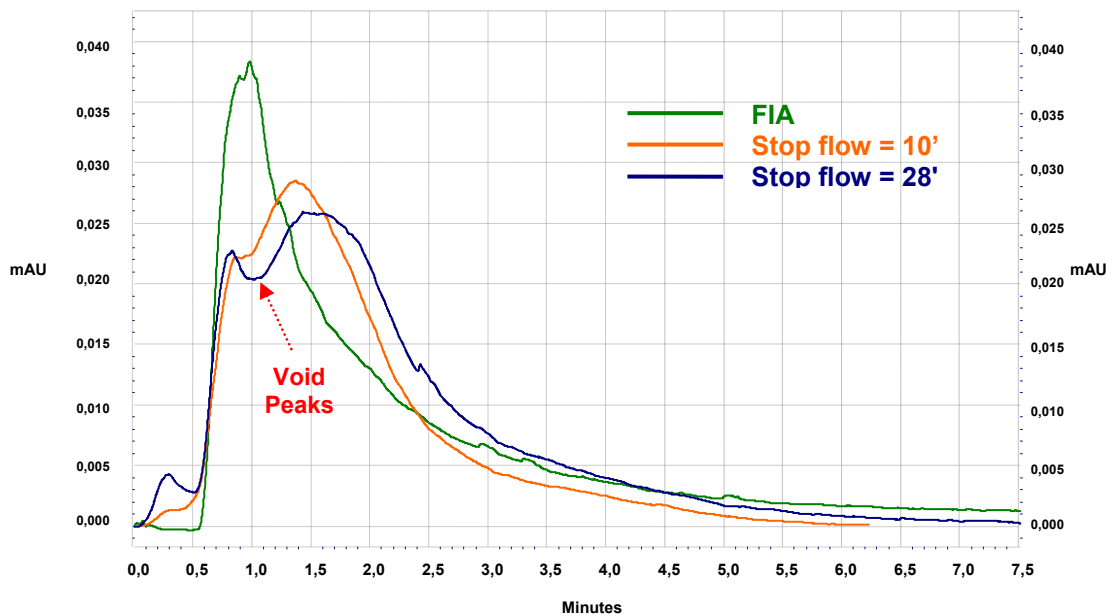
Fig. 5.16 - Micro-GrFFF fractionation of E.Coli at two relaxation time: 10 min (orange line); and 28 min (blu line); elution flow rate = 50 µL/min; relaxation time 10 min and fractographic profiles registered at 600 nm. Flow-injection analys (FIA) is in green.

Despite the high advantages of low sample dilution for injected samples, from the fractographic profiles, it has been observed that concerning the resolution the microchannel performances are not optimal when compared with those obtained by injecting the same sample in a traditional linear channel having dimensions of 30.0 cm in length (tip-to-tip), 0.025 cm in thickness and 2.0 cm in breadth (see Fig. 5.4). The fractographic profile (Fig. 5.17) shows a retention peak very well defined and clearly separated from the void peak.
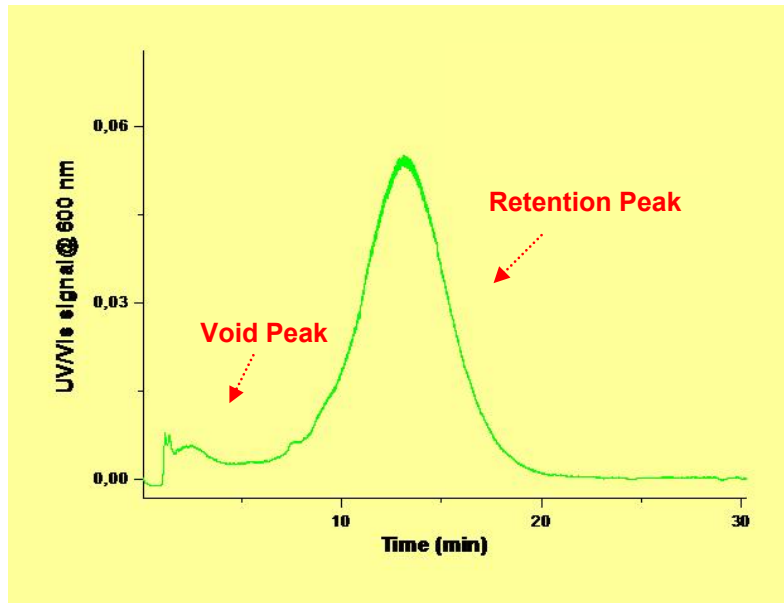
Fig. 5.17 - Conventional GrFFF fractionation of E.Coli; elution flow rate = 1.5 mL/min; relaxation time: 30 min and fractographic profiles registered at 600 nm.

The reason is expected to be in non-conservation of laminar flow inside the microchannel. Typically, flow in conventional microchannels, having planar straight geometry, is laminar and any mixing that occurs is purely by diffusion.
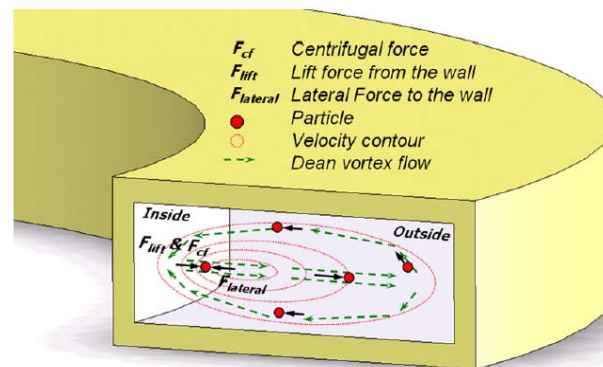
Fig. 5.18 - Flow in a curvilinear channel. The centrifugal force on fluid element generates the secondary flow or 'Dean vortex' [9].

In curved channels, instead, transverse secondary flows, commonly referred to as the Dean vortices, arise as a result of the interaction between inertial and centrifugal forces. These centrifugal effects induce a secondary flow field characterized by the presence of two counter-rotating vortices located above and below the plane of symmetry of the channel, coinciding with its plane of curvature (Fig. 5.18).

The magnitude of these effects is characterized by the dimensionless Dean number (D_e) defined as:

$$De = Re \sqrt{\delta} \qquad (5.1)$$

where $\delta = (D_H/2R)$ is the curvature ratio, that is the ratio of the channel hydraulic diameter (D_H) to the flow path radius of curvature (R) and Re is the Reynolds number gives by:

$$Re = \frac{\rho U_m D_H}{\mu} \qquad (5.2)$$

where ρ is the fluid density, U_m is the average flow velocity and μ is the dynamic viscosity of the fluid.

At low flow rates, the strength of Dean vortices is not sufficient to significantly perturb the laminar flow profile, and then mixing between two parallel streams is primarily by diffusion. With increasing flow rate, the Dean vortices become stronger and greatly increase the extent of mixing. Hence, as the radius of curvature decreases, the Dean number increases due to a corresponding increase in the value of curvature ratio (δ) [10].

Reschiglian *et al.* [4] recently have developed a GrFFF device based on a new GrFFF channel design with respect to the conventional rectangular geometry.

Fig. 5.19 - Sketch of an 'S'-shape macro-GrFFF channel.

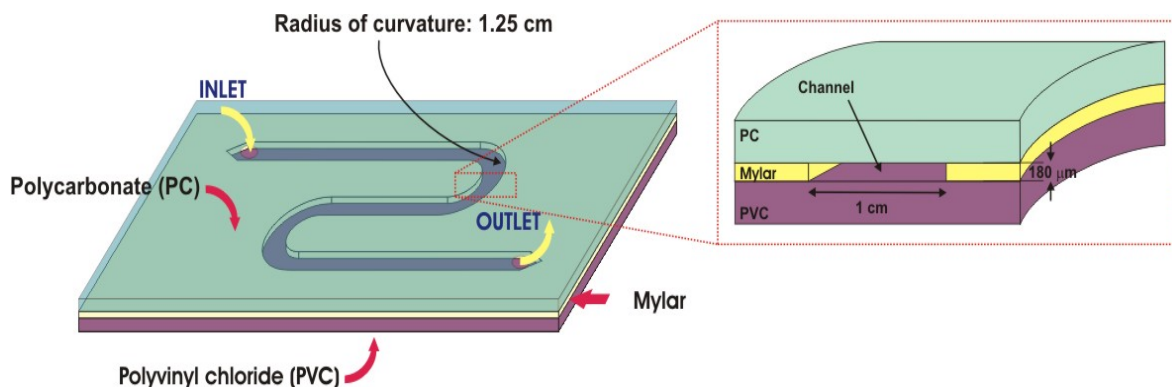The GrFFF channel, cut from a Mylar spacer, had a curvilinear shape with an 'S' geometry characterized by two curvilinear parts of 3.9 cm with a radius of curvature

of 1.25 cm. The channel presented conventional dimensions of 30.0 cm in length (tip-to-tip), 0.018 cm in thickness and 1.0 cm in breadth and it is sandwiched between polycarbonate (PC) and polyvinyl chloride (PVC) walls (Fig. 5.19).

This compact GrFFF device has been developed to be integrated in a microfluidic system for POCT applications, since it keeps the same fractionation performance obtained by the rectangular shape traditional GrFFF channels and it was applied to the separation of serum from blood sample and for an enzymatic analysis for diagnostic purpose.

A small volume (50 µL) of human whole blood sample diluted 1:100 (v/v) with saline solution (NaCl 9 g/L) has been injected into the GrFFF system for separation of plasma from cells.
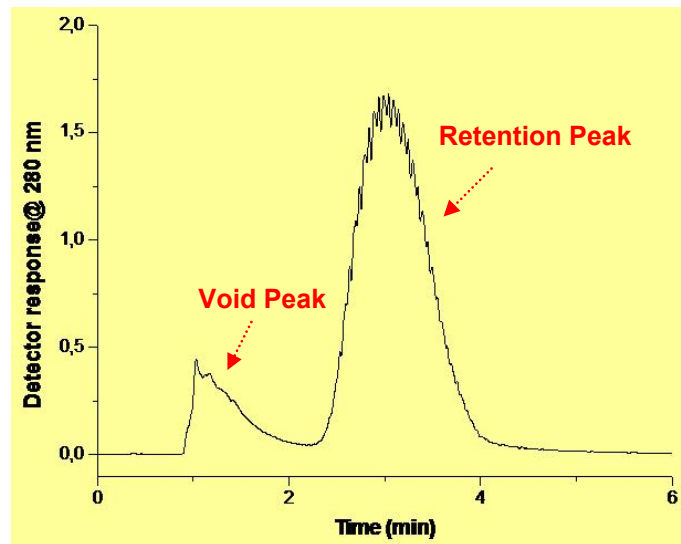
Fig. 5.20 - GrFFF-S-shaped channel fractionation of human whole blood, elution flow rate = 1 mL/min; relaxation time = 2 min and fractographic profile registered at 280 nm [4].

The signal has been recorded by means of an on-line UV6000 LP, diode array UV/Vis detector (ThermoQuest, Ausin, TX), operating at 280 and 600 nm. A representative GrFFF profile is reported in Fig. 5.20. When whole blood is injected into a GrFFF channel, plasma components are not retained by the system and are thus eluted in a single peak corresponding to the void volume, while blood cells are subjected to retention mechanisms and are thus eluted later (retention peak) [4].

Hence a theoretical comparison between the 'S' - shaped macrochannel and the double-spiral silicon microchannel (Fig. 5.21) has been performed. Water (μ = 0.001

Pa·s; ρ = 1000 Kg/m^3) has been used as a carrier fluid at 20 °C and a flow rate = 0.1 mL/min.
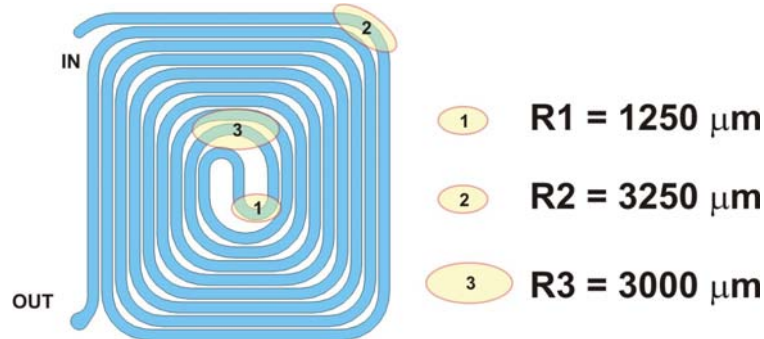
Fig. 5.21 – Micro-GrFFF channel radii of curvatures.

As can be disclosed from the Tab. 5.1, decreasing the channel curvature radius, Dean vortices increase and flow mixing occurs.

	'S'- shape GrFFF channel	**micro-GrFFF channel**
D$_H$ (µm)	353	178
R (µm)	12500	1250
δ	0.014	0.07
De	~ 0.0388	~ 0,98

Tab. 5.1 - Comparison between 'S'-shape GrFFF channel and micro-GrFFF channel.
Water (µ = 0.001 Pa·s; ρ = 1000 Kg/m^3) has been used as a carrier fluid
at 20 °C and a flow rate = 0.1 mL/min.

This situation is detrimental when it occurs within a GrFFF channel having small curvature radii, because the separation of the sample components is lost as soon as the particles reach the curved portion of the channel.

Unfortunately, from these calculations it is easy to disclose that the geometry of the micro-GrFFF cannel of the prototypal device used for these tests is not optimal due to the small curvature radii. In order to obtain a compact and reliable device with good performance for POCT applications, a new micro-GrFFF channel layout will be designed, aiming to minimize as much as possible the perturbation factors that degrade the microfluidics of the system. Hence, the main goal is to find the best compromise between microchannel geometry and chip dimensions. In addition, new

methods and materials for fabricating the micro-GrFFF device will be investigated, considering the market constraints for POCT testing devices, which are generally expected to be disposable and to have a low cost per unit, silicon etching may be found to be too expensive. By this purpose, soft lithographic methods, based on rapid prototyping and replica molding, provide faster and less expensive fabrication processes than conventional ones based on silicon or glass. Amongst materials, polydimethylsiloxane (PDMS) is an excellent polymeric material for the fabrication of Bio-MEMS since it is biocompatible, nontoxic and optically transparent and can be used as a stamp resin in the procedure of soft lithography [11].

REFERENCES

[1] "*Microfluidic Technologies for Miniaturized Analysis Systems*", Hardt S. and Schönfeld F. eds. (2007), Chapter 12.

[2] Roda B. et al.; *Analyst*, **138**, (2013) 211-219.

[3] Schimpf M.E., Caldwell K. and Giddings J.C.; "*Field-Flow Fractionation Handbook*", Wiley-Interscience (2000).

[4] Reschiglian P. et al.; *TRENDS in Biotechnology*, **23**, (2005) 475-483.

[5] Messaud F.A. et al.; *Progress in Polymer Science*, **34**, (2009) 351–368.

[6] Reschiglian P. et al.; *J. Chromatogr. A*, **740** (1996) 245-252.

[7] Roda B. et al.; *Anal. Bioanal. Chem.* **392** (2008) 137–145.

[8] "*Lab on a Chip Technology, Volume 1: Fabrications and Microfluidics*", Herold, K.H. and Rasooly A. eds. (2009).

[9] Seo J. et al.; *J. Chromatogr. A.*, **1162**, (2007) 126-131.

[10] Sudarsan A.P. and Ugaz V.M.; *Lab. Chip.*, **6**, (2006) 74-82.

[11] McDonald J.C. et al.; *Electrophoresis*, **21**, 27-40 (2000).

CONCLUSIONS

Nowadays microfluidic is becoming an important technology in many chemical and biological process and analysis applications. The potential to replace large-scale conventional laboratory instrumentation with miniaturized and self-contained systems, (called micro-total-analysis-systems (µTAS) or lab-on-a-chip (LOC)), offers a variety of advantages such as low reagent consumption, faster analysis speeds, and the capability of operating in a massively parallel scale in order to achieve high-throughput. These requirements are also most important in bioanalysis, where the development of point-of-care-testing (POCT) devices aims at rapidly performing clinical chemistry assays directly where the sample is obtained. Micro-electro-mechanical-systems (MEMS) based technologies enable both the fabrication of miniaturized systems and the possibility of developing compact and portable systems.

By this purpose, design parameters, process flows and experimental characterizations of silicon MEMS devices suited for both high-speed gas chromatography (HSGC) and gravitational field-flow fractionation (GrFFF) have been reported and thoroughly described in this dissertation.

Concerning the HSGC, the development of a complete platform of three MEMS-based gas chromatographic core components: injector, separation column and detector have been presented. The three silicon devices have been designed to satisfy the geometrical and physical constraints imposed for implementation of the HSGC technique.

The microinjector consists of a 12 x 12 mm^2 silicon chip integrating five microvalves, based on a pneumatically actuated polymeric membrane, and a 2 µL-volume sample loop. It should be stressed that, unlike previously reported micromachined injectors, the microdevice presented in this thesis has been completely fabricated at wafer level by using standard MEMS technologies.

The functional characterization of the chip injector has been performed by connecting the microdevice to a conventional GC system. A natural gas sample mixture has been used in all the experiments. Both the linearity and repeatability of the injecting mechanism has been evaluated and the results have been very satisfactory.

Moreover it has been demonstrated that the microinjector is able to ensure very low dead volume and fast injection time, according to HSGC requirements.

In addition further characterizations have been performed aimed at investigating both the mechanical robustness and the chemical inertness of the polymeric membrane. The former property has been tested by applying heavy mechanical stress cycles on the membranes. The latter property has been demonstrated by continuously exposing the polymeric membranes to injections of three different types of potentially corrosive solvents (such as trichloroethylene, toluene and isopropyl alcohol). These tests have showed that, despite the harsh working conditions the chip has been submitted to, the good injecting performances of the microdevice remains unchanged.

The separation column has been designed according to HSGC requirements: short column length (fast analysis time) and small inner diameter (high analysis performance). For this purpose, a 2-meter long all-silicon microcolumn having a nearly circular cross-section channel (with a 100 μm ID) has been fabricated by using standard MEMS technologies. It should be stressed that, unlike previously reported silicon microcolumns having a rectangular cross-section channel, the circular geometry of the MEMS column presented in this thesis, has enabled a uniform deposition of the stationary phase on the microchannel walls. The microdevice has been extensively characterized on standard GC benchmark mixture (Grob test) yielding separation performances very close to the theoretical ideal expectations. In fact, in terms of efficiency the MEMS column yield over 9000 plates/meter, compared to the expected 10000 theoretical plates and the quality of the results in terms of chemical inertness have been shown in the Grob test chromatograms. In addition, real samples have been analyzed and the excellent peaks resolution and their perfectly Gaussian shape have confirmed the good MEMS-column performance. Furthermore, both minimum height-equivalent-to-a-theoretical plate ($HETP_{min}$) and optimal average carrier gas velocity ($\bar{u}_{opt}$) experimental values have been comparable to the theoretical ones.

A thermal conductivity detector (TCD) has been chosen to be miniaturized since the volume reduction of the detector chamber results in an increased mass sensitivity (at a given concentration) and reduced dead volumes, according to HSGC requirements.

The microfabricated TCD has been fabricated using conventional MEMS technologies. The silicon chip (having the dimensions of 5 mm x 5 mm and containing four resistors put within a Wheatstone bridge configuration) has been encapsulated with a mechanically micromachined Pyrex® wafer implementing ultra-low-volume microchambers. The microdevice has been characterized by an appropriate experimental setup to preliminarily investigate its sensitivity with respect to changes in two gas carrier compositions i.e. nitrogen and helium. The test has confirmed the ability of the detector to discriminate between two gases having different thermal conductivity. The functional characterization of the microTCD has been performed by connecting the device to the outlet of a commercial GC/TCD system for preliminary comparative tests. The results obtained have been comparable for both detectors. The results obtained from all the tests have been very satisfactory since the microTCD has shown both a good sensitivity and a very wide dynamic range.

Finally the microinjector and microTCD have been connected upstream and downstream respectively, to a conventional fused silica capillary column. By injecting a real sample gas mixture, the analytes have been eluted in less than 120 s and the separation between the peaks has been an index of the good operation of the microdevices.

All micromachined devices have been integrated into a specifically designed system motherboard providing electrical and pneumatic connections as well as precise temperature control. The overall dimensions of the system, including all accessories and the control electronics is of 35 x 15 x 25 cm^3. The integration work is current ongoing and no experimental results can be reported at this stage.

Concerning the FFF technique, the gravitational FFF (GrFFF) variant, exploiting the Earth gravitational field to structure the separation, appears to be particularly suited for its implementation in POCT systems thanks to the simplicity of its separation device, amenability to miniaturization, and the potential easy on-line integration with specific analytical modules. The development and experimental characterization of a miniaturized GrFFF channel have been discussed in this thesis. This device, which is a modification of a design originally to be employed as a packed column for gas chromatography, has been chosen as a first prototype for a feasibility study having the aim to investigate the microchannel performance in the GrFFF context.

From experimental data obtained by analyzing bacteria samples (such as *Escherichia Coli*) it has been observed that the microchannel performances are not optimal when compared with those obtained by injecting the same sample in a traditional linear macro-channel. The reason is expected to be in non-conservation of laminar flow inside the microchannel. It known that curvatures in a channel generates flow perturbations which may cause sample mixing. The extent of this mixing depends on the curvature radius: the smaller the radius, the greater the flow mixing. So within a GrFFF channel with small curvature radii, the flow mixing becomes not negligible because, as soon as the different particles reach the curve, the separation of the sample components is lost.

On the other hand, the same experiment performed on a 'S'-shaped macrochannel with a greater curvature radius yielded results comparable to those obtained on a traditional liner-shaped one.

In order to obtain a compact and reliable device with good performance for POCT applications, a new micro-GrFFF channel layout will be designed, aiming to minimize as much as possible the perturbation factors that degrade the microfluidics of the system. In addition, new methods (such as soft litography) and materials (such as polydimethylsiloxane, PDMS) for fabricating the micro-GrFFF device will be investigated, considering the market constraints for POCT testing devices, which are generally expected to be disposable and to have a low cost per unit, silicon etching may be found to be too expensive. By this purpose PDMS is an excellent polymeric material for the fabrication of Bio-MEMS since it is biocompatible, nontoxic and optically transparent and can be used as a stamp resin in the procedure of soft lithography.